At the Intersection of Bistability and Elastic Instability: Switching and Locking Structures using Asymmetric Carbon Fiber Composites

Vishrut Jitendra Deshpande

Dissertation submitted to the Faculty of the
Virginia Polytechnic Institute and State University
in partial fulfillment of the requirements for the degree of

Doctor of Philosophy
in
Mechanical Engineering

Suyi Li, Chair
Michael Bartlett
Zhenhua Tian
Michael Philen
Oliver Myers

April 1, 2025
Blacksburg, Virginia

Keywords: Bistable laminates, Composites, Buckling, Origami, Kirigami

At the Intersection of Bistability and Elastic Instability: Switching and Locking Structures using Asymmetric Carbon Fiber Composites

Vishrut Jitendra Deshpande

ABSTRACT

The next evolution of engineered structures would be to have an on-demand ability to become soft and foldable for packing in compact dimensions. This adaptive capability makes them convenient in transportation such as space structures where packaging of large deployable structures is crucial that help meet ever increasing energy demands of satellites. To render such abilities, smart materials would become necessary – materials that show adaptability to certain stimuli and change one or more characteristic properties. For example, shape memory alloys (SMAs) shrink in length upon heating with increased longitudinal stiffness. Thus stiffness modulation and morphing ability is a crucial aspect of switchable systems. In our interest, Asymmetric Carbon-Fibre Reinforced Polymer (CFRP) laminates, have shown bistability, i.e., they have two stable equilibria or states that arise due to thermal imbalances during the curing process. This forces the laminate to exhibit two mutually perpendicular characteristic curvatures in two different stable states. The change from one state to the other is termed as a snap-through process. This study for the first time investigates the bistable laminates from a holistic perspective by understanding their quasi-static behaviors in mainly two important scenarios i.e. Out-of-plane and In-plane direction loadings. The authors in their first study uncover the different snap-through mechanics utilizing asymmetric boundary conditions. Three distinct snap-through characteristics are presented — two-step, one-step, and no-snap process — which depends on the load location and boundary conditions. For the second study, in-plane compression testing for bistable laminates reveal two drastically different responses – one very compliant and soft that behaves like a softening non-linear spring, and the other stiff response similar to thin columns which buckle under large loads. This material offers on-demand switching between these two responses by simply snapping their state from one to the other. Through extensive finite element simulation and experimentation, we present effective strategies to enhance their stiff response (buckling load) for improving the stiffness switching ratio. Learning through these behavioral characteristics of bistable laminates, a novel concept is implemented for morphing structures. A 'locking' feature is introduced by harnessing characteristic curvatures of these bistable laminates and strategically implementing them in morphing structures. We take inspiration from various origami folding patterns and incorporate a waterbomb geometry in these bistable laminates. This helps in changing the load-bearing capabilities of the bistable laminate, by switching from a very soft foldable state to a lockable stiff state. We present a case study on two origami designs, namely Kresling and Yoshimura, where using this bistability property delivers massively reconfigurable structures that show meta-stable load-bearing states.

At the Intersection of Bistability and Elastic Instability: Switching and Locking Structures using Asymmetric Carbon Fiber Composites

Vishrut Jitendra Deshpande

GENERAL AUDIENCE ABSTRACT

The next evolution of engineered structures would have an on-demand ability to become soft and foldable for packing in compact dimensions. This adaptive capability makes them convenient in transportation, such as space applications where the packaging of large structures (like the James Webb telescope!) that can be deployed in outer space, is crucial to meet ever-increasing energy demands of satellites. To propose, we investigate unsymmetric Carbon Fibre-Reinforced Polymer (CFRP) laminates that show *bistability*, i.e., they have two stable shapes. And to change from one shape to the other is termed a snap-through process. This study, for the first time, investigates the bistable laminates from a holistic perspective by understanding their mechanical behaviors in mainly two important scenarios- *out-of-plane* (transverse) and *in-plane direction* (in the direction of fibers). Firstly, this study uncovers the different snap-through behaviors when transverse forces are applied. Three distinctive behaviors are recorded and one could select either based on the snap-through actuation desired. Secondly, the study focuses on in-plane compression testing for bistable laminates. It reveals two drastically different responses – one very compliant and soft that behaves like a spring and the other a very stiff response similar to thin columns that buckle under large loads. This material offers on-demand 'switching' between these two responses by simply snapping their state from one to the other. Learning through these behavioral characteristics of bistable laminates, a foundational third study is proposed for origami-inspired morphing

structures - a ‘locking’ feature is introduced by harnessing their characteristic shapes and strategically implementing them for either locking them from folding or unlocking them to be allowed to fold. This provides such structures with added functionality to achieve complex motions energy efficiently and provide load carrying ability. Overall, the bistable nature of laminates can effectively enrich the origami-inspired morphing technology by utilizing their mechanical behaviors.

Contents

Chapter 1

Introduction

1.1 Literature Review

In the new era of material sciences, *smart materials* are defined as an entity that shows adaptability to work environments. For example, imagine an airplane that could optimize its performance by having the complete wing structure as a continuous flexible flap! Rather than a rigid body with just the tail parts as moving elements and leads to added weights of various parts embedded in the blade for its actuation. Instead, a continuous flexible flap would help reduce the weight and make airplane rides more comfortable than ever. The first steps in this direction can be seen in the new McLaren Speedtail series where their team has designed flexible carbon-fibre ailerons [1]. These flexible ailerons have replaced the traditional spoilers, giving a clear advantage of a continuum structure with better air dynamics. This would prove to be a crucial advancement for next-gen automobiles [2], especially in the field of electric automobiles where weight optimization is ever important.

Smart materials are able to adapt to their surroundings by changing their behaviors either by *intrinsic* property changes like the material parameters (stiffness modulus, Poisson's ratio, expansion coefficients), or *extrinsic* property such as shape, size, geometric reconfiguration, etc. During the literature review for materials that could be utilized for such functionalities through intrinsic changes, we commonly observe shape memory alloys (SMA), magnetic shape memory alloys (MSMAs), and Elastic memory composites (EMCs) materials that often need energy-expensive external stimuli such as electricity, temperature (heat), and magnetic fields to operate between different modes. These materials change the internal crystal/molecular structure at high transition temperatures and become visco-elastic with a stiffness change. They have found applications in medical surgery equipment used for minimally invasive treatments. They could be made bio-degradable and are used as temporary implants which, upon tissue regeneration, get dissolved by the body [3], wearable devices [4], and textile (clothing and apparels) applications [5]. The other notable materials that undergo intrinsic property changes could be thermochromic (susceptible to temperature and change color), photosensitive (responsive to light), piezoelectric (generate electricity upon mechanical stress), etc.

On the other hand, smart materials that change their appearance visibly, by changing extrinsic properties such as shape, size, or geometric configuration, to adapt to the environment. For example, magnetostrictive materials change their shape or dimensions upon an externally applied magnetic field with a high degree of precision. They are increasingly being adopted as actuators for vibration control, micropositioning, and deformable mirrors [6]. There are many other examples of smart materials that fall into this category such as shape memory polymers (SMPs, unlike SMAs undergo only reversible entropic elastic changes [7]), electrostatic layer jamming (ELJ, responsive to electro-magnetic fields) materials used for bending stiffness of actuators [8], and fluidic flexible matrix composites (F^2MC) that are actuated by fluid pressures [9].

Another unique shape-shifting material based on extrinsic property changes, which will become the base for our following studies, is *asymmetric Carbon-Fiber Reinforced Polymers* (CFRPs). ‘Asymmetric’ refers to the plies (layers) in the uni-directional composite laminates where the orientation of fibers within different layers is not symmetric about the mid-plane axis. Hence, the thermal strains developed in two perpendicular directions differ during the curing process. These differential strains in the laminate forces them to settle in a warped shape with a characteristic curvature. This could be called one of the stable states of the laminate. Noteworthy, this curvature can be flipped to the other direction by applying a sufficient out-of-plane force to change into other stable position, i.e., laminates show *bistable* nature. This shape change from one to the other is generally referred to as *snap-through* process. Usually, symmetric laminates are desired for various applications where fixed structures are needed. Hence, warping in such laminates was initially understood as a local deformity with no particular usage. Until seminal research that helped realize a new approach to such asymmetric laminates by Hyer in the 1980s [10]. Dano and Hyer explained the bistable nature of such asymmetric laminates with different layups and successively developed an analytical model based on the Classical Lamination theory[11, 12, 13, 14]. This provided a platform for various follow-up studies by other researchers focusing on the snap-through behavior of laminates and understanding the curvature characteristics. They explored by creating multi-patch models, and morphing applications in various fields such as automobiles[2], aerospace[15, 16, 17], and even architecture[18, 19]. In addition to morphing, vibration isolation [20] and energy harvesting [21, 22] were also feasible with multi-stable composites. Compared to the equivalent linear systems that work ideally only near resonance frequencies, multi-stable composites perform well across a wider frequency bandwidth [23]. Such broadband advantage is especially evident when the laminates vibrate between their two stable states (aka. inter-well snap-through responses). Harnessing such multi-stability and snap-through has yielded a wide spectrum of adaptive functionalities [24]. Shape morphing is the most extensively analyzed example. Multi-stable composites have several advantages that make them uniquely attractive for such a purpose: i) they need no constant power supply to maintain their shapes at stable states; ii) the snap-through typically features a large deformation and short response time, and iii) fiber composites inherently have high stiffness and strength-to-density ratios. Therefore, multi-stable composites are promising light-weight and multi-functional structural systems.

1.2 Motivation and Research Question

Bistable laminates have been studied so far to understand their curvature characteristics with composite layup changes, their snap-through loads (or moments), and their performance for energy harvesting efforts. Upon careful observation, one may realize there are two important directions associated with these laminates, one is the *out-of-plane direction* i.e. in the perpendicular direction of the laminate surface, and the other is *in-plane direction* i.e. in the surface of the laminate. Many researchers have focused on understanding their out-of-plane characteristics as for snap-through an effective load (or moment) needs to be applied in this direction. [25, 26, 27] Though, we observed an important research gap in these bistable laminate studies — understanding their transient snap-through mechanics that depend on the load location and boundary conditions, with specifically characterizing their different snap-through behaviors. Whereas, for the in-plane characteristics of the bistable laminates remains largely unexplored with only few handful studies tried to explore this domain. [17, 28, 29]. Hence, we deem that exploring their in-plane compression responses at their two states would give the readers a complete understanding of the material behavior. This study also aims to provide a multi-functional purpose to these well-known bistable laminates through learning from above studies and show innovative ways of incorporating them into morphing structures. The morphing structures mean they can morph themselves to adapt to their surroundings and improve their performances such as morphing airframes [28], robots for advanced motions like crawl, climb and mimic animals. [30]

Recently, many researchers have looked at ancient Japanese art forms of paper-folding called *Ori-gami* and *Kiri-gami* as potential answers to achieve complex shapes and flexibility in the morphing structures. The word origami comes from the following root words – 'ori' means 'to fold', 'gami' means 'paper', and 'Kiri' means 'to cut'. This art form could have umpteen benefits in engineering, especially in fields such as metamaterials[31, 32, 33, 34**?**], morphing topologies (transforming from 2D shape to 3D shape)[35], and auxetic materials (negative Poisson's ratio or negative thermal expansion coefficients)[31, 36]. Most often, the folding principles at the basal level emerge from the nature of things around us. For example, the famous 'miura-ori' pattern is inspired by the geometry of leaves from beech/hornbeam trees whose surface has a corrugated shape that is initially packed inside a bud. This bud opens up during the spring season by actuating the distributed flow vessels (veins) through the leaf body and opening the leaf geometry in the process. The Miura-ori has the auxetic property, i.e., the folded geometry opens and expands in both perpendicular directions even if stretched in one direction. Such examples are abundantly available, and the real question is how we learn from them and apply them in the engineering field. The following figure 1.1 shows a few patterns of origami that are inspired by the deformation of 2D- and 3D-surfaces.

Now, knowing the capabilities and immense potential of using Origami and Bistable composite laminates individually, we pose an important question – **can we combine their properties to create even smarter structures that would have on-demand ability to *switch* their performance characteristics and *lock* into multiple configurations?** The answer to this question is addressed through three leading studies – first, by understanding the snap-through behaviors of a simple square bistable laminate under out-of-plane transient loading and asymmetric boundary conditions (bistability); second, we study the behavior of this bistable laminate under in-plane compression loading (elastic instability) in two different stable states and show their switchable performance and; third, an origami-inspired waterbomb laminate structure that can enhance the design space with introducing

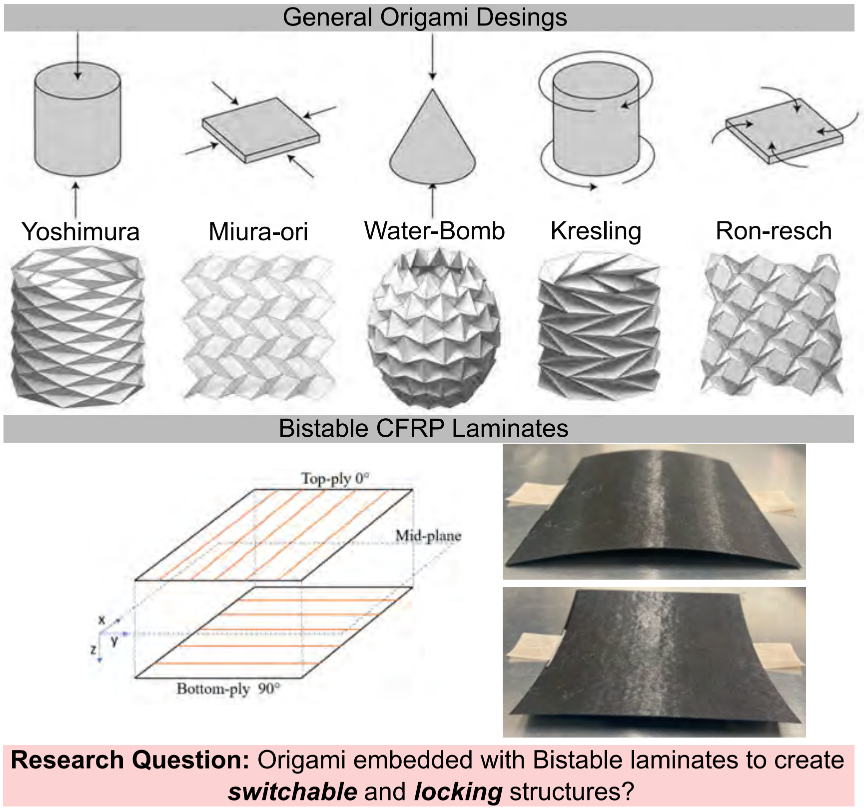

Figure 1.1: (a) General Origami Designs [37] that are inspired by the deformation of some 2D- and 3D-surface geometries. (b) Bistable CFRP laminate is a result of asymmetric ply layout about the mid-plane. The figure shows two stable shapes of the laminate. Notice the curvatures in both the states are mutually inverted and perpendicular.

locking feature to morphing structures.

1.3 Intellectual Merit

Originality: The study investigates the bistable laminates from a holistic perspective by understanding their quasi-static behaviors in mainly two important scenarios i.e. Out-of-plane and In-plane direction loadings. For the out-of-plane direction, many research studies have focused on snap-through characteristics and applications without really understanding the underlying snap-through mechanics of these laminates with asymmetric boundary conditions. The authors, in their first study, uncover these different snap-through mechanics that depend on the loading and boundary condition. Essentially, the study would help in designing actuation strategies for these laminates depending on their usage, either for energy harvesting, actuating morphing structures, etc.

This study, for the first time, carefully explores the in-plane compression characteristics to uncover the elastic instability in these bistable laminates. The study further discusses two drastically different stiffness responses in their two different states. Upon identifying specific parameters, these in-plane behaviors can be tuned, even on-demand, to enhance their stiffness switching ratio. This sets the base for achieving switchable performances within morphing structures by incorporating such bistable/multi-stable elements.

Learning through these behavioral characteristics of bistable laminates, one starts to ponder the immense possibilities of utilizing them in morphing structures. We, for the first time, present a 'locking' feature by harnessing characteristic curvatures of these bistable laminates and strategically implementing them in morphing structures. We take inspiration from various origami folding patterns and incorporate these bistable laminates in them. This helps in changing the load-bearing capabilities of the structure by switching from a very soft foldable state to a lockable stiff state. We present a case study on two origami designs, namely Kresling and Yoshimura, where using this bistability property delivers massively reconfigurable structures that show meta-stable load-bearing states.

Hence, amalgamation of these two technologies provides strong base to create — compact, energy efficient techniques to achieve switchable performance, particularly in terms of stiffness properties changing from soft to rigid and vice versa. These could be envisioned at advanced space technologies such as in-space manufacturing robotic arms that show maneuverability with load-bearing capabilities to handle tools. To minimize the complexity of controlling such large space structures [38, 39, 40], it is necessary to create robust mechanisms for deploying structures to avoid alignment errors and vibrational losses [41, 42]. Hence, the use of origami technology can provide a controlled deployment strategy that minimizes the actuation requirements. Hence, this study should inspire future research to harness bistable laminates in morphing technology.

1.4 Thesis Outline

The above imposing question is answered through a series of studies. The following outline presents a brief look into my research study:

1. **Chapter 2**: Out-of-plane snap-through behaviors

   This section briefly explains the snap-through behavior of a simple bistable CFRP laminate that depends on the boundary conditions – fixity constraints and location of force applied. The study shows three distinct modes or paths of snap-through for the laminate depending on the location of the applied force. It provides useful information on the methodology of obtaining these behaviors and the placement or design of actuators depending on the desired deformation path.

2. **Chapter 3**: In-plane compression behavior of bistable laminates

   The chapter explains in detail the two distinct in-plane compression stiffness behaviors of bistable laminate. These behaviors could be interchanged through simple snap-through of laminates from one stable state to the other. It lists the details of the novel fabrication method, which introduces a flexible connection to the laminates and the effects of asymmetric boundary conditions with friction interplay. Then three different strategies are discussed that could be used to improve the stiffness behavior. With comprehensive experimentation and a semi-empirical analytical model, we validate the predictions. At the end, discuss methods to create switchable sandwich structures.

3. **Chapter** 4: Folding laminates

   This chapter pitches a potential design paradigm for creating folding laminates that could be leveraged to create multi-stable morphing structures. The research proposes to utilize the bistability of CFRP laminates with origami-inspired panel geometry to embed 'locking' feature. This feature brings a more energy-efficient way to create load-bearing stable states for morphing structures as both origami and bistable laminates require only mechanical actuation (low-level form of energy compared to electrical, thermal, or magnetic) to change overall properties. Using this idea, we also present a case study that explores two origami patterns, namely Kresling and Yoshimura, showcasing the possibility of combining bistable technology with origami structures. Future work is discussed later in the chapter 5.

In parallel, we developed a new lamination theory formulation for bistable laminates that differs from the Classical Lamination theory (CLT) on the use of high-order plate theory. In the CLT, they use Kirchoff's plate theory that ignores the interlaminar stresses (τ_{xz} and τ_{yz}) that play a crucial role in the bistable laminates for balancing the moments, particularly at the free edges. Hence, we present a separate chapter as an additional study that, for the first time, uses the first-order shear theory of plates in combination with CLT for shape prediction of bistable laminates. It also explains in detail the extensions for this high-fidelity analytical model to predict multi-patch systems of bistable laminates and also includes a hygroscopic degradation factor to predict the change in their shape and snap-through property.

Chapter 2

Summary of Previous Study: Out-of-plane snap-through behaviors

Publication Details

Other Authors: Oliver Myers, Georges Fadel, Suyi Li.

Title: "Transient deformation and curvature evolution during the snap-through of a bistable laminate under asymmetric point load"

Journal: Composites Science and Technology, vol. 211, p. 108871, 7 (2021).

Asymmetric laminates with appropriate dimensions and layup properties [43] show bistability, i.e., they show two stable states and could be changed from one state to the other. This phenomenon of shape change from one state to another is called the *snap-through* process. An effective stimulus (force, moment, or pressure) in the out-of-plane direction is typically required for a laminate to change its shape. And, it is observed that this snap-through behavior depends on the boundary conditions applied to the laminate. Hence, we addressed an imposing question in my master's thesis [44] – **does the laminate snap-through always follow the same path?**

Most of the literature studies on bistable laminates focus on –static analysis such as predicting the stable shapes of the laminate by varying parameters (ply orientations, number

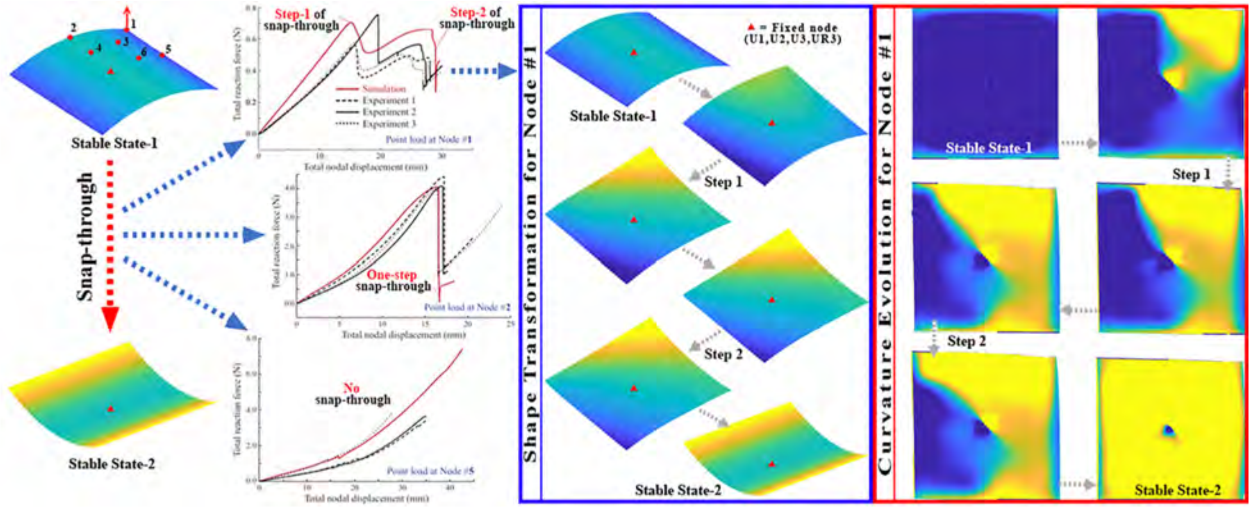

Figure 2.1: Summary: A simple bistable CFRP laminate of configuration [0°/90°] can show three different paths for snap-through process from stable state-1 to stable state-2. They are categorized as: two-step, one-step, or no-snap process depending on the location of out-of-plane force applied to the laminate. A displacement profile change is shown inside the blue box for the case when the laminate experiences force at the Node #1. The corresponding curvature changes in the laminate are shown in the red box, where the curvature front –marked at the separation of yellow(positive curvature) and blue (negative curvature) region – progresses through the laminate with starting at the node where the force is applied. The curvature front first progresses on the vertical edge and meets the bottom edge. In the second progression, the front reaches the left edge and completes the curvature inversion of the laminate.

of layers, dimensions, etc.) through various analytical formulations[45, 46], and optimizing these parameters for desired topological shapes by combining different laminate configurations [43, 47, 48], and dynamic analysis such as natural frequency predictions, cross-well free-vibrations of simple cross-ply laminates [16, 24], etc. But all of them had one common factor i.e. these studies have *symmetric* boundary conditions, and hence different snap-through characteristic paths are far less studied. All the forces and fixity constraints have a symmetric distribution across the center line of laminate geometry, and hence the laminate usually follows a one-step snap-through.

We addressed the above shortcoming by introducing *asymmetric boundary conditions* for a simple asymmetric cross-ply laminate of configuration [0°/90°] that has two stable shapes as shown in the figure 2.1. And we apply minimum boundary conditions by fixing the laminate at its centre for all the degrees of freedom and apply a de-stabilizing force in the out-of-plane direction at one of the selected node points on the laminate. A total of eight nodal points are selected in one quadrant, as there are two planes of symmetry for the laminate's displacement profile. The snap-through path is observed to vary with the location of selected node on the laminate (refer to the stable state-1 in the figure 2.1, it shows the six selected point inside one top-right quadrant) – **one-step** snap-process is observed for all the points on the axis joining the centre node and the Node #2, i.e., the Node #4 also shows a one-step snap process; **no-snap** process for all the point on the axis joining the centre node and the Node #5; and everywhere else inside the quadrant, the laminate takes **two-step** snap process. The snap-through requirements are also observed to vary with the different snap-through paths, the laminate required more force and lesser snapping-displacement before changing its shape from one stable state to the other if the location of the force is on the axis joining the Node #2 and the center node when compared to that node being at the corner side.

Regardless, this study's results can offer valuable insights into the fundamental mechanics of snap-through behaviors and the actuation locations associated with the bistable composite laminates. The out-of-plane actuation used in this study has unique advantages compared to in-plane actuators, such as embedded piezoelectric patches, because the latter could hinder bistability due to their additional stiffness [49]. And this study's result could serve as a guide, allowing the user to choose the actuation force's location based on the snap-through mechanics. One could first examine the characteristics of different snap-through processes and then select the actuator's position according to its capability. For example, if the [0°/90°] patch is selected and the actuator has a high block force but low stroke (e.g., piezoelectric actuators), one can place the actuator at any point along the axis joining the Node #2 and center.

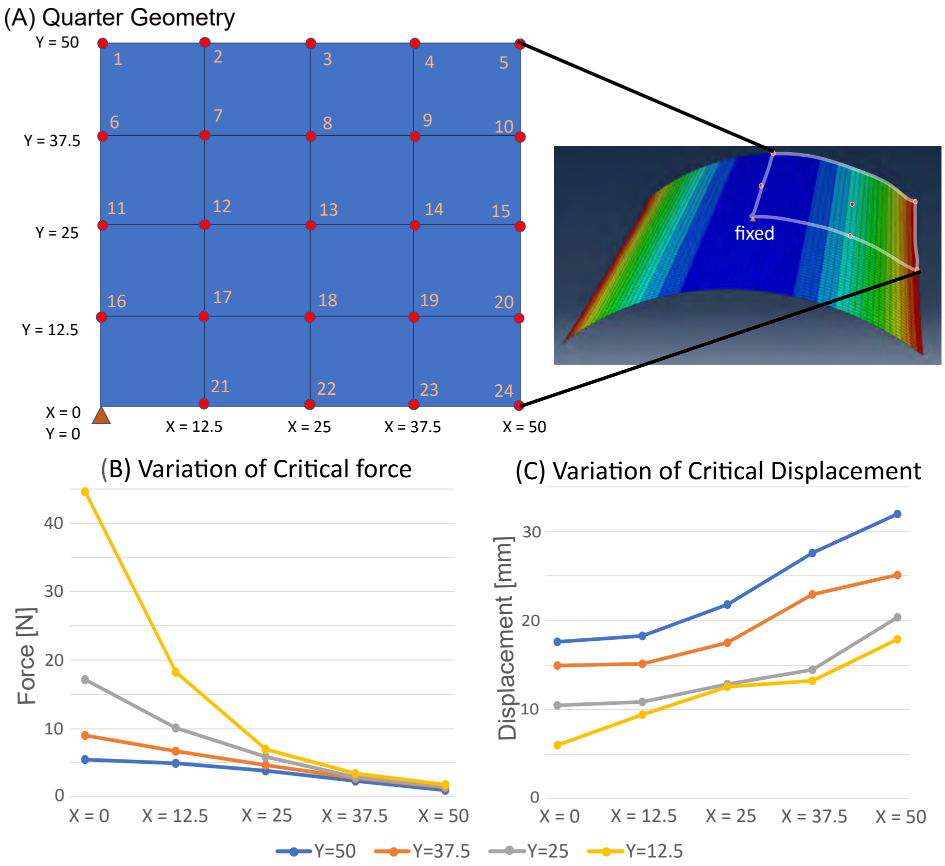

Figure 2.2: Comparison of Snap-through requirements for [0°/90°] laminate depending on the location of the loading node.

This is because the corresponding snap-through involves a single step with minimal displacement requirement. On the other hand, if the actuator has a high stroke but low block force (e.g., shape memory polymers), Node #1 is the favorable actuating location as the critical force requirement is the least. An overall summary of snap-through requirements could be understood from the figure 2.2 which shows the variation of critical force and critical displacement needed in order to change the shape of a [0°/90°] laminate based on its actuation location. A preliminary actuation energy estimates for the snap-through process is calculated from the area under the force-displacement curve observed for different cases shown in the table 2.1.

The learnings from this study would help us guide in the methodology of first, selecting the

Node location	Node #1 (One-step)	Node # 5 (Two-step)	Node # 11 (One-step)	Node # 13 (Two-step)	Node # 24 (No snap)
Work to snap (mJ)	32.18	13.46	47.85	20.06	Inf

Table 2.1: Snap-through energy estimates based on the actuation location for $[0°/90°]$ laminate. The work to snap is calculated as the area under the curve from the finite element simulation results. Refer to the figure 2.2 for the node locations.

right actuator for a bistable mechanism according to the force requirements, and second, the location of the actuator for a defined/desired snap-through path and permissible displacement to change shape from one state to the other. A similar method is (will be) used in the chapter 3 to choose an actuator for the robotic structure. We now discuss another dimension of bistable laminates, which are loaded in an in-plane direction. We use the results to develop switchable structures that change their nature from very soft to very stiff and vice-versa.

Chapter 3

In-plane compression behavior of Bistable laminates

3.1 Introduction

Stiffness-tuning materials and structures that can switch between being soft and stiff on demand have been crucial to many advanced engineering systems [50, 51, 52]. For instance, a morphing aircraft wing must be soft to adapt its external shape for maximum aerodynamic efficiency yet become rigid enough when necessary to withstand wind gusts [28, 29]. An ideal soft robot should be able to switch between being flexible to maneuver through confined working spaces and stiff to carry payload [51, 53, 54, 55]. Future automobiles, especially electric ones, can benefit from adapting their suspension stiffness to upgrade the driving experiences [56, 57]. To this end, we have witnessed the emergence of a wide variety of stiffness tuning (also called variable stiffness) methods with vastly different operating principles(electrical, magnetic, mechanical, pressure, etc.), ranging from responsive materials that can change their intrinsic constitutive properties (e.g., shape memory alloys (SMAs) [51, 58, 59, 60] and polymers (SMPs) [61, 62, 63, 64, 65]), meta-structures that can transform their underlying architectures (e.g., multi-stable origami solids [32, 66, 67]), to cleverly designed mechanical systems that can adjust its internal working conditions (e.g., electrostrictive layer jamming, ELJ [8]).

However, state-of-the-art stiffness tuning materials are limited by two significant constraints. First, many stiffness tuning mechanisms require a continuous and sometimes substantial power supply to initiate and maintain the stiffness change, making it challenging to implement in practical, real-world scenarios. For example, the SMPs are temperature sensitive and need to be maintained to keep the material in a particular shape, and ELJs need to be supplied with a constant magnetic power to increase the bending stiffness of the material. Second and more importantly, there has been a trade-off between the achievable stiffness change and the load-bearing capacity at the stiff state. To compare these different state-of-the-art materials/structures with our bistable laminates, we present a plot in the figure 3.1 that evaluates their normalized load-bearing capacity with their stiffness variation ratio. The normalized load-bearing capacity is calculated using the nominal stress induced at their critical loads (varies with their operating modes such as tension, compression, bending) and divided by the specific gravity of the material to eliminate the bias of the material weight. Next, we choose representative materials based on their actuation methods, such as for electrical actuation - SMA wire and manipulator, for electro-magnetic actuation - ELJ beam, for pressure actuation - fluidic flexible memory composite, for temperature actuation - SMP and SMPC, and mechanical actuation - Origami-TMP. In addition, we associate a qualitative energy cost of operation with these materials based on the form of energy used. Three classifications - high energy cost (electrical, magnetic) marked as red dots, moderate energy cost (temperature, pressure) marked as yellow dots, and low energy cost (mechanical) marked as green dots. Due to the lack of evidence, a quantitative measure of energy dispensed for all materials is difficult to calculate, and hence, only qualitative measure is used based on the cost associated with harnessing energy sources. Now, the heat-responsive SMA wire can carry a large amount of load (in tension) but has a relatively small change in stiffness between its austenite and martensite phases ($<$ 10 high/low stiffness ratio). On the other end of the spectrum, elastic memory composites (EMC) [68, 69] and SMPs [61, 62, 64] can achieve relatively larger high-low stiffness ratios (≈ 100) and carry high loads in tension but fail to operate in compression (Figure 3.1). Other modes of deformation, such as bending shown by ELJ [8] and compression shown by Origami structures such as the Tachi-miura polyhedron (Origami-TMP, mechanical reconfiguration), have low load-bearing capacity and limited stiffness variation ratio. Flexible fluidic memory composite (F^2MC)[9, 70] can achieve a moderate level of stiffness variation but lacks in carrying large loads.

Therefore, in this study, we find a way to overcome these two constraints and develop a large stiffness-ratio, high compression-load bearing capacity material system by harnessing the in-plane buckling and bi-stability of asymmetric carbon fiber composite laminates.

Asymmetric carbon fiber composite laminates have recently gained considerable interest for their potential to create multi-stable structures suitable for the automotive [2], aerospace [28, 71], and renewable energy industries [24, 72, 73]. These laminates have asymmetric ply angle layouts, such as [0°] in one layer and [90°] in the other. As a result, upon appropriate conditions, they become bistable from the internal energy mismatch generated during the thermal curing, showing opposite surface curvatures between the two states [45, 74] (Figure 3.2). Many studies have been conducted to uncover the correlations between the design [75, 76, 77], mechanics[44, 78, 79, 80], ambient conditions [81], and potential applications [2, 82, 83, 84, 85] of these bistable laminates. Though enough studies have looked into in-plane buckling of symmetric laminates [86, 87] with multi-objective optimizations [88, 89, 90], this aspect of asymmetric laminates is poorly understood. Except for an early exploratory study [17], all previous work has focused on the laminate's out-of-plane performance, and it stands imperative for us to explore in this direction.

We find that an asymmetric composite laminate exhibits two distinct stiffness behaviors when subjected to *in-plane* compression load at its two stable states — in one state, the laminate is very stiff as it carries the external load like a curved column structure, whereas,

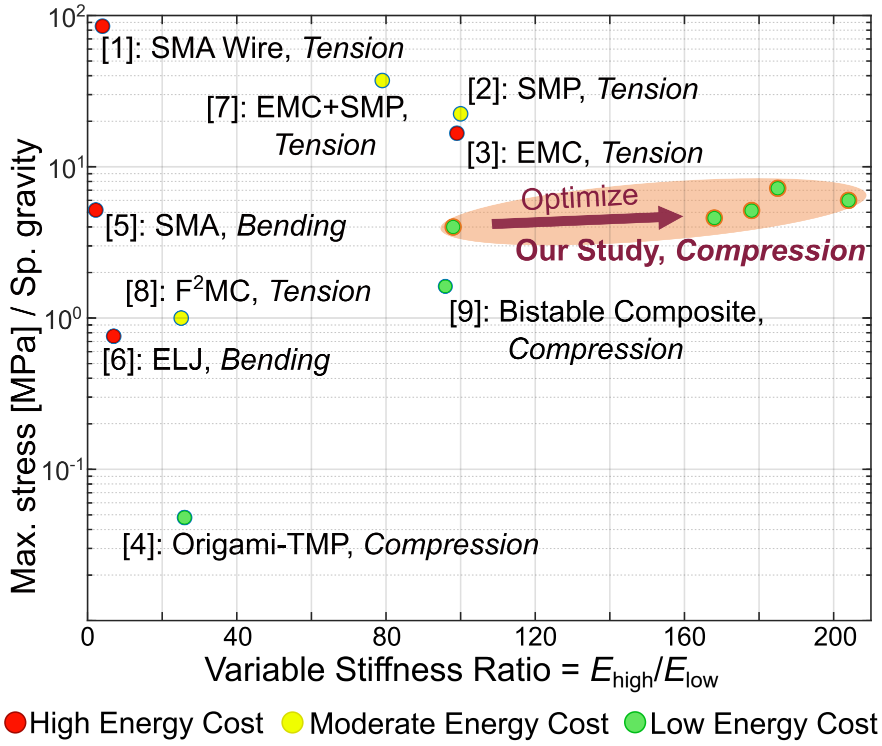

Figure 3.1: Comparing the performance of different variable stiffness methods. Here, we use three performance metrics: The high/low stiffness tuning ratio ($E_{\text{high}}/E_{\text{low}}$), normalized load-bearing capacity (Max. stress/Specific gravity), and energy consumption (High, Moderate, and Low). *It is important to note that lightweight structures inherently have a much higher loading bearing capacity in tension than in bending and compression.* Therefore, even though the bistable composite laminate in this study is loaded in compression, it can still provide a very large stiffness ratio and excellent compression load capacity with a small actuation requirement. (Technical details and references behind this figure are available in the Supplement section 3.6 of this chapter).
Note: Focus is on shape morphing, large-deformation materials that are used in the cm-scale-and-above applications.

in the other stable state, it becomes very soft and bends like a leaf spring. The bistable nature ensures an energy-efficient stiffness tuning, as actuation is required only to overcome the energy barrier between the two stable states [44, 82]. Once the laminate settles into the stiff or soft configuration, no more actuation is needed to maintain the change in stiffness. Moreover, composite is inherently lightweight and can carry high loads. Remarkably, we find that by simply adding a small lateral in-plane force (e.g., a rubber band shown in Figure 3.1), we can substantially increase the high-low stiffness ratio (up to 200) and load-carrying capacity at the stiff configuration, outperforming the state-of-art variable stiffness methods.

In the following section of this paper, we first briefly discuss the fabrication process of the composite laminate involving a flexible connection strip for assembly. Then, we thoroughly examine the physics underpinning the compression buckling of a square two-ply [0°/90°] laminate at its stiff state; such buckling is directly related to its load-bearing capacity. We find that different buckling modes and contact conditions play a crucial role. Based on these insights, we explore different strategies to enhance the stiffness switching performance and compression load-bearing capacity, including (a) adjusting the laminate's aspect ratio, (b) applying lateral loads, and (c) parallel stacking. In the end, we fabricate and demonstrate cellular structure concepts by carefully assembling these laminates into a square or hexagonal arrangement.

3.2 Design and Fabrication of the Switchable Laminate

When designing a modular, adaptive, and reconfigurable structure, it is critical to create the connections between its functional elements to accommodate their large and often non-uniform deformations. For our study, we need to develop a flexible connection between the bistable composite laminate and the end plates. Ideally, this connection should be soft in twisting/bending, tear-resistant, and bond well with the composite's epoxy matrix. After many trials and errors with materials like glass fiber sheets and fabric cloths, we found that the 3D-printed thermoplastic polyurethane (TPU) sheet provided us with the best results.

To fabricate the stiffness-switching laminate, we first use a layer of uni-directional carbon-fiber prepreg oriented at [90°] as the base. Next, we carefully place a 3D-printed TPU connection strip in the center. Finally, we add another layer of fiber prepreg oriented at [0°] on the top (Figure 3.2a). The vacuum bagging technique is used to cure the laminate

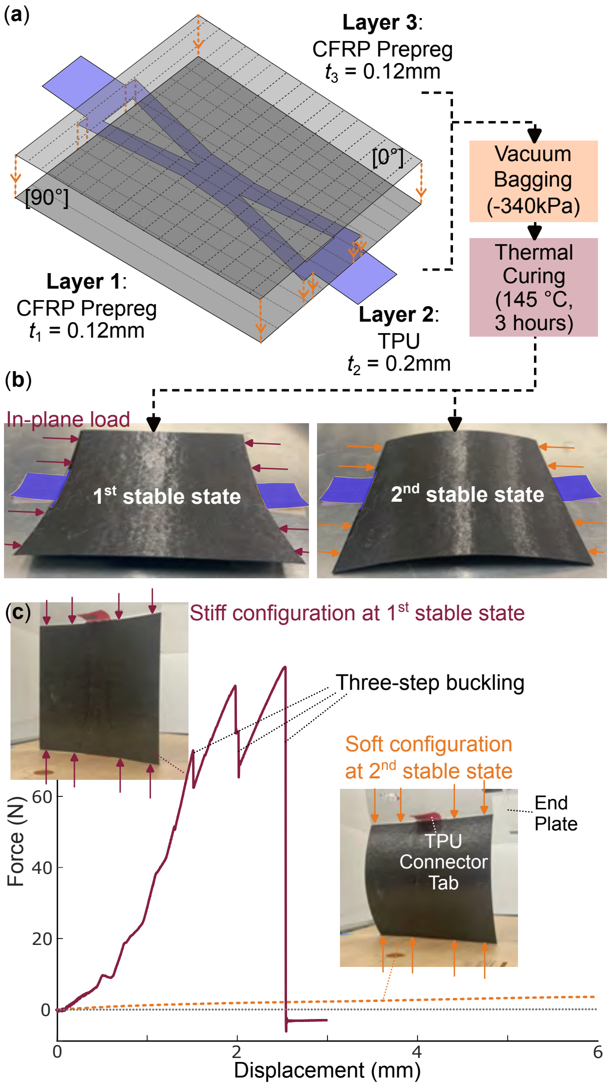

Figure 3.2: Design and fabrication of the stiffness switching laminate. (**a**) The bistable composite laminate in this study has a three-layered construction: CFRP prepreg with 90°fiber orientation, 3D-printed TPU connection strip, and another CFRP prepreg with 0°fiber orientation. (**b**) The two stable states of the cured laminate sample. (**c**) The radically different in-plane compression responses of a single laminate at its two different states. The force-displacement curves are testing results from a 100mm×100mm sample.

assembly (OV301 EasyComposites oven), with a carefully designed curing cycle to ensure strong bonding between the fiber laminates and TPU strip. Note that TPU has a glass transition temperature of 145°C, exceeding the fiber laminate's curing temperature at 121°C. After releasing the laminate at room temperature, we observe that it exhibits two stable states, as shown in Figure 3.2(b).

To effectively apply in-plane loading to the laminates, we sandwiched them between two acrylic end plates and attached the TPU strip's connection tabs to these end plates using double-sided adhesive tapes. The compression response of the final assembly is obtained on a universal testing machine (Instron 6500 with 100 N and 1000 N load cells). We observe two distinct behaviors for a single laminate: (1) A stiff response when the laminate starts from its first stable state and behaves like a thin column and (2) a compliant response when the laminate is in its second stable state and behaves like a spring. Comparing these two responses, like in Figure 3.2(c), reveals a remarkable difference in stiffness and load-bearing capacity.

Here, the force-displacement relationship in the stiff configuration is unique and intriguing. It starts from a rapid rise in reaction force, and then a unique "three-step buckling" occurs (indicated by the three distinct peaks in the force curve). The bistable laminate then snaps to the second stable state corresponding to the soft configuration. However, upon the removal of the compression load, the laminate can return to its first state (with some actuation), ready for the next loading cycle.

3.3 Understanding the Physics of Compression Buckling

Clearly, understanding and exploring the 3-step buckling is crucial for the laminate's performance at the stiff configuration, so we conduct extensive experiments and finite element simulations to uncover the underpinning physical principles.

3.3.1 Analysis of the 3-step Buckling

To further investigate the dual-stiffness behaviors of these bistable laminates, we measured the in-plane compressive responses from five 100mm×100 mm samples and summarized the results in Figure 3.3(a). Although the compliant responses of these samples were consistent (albeit nonlinear), the stiff responses varied considerably. This is not surprising because buckling, an elastic instability, is sensitive to boundary effects and fabrication errors. Nonetheless, the three-step buckling is persistent. Therefore, we use high-speed imaging and buckling mode analysis with finite element simulation to examine the underpinning physics (Figure 3.3b).

The test image at the occurrence of buckling Step 1, marked by the first drop in the force curves, involves a translation of the laminate's edges at the top corners. Such edge translation is also present in the first pair of buckling modes obtained from FEA (Modes 1 & 2 in Figure 3.3b). Here, Mode 1 has a symmetric deformation, while Mode 2 is anti-symmetric. The actual laminate deformation observed in the test is likely a combination of these two modes, depending on the contact friction between the laminate's edge and the acrylic end plates (more on this in the following section).

Besides the deformation pattern, we can also correlate the critical buckling force between test results and modal analysis. In the finite element simulation, the bucking force P_{cr} corresponding to each mode is

$$P_{cr} = \lambda_i Q_N \tag{3.1}$$

where λ_i is the eigen-value, and Q_N is the applied force. Hence, P_{cr} is 54N for Mode 1 ($\lambda_1 = 0.67$) and 56N for Mode 2 ($\lambda_2 = 0.7$). These are consistent with the measured buckling force at Step 1: 74 ± 18N.

In the test images corresponding to buckling Step 2, the laminate's right edge changes its

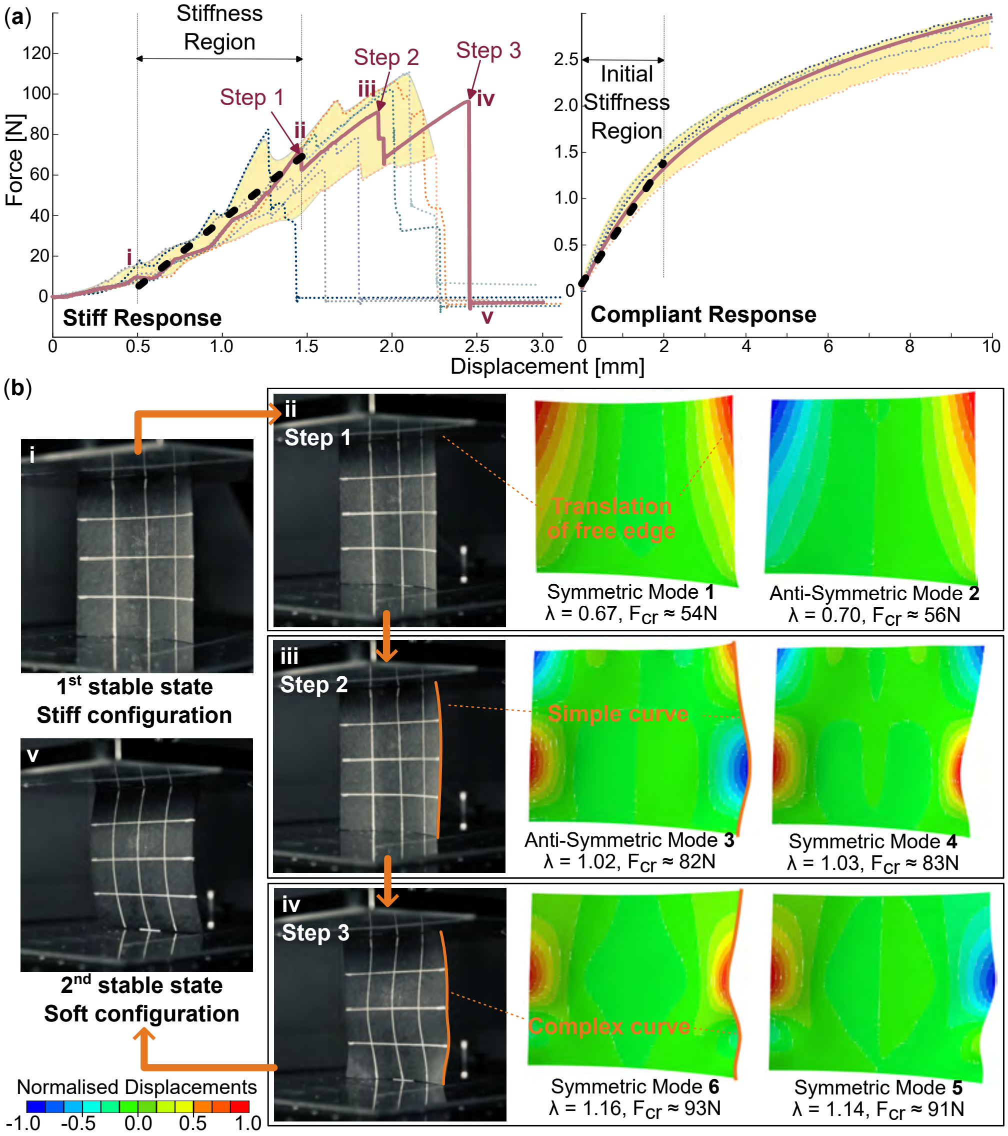

Figure 3.3: Compression and buckling analysis of 100mm×100mm laminates. (**a**) The force-deformation curves from seven loading cycles performed on five laminate samples. The red solid line is a typical response, the shaded yellow region covers the upper and lower limits of the test results, and the black solid line represents the fitted stiffness. (**b**) Test images showing the 3-step buckling deformation in stiff configuration and the corresponding buckling mode analysis using finite element simulations.

shape from a straight line to a simple curve, indicating that the right side of the laminate starts to invert its curvature. Such edge deformation is also observed in the anti-symmetric buckling Mode 3 and symmetric Mode 4 from FEA. The corresponding buckling forces P_{cr} are 82N ($\lambda_3 = 1.02$) and 83N ($\lambda_4 = 1.03$), respectively, agreeing with the test result of

79 ± 24N. In the final Step 3, just before the laminate completely snaps to its second stable state, its right edge deforms to a complex curve. Such deformation is also observed in the anti-symmetric buckling Mode 5 ($\lambda_5 = 1.14$, $P_{cr} = 91$N) and symmetric Mode 6 ($\lambda = 1.16$, $P_{cr} = 93$N). The experimentally measured P_{cr} of 89 ± 31N is consistent with the FEA predictions.

In the stiff configuration, we determine the laminate's effective stiffness by using the reaction force curve from 0.5mm displacement to the onset of buckling (rather than starting from 00mm due to the initial slackness from the gaps between the laminate's top and bottom edges and the end plates). On the other hand, for the compliant configuration, we calculate the effective stiffness over the initial linear deformation range from 0 to 2mm. Our test results showed that the averaged laminate stiffness is 68 ± 17 N mm^{-1} at the stiff configuration and only 0.70 ± 0.06 N mm^{-1} at the soft state, providing us with $\approx 97:1$ variable stiffness ratio just by switching between two stable states.

It is important to note that the 100mm×100mm laminate is very soft at its second stable state, generating only 3N reaction force with 10mm compression. As the compression load increases, the curvature of the laminate will increase, causing stress to concentrate in the center and eventually leading to failure (Additional Information Section 3.10). Therefore, in subsequent tests, we limit the compression deformation to below 15% strain.

3.3.2 Effects of Friction and Asymmetric Contact Conditions

During the compression tests, the laminate's upper and lower edges are consistently in contact with the end plates to transfer the external compression load to the laminate body. Understanding how this contact condition can impact the overall structural performance is essential. Upon examining the experiment results, we identified two critical factors that can significantly affect the occurrence of 3-step buckling. Firstly, the friction on the contact surface plays a vital role. Secondly, the laminate's edges are not always in perfect contact with the end plates due to fabrication imperfections.

We conducted another finite element simulation where the laminate's top and bottom edges were partitioned (Figure 3.4(a)). Denote 'A,' 'B,' 'C,' and 'D' as the laminate's upper left, upper right, lower left, and lower right edges, respectively (excluding the connection tab from the TPU strip). We divide these four edges using two reference lines positioned at a distance L_s and R_s away from the left and right edges, respectively. For example, edge A is divided into two parts: 1 near the laminate corner and 2 near the center. Such a setup helps create different combinations of contact conditions. In the finite element simulations, the contacting edges are defined by surface-to-surface contact pairs. Their normal behaviors are set as "hard-surface," and the tangential behavior is "frictionless" or "penalty friction" if friction effects are to be modeled. For further details of modeling, refer to the section 3.5.

First, we simulate the laminate's compression response in the stiff configuration without edge split ($L_s = R_s = 0$) or friction, and the result is the grey dotted line in Figure 3.4(b). Surprisingly, the laminate's buckling only has two steps. To replicate the 3-step buckling we observe in the experiments, we must introduce asymmetry in the edge contact conditions — by splitting up the laminate edges and introducing friction. Specifically, we denote the edge contact setup as "ABCD-Fric," where the first four values indicate the edge partitions in contact with the end plates, and "Fric" is the dry friction coefficient.

For example, if the setup is 1111-Fric=0, the outer parts 1 of edges A, B, C, and D are in contact with the end plates, but there is no friction. We found that with this contact setup, the 3-step buckling occurs as long as the partition lines' positions are asymmetric ($L_s \neq R_s$, for example, $L_s = 15$ mm, $R_s = 20$ mm). On the other hand, if the connection setup is 1211-Fric=0, the inner part 2 of edge B contacts the end plate instead, and the corresponding

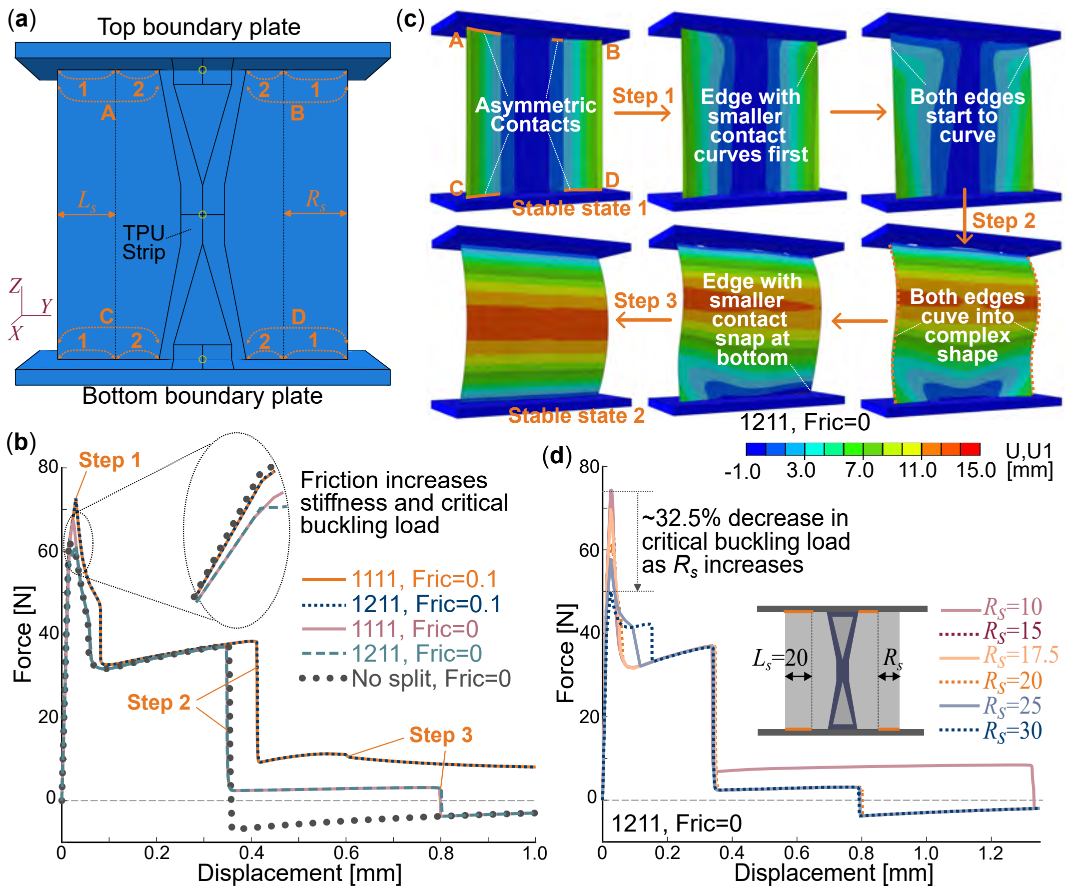

Figure 3.4: FEA Simulations reveal the effects of friction and asymmetric contact conditions. (**a**) Finite element setup, showing the four contact edges A, B, C, and D, as well as their partition by two reference lines. Here L_s, R_s are the variables. (**b**) Simulated reaction force curves with different contact condition setups. (**c**) Simulated compression buckling deformation for 1211-Fric=0. (**d**) Simulated force curves with different petition setups on the right side of the laminate.

compression response is similar to the 1111-Fric=0 case but with a reduced critical buckling load. This reduction could be because Part 2 of Edge B is shorter than Part 1.

Figure 3.4(c) details the compression deformation sequence of this latter example. The edge with a shorter contact ('B' in this case) deforms and translates first, generating the first step of the buckling. Then, the upper edge A follows, gradually deforming the left and right edges into complex curves (which we also observed in the experiment). In the second step of buckling, edge D (which has a shorter contact length than edge C) "snaps." Finally, edge

C moves and completes the buckling process.

If friction is involved, the laminate becomes stiffer, and its critical buckling load also increases. For example, the simulation result with contact setup 1211-Fric=0.1 shows a more prominent 3-step buckling and the corresponding critical load increases by almost 28% than the zero friction case. The laminate also deforms more in each buckling step, increasing the overall load capacity and stiffness.

We conducted further investigations on the asymmetric contact setup 1211-Fric=0 by varying the position of the partition reference line (R_s) while keeping L_s constant at 20 mm. The simulation results are summarized in Figure 3.4(d). We found that the critical buckling load drops significantly by $\approx 32\%$ as R_s increases from 10 mm (substantial contact between edge B and the end plate at its inner part 2) to 30 mm (minimal contact). This result verifies that the edge contact length determines the effectiveness of load transfer to the laminate body.

It is important to highlight that we do not intend to *quantitatively* match the simulated force-deformation curves from the FEA with the experiment results. As we have shown, the laminate's responses are sensitive to partial edge contact and friction coefficient, and these two factors are random and impossible to model accurately in FEA. Therefore, we do not expect the simulated laminate stiffness to agree with the experiment. Nonetheless, the simulated critical buckling loads are generally consistent with the test data.

3.4 Strategies to Optimize the Switching Performance

Once we understand the physics underpinning the compression buckling and the influences of asymmetric contact and friction, it is important to explore how to improve the buckling characteristics (like the critical buckling loads). Hence, in this section, we look at three approaches: a) adjusting the aspect ratio, b) adding lateral load, and c) parallel stacking the laminates.

3.4.1 Increase the Laminate's Aspect Ratio

Thus far, the laminate samples have a square geometry with a side length of 100 mm. Its aspect ratio (AR), defined as the ratio of the laminate's top edge length (b) over the side edge (a), is 1. If the aspect ratio deviates from 1, the laminate will take a rectangular shape. Consequently, bistability becomes asymmetrical in that one stable shape becomes "stronger" than the other (aka. it would require more effort to switch the laminate from one stable state to the other). Therefore, we systematically test laminate samples with aspect ratios $1.0, 1.5, 2.0$, and 2.5 for their compression behaviors.

The compression test results summarized in Figure 3.5(a) show a significant increase in critical buckling load as the aspect ratio increases. Surprisingly, we discover that such an increase in the critical force aligns with a shell buckling theory from NASA. This theory was initially formulated as a unified, semi-analytical approach to estimate buckling in curved plates and shells made of monolithic materials [91]. It categorizes the behavior of these curved structures as resembling either a flat plate or a circular cylinder, depending on the geometric and material parameters. In our study, the curved laminate falls into the latter category and the critical buckling stress σ_{cr} can be estimated as:

$$\sigma_{cr} = \frac{k_c \pi^2 E}{12(1-\nu^2)} . \frac{t^2}{b^2}, \tag{3.2}$$

where E is the effective elastic modulus, ν is the in-plane Poisson's ratio, b is the laminate's width, t is the thickness, and k_c refers to the coefficient of buckling stress. Here, k_c is

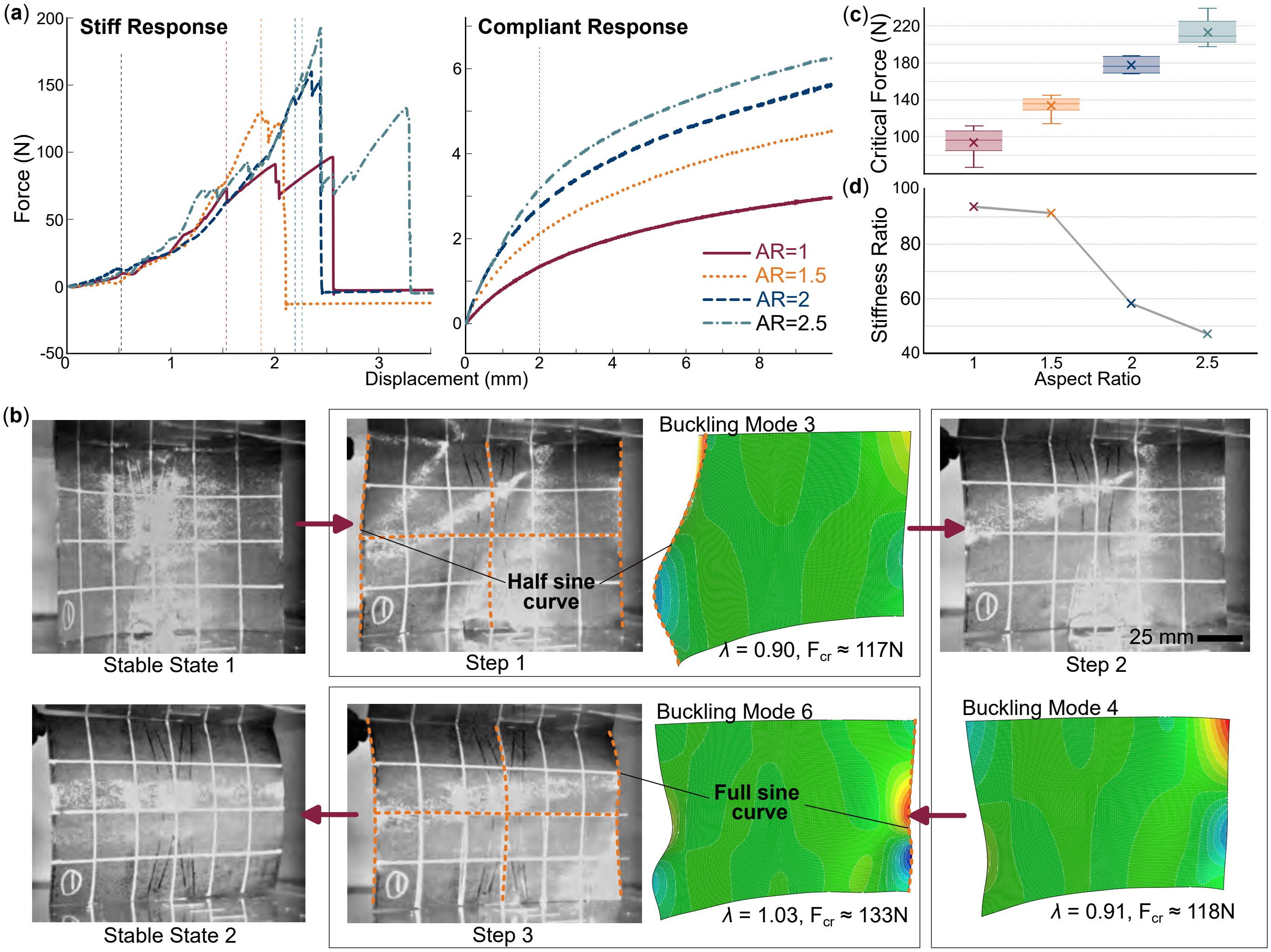

Figure 3.5: Examine the influences of aspect ratio. (a) Compression force-response curves for the laminates of aspect ratio 1.0, 1.5, 2.0, and 2.5. The first plot shows the results in the stiff configuration, while the second plot shows the soft configuration. (b) Sequential buckling of the laminate of $AR = 1.5$. Note: By looking at the critical modes in steps 1 and step 2, we see that the two modes are closely coupled with each other, which is also observed in the experiment images (refer to the orange lines). (c) Critical buckling loads increase as the aspect ratio increases. (d) The high-low stiffness change ratio, however, drops at the higher aspect ratio.

correlated to a non-dimensional geometric factor Z_b in that

$$Z_b = \frac{b^2}{rt}\sqrt{1-\nu^2}. \tag{3.3}$$

Note that this geometric factor is related to the radius of curvature r of the laminate.

AR	r/t	Z_b	Est. k_c	Exp. F_{cr}	Increase in F_{cr}	Increase in F_{cr} by Eq. (5)	Error
1	555	298	79	96N	-	-	-
1.5	555	671	178	136N	42%	49%	4.9%
2	555	1192	315	176N	83%	98%	7.5%
2.5	555	1863	492	216N	125%	148%	9.3%

Table 3.1: Aspect ratio and their estimated increase in the buckling loads.

NASA's curved plate buckling theory provided a set of nonlinear relationships between k_c and Z_b based on different ranges of r/t ratio (Figure 3.9 in the later section 3.5). Accordingly, we calculate the r/t ratio of the [0°/90°], 100mm×100mm laminate using finite element simulation. This way, we can obtain the k_c and Z_b values using the curves in Figure 3.9 and Eq. (3.4.1). The results are summarized in the first row of Table 3.1. This set of parameters from $AR = 1$ laminate becomes the basis for the following scaling analysis:

Eq. 3.2 indicates that $\sigma_{cr} \propto k_c$ and $\sigma_{cr} \propto 1/b^2$, where $AR = b/a$. Assuming the laminate's height a does not change, we can conclude $\sigma_{cr} \propto 1/AR^2$. Therefore, the critical buckling force

$$F_{cr} = \sigma_{cr} \times \text{Cross-sectional area} = \sigma_{cr}\, b\, t = \sigma_{cr}\, AR\, a\, t. \tag{3.4}$$

Therefore, we arrive at the critical scaling relationship:

$$F_{cr} \propto \frac{k_c}{AR}. \tag{3.5}$$

Based on this scaling law, we can use the compression test results of the $AR = 1$ laminate to predict the buckling force of other aspect ratio samples. For example, in the case of $AR = 1.5$ sample ($b = 150$mm), we first notice that the laminate's curvature r does not change with the aspect ratio ($r = 133$mm), so the ratio r/t stays the same. In this way, we can first calculate its Z_b parameter using Eq.3.4.1 and then estimate the corresponding k_c value based on the same master curve in Figure 3.9 in the later section 3.5. We found that the k_c of $AR = 1.5$ sample increases by 124% compared to the $AR = 1$ sample. Therefore, the scaling law of Eq. (3.5) predicts that the critical buckling force of the $AR = 1.5$ sample should increase by 49%, which agrees with the experiment data: $\approx 42 \pm 6.2\%$. Similarly, we compare the predicted buckling load increase for higher aspect ratio laminates with the test results, and we find that the semi-empirical theory could provide a very good estimation. The minor discrepancy between theoretical prediction and test result could be attributed to the limited availability of accurate correlations between k_c and Z_b, as well as experimental inaccuracies.

Increasing the laminate's aspect ratio can significantly increase the critical buckling load in their stiff configuration. However, this also leads to a decreased stiffness ratio between two stable states. For the $AR = 1$ square sample, the averaged stiffness ratio is 97. When the aspect ratio increases to 1.5, the ratio drops slightly to 91. However, if the aspect ratio rises further, the stiffness ratio decreases rapidly (59 if $AR = 2$, and 48 if $AR = 2.5$). Such a loss of switchable stiffness performance is because, as the laminate's aspect ratio increases, its stiffness increases in the soft configuration but remains relatively unchanged in the stiff configuration.

Therefore, as the laminate's aspect ratio rises, there is a trade-off between buckling load capacity in the stiff configuration and the switchable stiffness ratio. To circumvent this trade-off, we propose a different strategy of adding lateral force, as detailed in the following subsection.

3.4.2 Applying Lateral Force

Here, we introduce another strategy to enhance the compression performance of bistable laminates in their stiff configuration. We believe that applying lateral “squeezing” force to the laminate can increase its principal curvature and directly enhance the critical compression buckling load. To prove this idea, we conduct an experiment where two free-translating sliders apply lateral push force (F_L) to a 100mm×100mm square laminate under compression (Figure 3.6a). These slider mechanisms are actuated by free-hanging weights via strings, allowing us to control the magnitude of the lateral force precisely.

Due to the lateral force, the laminate’s curvature increases. Figure 3.6(b) shows the simulated laminate deformation profile and corresponding curvatures under different lateral forces using finite elements. The lateral loads are modeled as additional boundary conditions on the laminate’s vertical edges in this case. The laminate’s curvature rises by almost 74% even with a small 4N ($\approx$ 400 grams) lateral force. Consequently, the critical buckling load increases significantly by up to 68N (78% compared to the F_{cr} without lateral force). Such an increase in the critical buckling loads could also be estimated using the semi-empirical shell buckling theory introduced in the previous subsection. The geometry factor Z_b in Eq.3.4.1 is inversely proportional to the radius of curvature r (or directly proportional to the laminate’s principal curvature), so the buckling coefficient k_c increases as the laminate’s curvature increases. Given that the aspect ratio does not change in this case, the scaling law shown in Eq. (3.5) can be simplified to:

$$F_{cr} \propto k_c \tag{3.6}$$

We use the laminate’s compression performance *without* lateral force as the basis for comparison. First, we calculate the Z_b factors depending on the changing curvature and estimate

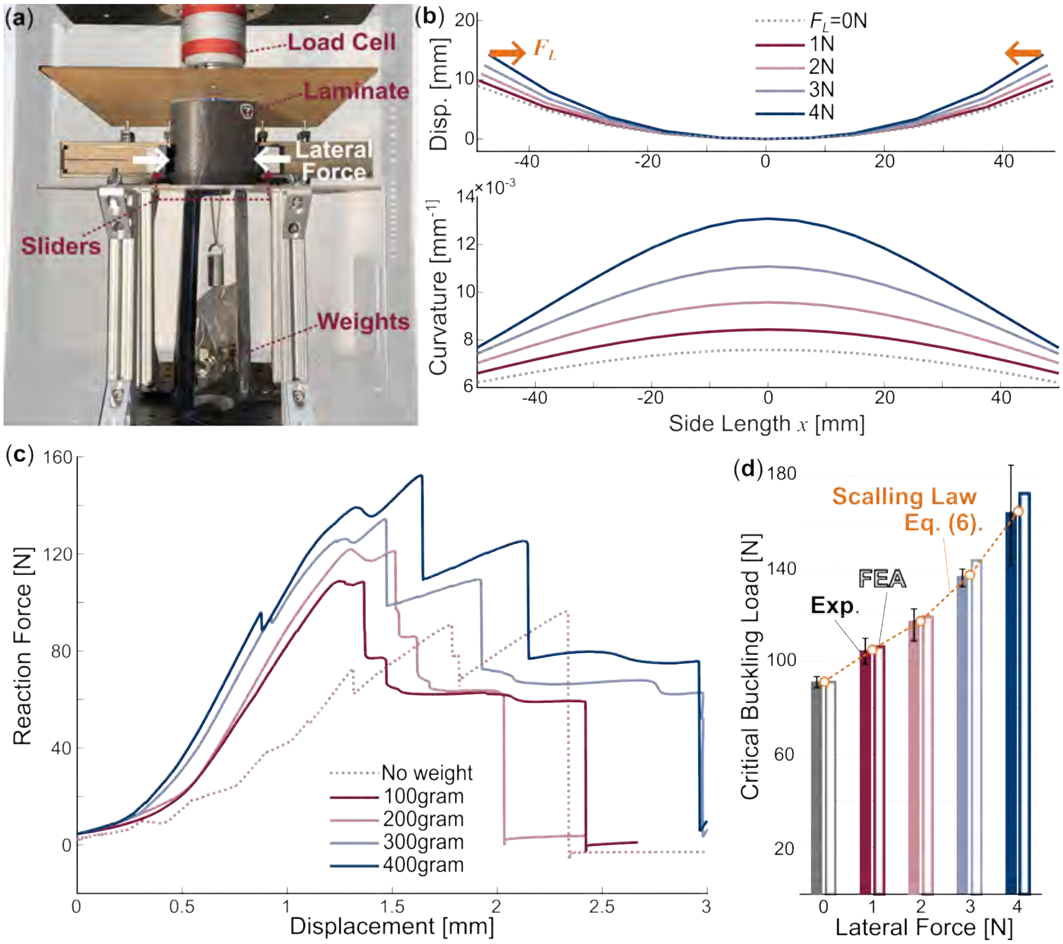

Figure 3.6: Investigating the influence of lateral force. (**a**) The experiment setup. (b) The top view of the laminate with different F_L from finite element simulations showing the different deformation profiles and corresponding curvatures. (**c**) The measured compression reaction forces. (**d**) Comparing the critical buckling load from experiment, finite element, and theoretical prediction. The experiment values are the averaged results from at least five loading cycles using two samples for each test condition.

the corresponding increase in the buckling coefficient k_c. (It is worth noting that we continue using the same curve correlating Z_b and k_c based on the original r/t ratio — as shown in Figure 3.9 in later section 3.5 — even though its magnitude drops with increasing lateral force.) The rising k_c directly translates to improving critical buckling loads, and the results are summarized in Table 3.2. The estimated buckling loads agree very well with the experimental results and finite element simulation, with errors less than 4%.

Remarkably, applying lateral force would not only improve the critical buckling force under

F_L (N)	$\kappa = 1/r$ (mm^{-1})	Z_b	Increase in k_c	Exp. F_{cr}	Measured F_{cr} increase	Error
0	7.5×10^{-3}	298	-	96N	-	-
1N	8.0×10^{-3}	318	6.7%	104.5N	8.9%	2.1%
2N	9.2×10^{-3}	366	22.5%	117N	21.9%	-0.5%
3N	11.0×10^{-3}	437	46.3%	136N	41.7%	-3.7%
4N	13.1×10^{-3}	521	74%	164N	70.8%	-1.9%

Table 3.2: Applying lateral force and the corresponding increase in buckling force, based on the analytical scaling law and experiment data.

compression but also increase the laminate's stiffness at the stiff configuration. As a result, we observe the high-low stiffness ratio increasing to 200 (Figure 3.1). This is probably because the compression load can better transfer from the end plates to the laminate with higher curvature.

3.4.3 Parallel Stacking with Multiple Laminates

An advantage of our switchable structure design is that we can easily sandwich multiple laminates between the end plates. This setup allows these parallel laminates to interact and work in unison toward the desired functionality. To this end, we assembled 2 or 3 square-shaped laminates to examine their collective buckling and switchable stiffness performance (Figure 3.7a). These tests can provide valuable insights into how the switchable structure's performance can scale with many laminates.

First, we tested three laminate samples individually — each with four compressive loading cycles at their stiff configuration — to measure their average critical buckling force and stiffness. Additionally, we use finite element simulations to estimate the buckling force, and the predictions show less than 10% error compared to the experimental results.

Then, we analyze the results from 2-laminate assemblies with all the possible pairings among

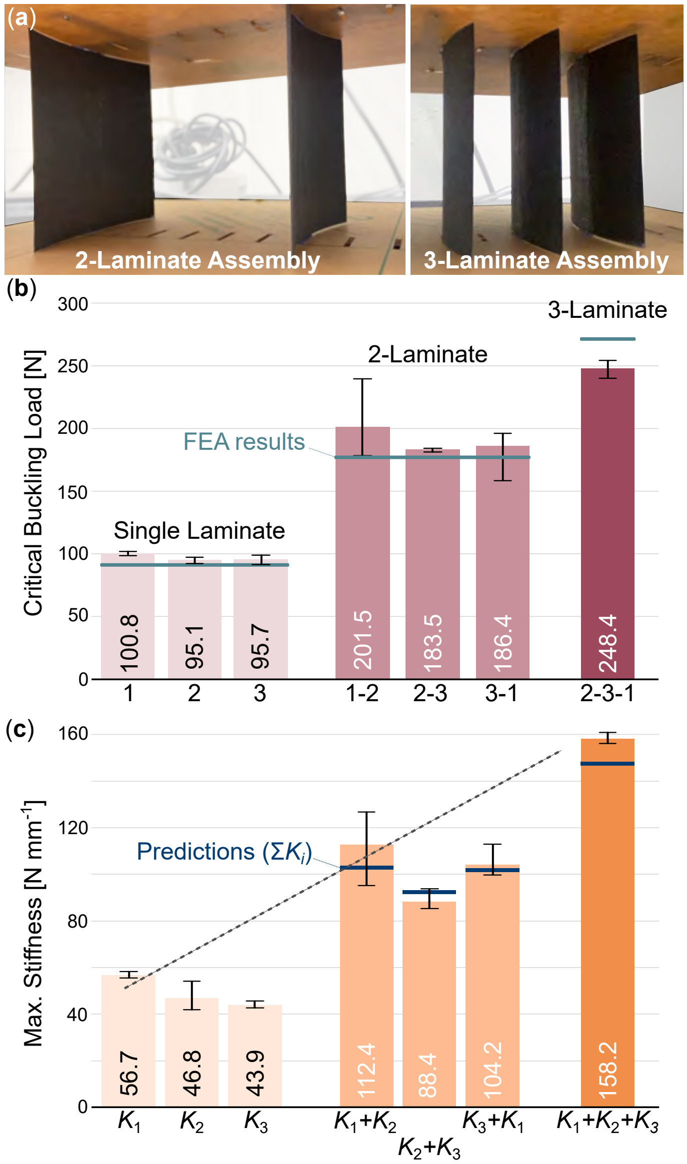

Figure 3.7: Use parallel stacking to improve the switchable structure performance. (**a**) The 2-laminate and 3-laminate assemblies in the test. (**b**) Critical buckling loads from single laminates, 2-laminate, and 3-laminate assembly. Here, we label the three laminate samples as '1,' '2,' and '3.' The vertical bars are averaged test results from four compressive loading cycles, and the error bars are the associated deviation. (**c**) The corresponding stiffness of single laminates, 2-laminate, and 3-laminate assemblies.

the three laminate samples (the bar plots in Figure 3.7b-c). The laminate combinations of 1 and 2 provided the highest buckling load (201.5 ± 30.5N over four loading cycles), and the corresponding stiffness is 112.4 ± 17.7 N mm^{-1}. Overall, the buckling load of a 2-

laminate assembly is about two times that of the individual laminate (this trend is in good agreement with the finite element predictions using two identical laminates and contact conditions). Meanwhile, the measured stiffness of the 2-laminate assembly is also very close to the summation of individual laminates with less than 10% variation (Figure 3.7c). These results indicate that the two composite laminates can distribute the external load between them evenly. It is worth noting that the distance between the two laminates has no significant influence as long as the external compression force is applied evenly. Otherwise, we will observe one laminate buckle before the other, hindering the overall performance.

The results from the 3-laminate assembly are relatively complicated. The critical buckling load measured experimentally is lower than the results obtained from the finite element simulations. Ideally, all three laminates should come into contact with the end plates simultaneously. However, during the experiment, we observed a “delay” in which the end plates had to deform by a minor initial strain before the three laminates could bear the load together. Moreover, once the external force reaches the critical level, the weakest laminate will buckle and snap to its second (soft) stable state rather than all three laminates snapping together. As a result, the experimentally measured critical load from the 3-laminate assembly is smaller than the summation of those from individual laminates.

This discrepancy is probably due to the inevitable fabrication imperfections in laminate geometries and their assembly. As a result, the three laminates are not identical in the experiments. Uneven loading conditions could be another factor: The universal testing machine can only provide a single point load, so we implemented a plunger attachment to convert this point force to a line force. However, it is still very challenging to distribute the external force evenly.

Regardless, the overall stiffness, calculated over the deformation range where all laminates are carrying the external load, is still consistent with the summation of individual laminate stiffness.

Our parallel stacking experiments have demonstrated that placing multiple laminates between two end plates can effectively increase the load-bearing capacity of switchable structures. It is critical to distribute external loads uniformly across all laminates and minimize fabrication imperfections (so they are as identical as possible). Realistically speaking, the switchable structure's stiffness scales well with the multiple-laminate construction, but the critical buckling force may not scale as well because some laminates will inevitably buckle before others.

3.5 Discussion and Conclusion

The use of bistable carbon composites with an asymmetric [0°/90°] fiber layout has been widely researched for adaptive structure applications. However, there have been no systematic studies on its in-plane response under compressive load. This study filled this gap and elucidated how bistable composite laminates can provide switchable in-plane stiffness responses in two different states — *stiff* response where the laminate behaves as a thin curved column, and *compliant* response where the laminate bends like a nonlinear spring — with a high/low stiffness ratio up to 200. Such significant stiffness variation originates from the laminate's principal curvature inverting between its two states.

Through extensive experimentation, finite element simulation, and theoretical analysis, this study thoroughly examines the physics behind the multi-step buckling of the bistable laminate when it is in its stiff configuration, as well as the impact of asymmetric contact conditions and surface friction between the laminates and end plates. Additionally, we explore various strategies for increasing the critical buckling force, enabling the structure to bear more load at its stiff configuration. These techniques include increasing the aspect ratio,

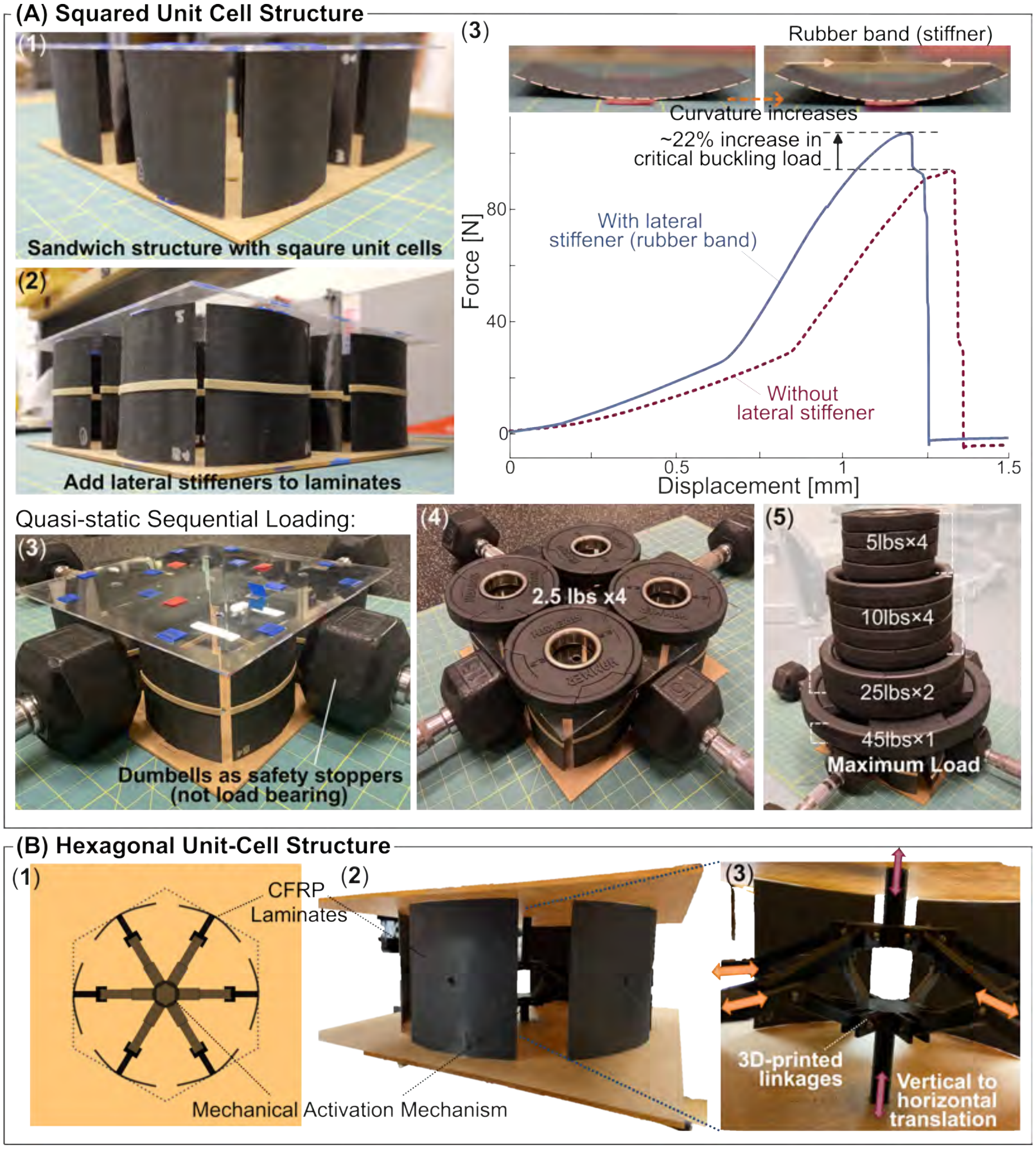

Figure 3.8: Two examples of switchable sandwich structures using bistable composites. (A1-A2) A close-up view of the square-shaped unit cells before and after applying lateral stiffeners (rubber band). (A-3) With the rubber band, the curvature of the bistable laminate changes, increasing its critical buckling load by 22%. (A3-A5) Quasi-static loading of the switchable structures containing four square cells (16 laminates). Dumbbells were first placed between the end plates as emergency stoppers (but they do not carry any load). Then, four 2.5-lbs weights are placed on top of the four cells to ensure even load distribution. Eventually, the switchable structure sample supported a weight of 165 lbs before buckling. (B1-B3) Another cellular structure example with a 3D-printed linkage-slider mechanism to convert vertical input to lateral forces, switching the laminates between stiff and soft configurations (Supplement Video 02).

stacking multiple laminates in parallel, and applying lateral force. With this new knowledge, we present a novel class of sandwich panels that could switch their stiffness on-demand by setting its bistable laminates in two different configurations.

For example, we constructed a squared unit cell structure, and each unit cell consists of four [0°/90°], square-shaped laminates (Figure 3.8(A1-5)). This sample structure has four unit cells with 16 laminates in total. Since our studies in Section 4.2 revealed that a small lateral force on the laminate can significantly increase the load-bearing capacity, we add lateral stiffeners (simple rubber bands) to the laminates (Figure 3.8A2-3). These rubber bands alter the curvature of the laminate and increase their critical buckling force by 22%. As a result, the switchable structure, which in total weighs only 604 grams – of which all the laminates only weigh 84 grams, rubber bands weigh 15 grams, and end plates are approximately 250 grams each – supported 75 kilograms of weight before laminate buckling giving a very large compression load-to-weight ratio of 893 (considering only the laminates' weight).

In another switchable structure example, we explore effective methods to snap the bistable laminates on demand between stiff and soft configurations. This example is inspired by the honeycomb structure, and it has one unit cell with a hexagonal arrangement of six bistable laminates (Figure 3.8B). This sandwich panel prototype can support up to 27 kilograms (or 65 lbs) of load in total in the stiff configuration. To implement on-demand stiffness switching, we designed and 3D-printed a double-slider mechanism that converts vertical inputs into lateral forces. This lateral force is directed toward the center of bistable laminates, shifting them between stiff and soft configurations (Supplement Video 02). That is, an external, vertical push on the slider mechanism can be translated into an outward lateral push, snapping the laminates from soft to stiff configuration and vice versa.

It is worth noting that the examples above only demonstrate two possible implementations of switchable structures using bistable laminates. The simple and modular design can accommodate many combinations of laminate arrangement and actuation methods for stiffness switching (e.g., magnetic, pneumatic, or motors-driven tendons). Overall, the stiffness switching is energy efficient, requiring no constant power supply to maintain the switched stiffness. The results of this study can foster a new class of composite structures that can adapt their mechanical properties.

Finite Element simulation for compression buckling

The compression behavior of bistable composite laminates is modeled in ABAQUS CAE 2022 using the ‘Static General’ analysis setup with a displacement-controlled setting. The constitutive material properties of the uni-directional CFRP prepreg laminar and the TPU-based connection strip are summarised in Table 3.3. We model the laminate as a 3D-deformable shell structure with a partition for the connection strip set between the two layers of uni-directional prepregs (Figure 3.2 in the main text). We also model the end boundary plates that host the laminate in between, where the laminate has a fixed constraint at the center part of its top and bottom edges corresponding to the TPU strip. The rest of the laminate’s top and bottom edges in contact with the boundary plate are given the “tangential” contact properties according to the friction case as mentioned in Section 3.3.2, and the “normal” contact property if hard contact is considered. We find that a global mesh size of 2 mm and local seeding of 0.5 mm near the connection strip can achieve convergence, and the simulation results are consistent with the experiment.

The finite element simulation involves five steps: (1) Heating: We apply the curing temperature as the prescribed field and fixed boundary condition according to vacuum bagging on the entire laminate. (2) Cooling: The laminate cools to room temperature (20°C) with

Laminar Properties						TPU Properties	
E_1	140 GPa	G_{13}	5 GPa	α_{11}	2.4×10^{-5}	E	26 MPa
E_2	9.4 GPa	G_{23}	7.17 GPa	α_{22}	3×10^{-5}	ν	0.3
ν_{12}	0.3	G_{12}	3.97 GPa	α_{33}	3×10^{-5}	α	1.0×10^{-4}

Table 3.3: CFRP prepregs – Grafil TR50S Carbon fibers with Newport 301 resin system with a thickness of $h = 0.12$mm is modelled as laminar material. Tetra-PolyUrethane (TPU) strip with a thickness of $h = 0.5mm$ is modelled as elastic material.

the fixed boundary condition released, completing the curing process. (3) Snapping: The laminate is snapped to its first stable state via snapping displacement at the center node. (4) Settling: We add a free damping step by releasing the snapping displacement, allowing the laminate to settle and release any residual stress. (5) Loading: The laminate is compressed by 5mm at the connected parts of the top edge. We extract the reaction forces from the nodes at the top edge that are in contact with the upper-end plate and sum them up as the total reaction force. To determine the laminate's buckling modes, we use the first four steps as above and then apply the 'Static, Linear Perturbation' step analysis with the *buckle* option. For the perturbation, a line load of unit magnitude is applied so that the eigenvalue can be directly linked to the critical buckling load according to the equation 3.2.

The finite element simulation with the changing aspect ratio is set up similarly to the steps above. The only exception is the third step for snapping. Here, we adjust the magnitude of snapping displacement according to the laminate's geometry.

For the simulation with the additional lateral forces, we introduce three point-forces on the two vertical edges. These lateral forces are incorporated into the fifth step as explained above and are kept constant throughout the simulation, consistent with the experiments shown in Figure 3.6.

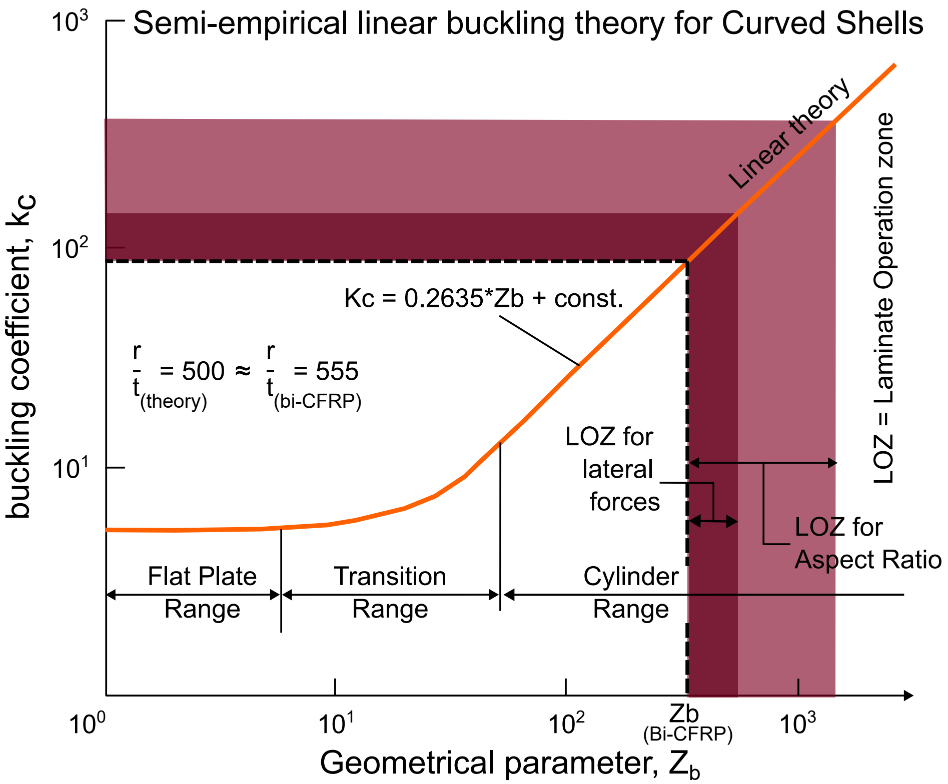

Figure 3.9: Semi-analytical buckling theory for curved shells: The correlation between the buckling coefficient k_c and geometric parameter Z_b is marked by the *orange* line. This curve is specific to $\frac{r}{t} = 500$ (curvature to thickness ratio).

Semi-empirical Theory

The laminate's critical buckling forces are estimated through the semi-analytical linear buckling theory for curved shells presented by Gerard et al. in the *NASA Handbook of Structural Stability: Buckling of Curved Shells and Plates* [91]. We find the theoretical predictions could be improved using the buckling coefficient k_c that varies as a function of geometrical parameter Z_b (refer to the equation 3.4.1).

Figure 3.9 is adapted from Figure 38(b) of the handbook mentioned above, where it lists different correlations between k_c and Z_b according to different $\frac{r}{t}$ values. For the laminates in this study, this ratio is close to 500 ($\approx$ 555). Hence, we plot the buckling coefficient k_c

as a function of the geometric parameter Z_b for our base laminate with [0°/90°] fiber layer and $100mm \times 100mm$ size. The result of this base laminate is later used for estimating the increase in the critical buckling forces of laminates by varying parameters.

For the first parametric study, we predict the critical buckling loads as a function of changing aspect ratio based on the scaling law in Eq. 3.5. The corresponding changes in its geometrical parameter are marked as LOZ (laminate operation zone) for aspect ratio in Figure 3.9. Similarly, for the second parametric study, we mark the change in the geometrical parameter due to additional lateral forces as LOZ for lateral forces.

3.6 Additional Information

Failure of the Composite Laminate under Compression at the Soft Configuration

The bistable laminates show a stiff response under compression in its stable state 1; however, once it undergoes the 3-step buckling, it settles into the stable state 2. In our tests, the compression loading is effectively quasi-static with a low deformation rate, and the buckling produces a snapping sound due to rapid energy release. Nonetheless, this buckling process does not develop any stresses large enough to damage the laminates. However, if the external force comes as a significant impact, the laminate would *sometimes* show an alternate buckling path that bends the laminate towards the opposite curvature of stable state 2 (Figure 3.10a). This alternative buckling generates excess tensile stress in the [0°] fiber ply (aka. fibers perpendicular to the force direction). As a result, the fiber laminate would eventually fracture along the middle line (Figure 3.10b).

Failure of bistable laminate is far less studied than traditional, monostable composites with

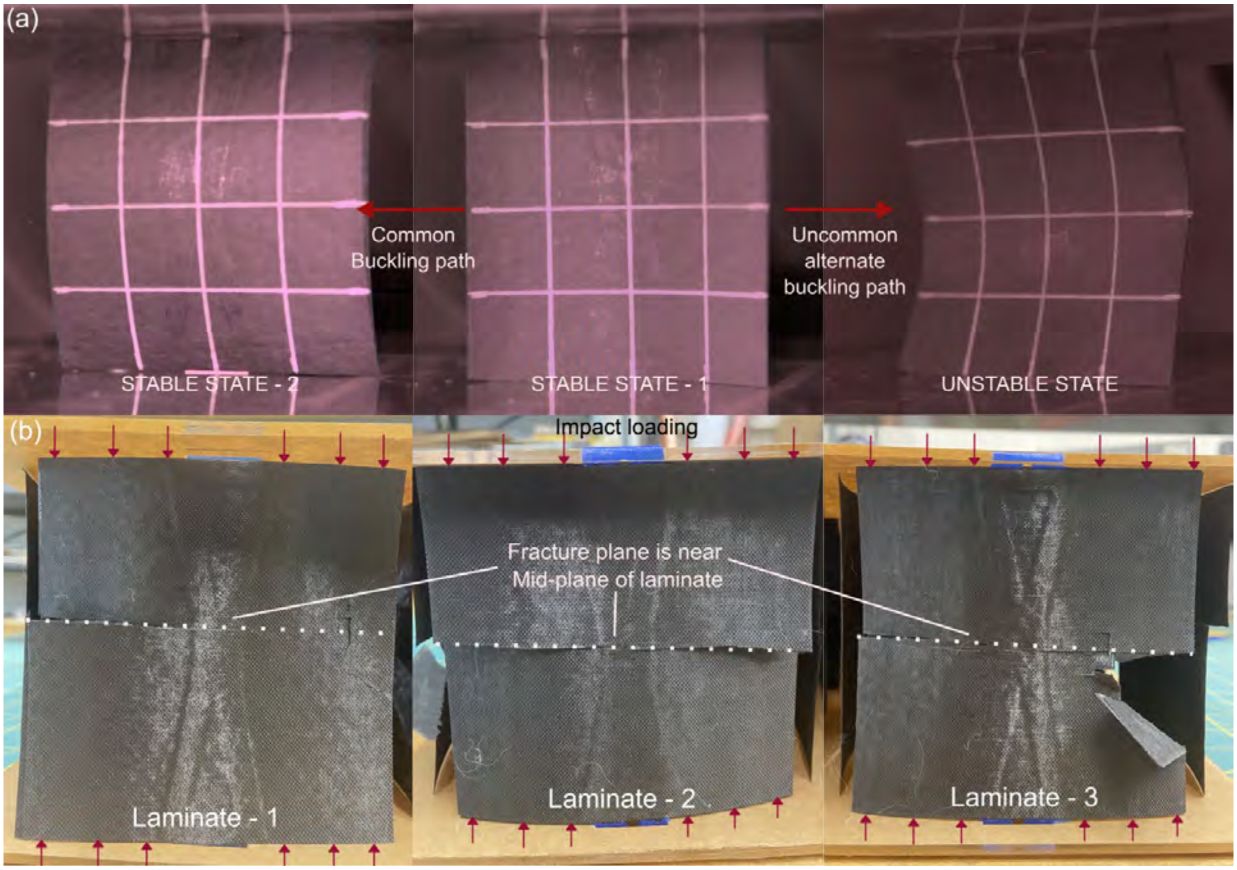

Figure 3.10: **Failure of bistable laminate**. (a) The two different buckling paths of a laminate starting from its stiff configuration. Usually, with a slow compression load, the laminate would undergo the 3-step buckling and switch to its second stable state. However, if the external force is an impact, there is a possibility that the laminate would buckle "in the opposite direction," leading to excessive stress and crack failure. (b) Images of three failed laminate samples due to the alternative buckling with large impact loads.

symmetric fiber layout. It is a potential research topic in the future. However, this study delves into understanding the buckling instability of bistable laminates and their responses to compression loadings in two different states. Hence, further examining the failure is out of the scope in this study.

Information for the stiffness tuning materials' performance in Figure 3.1:

1. **Nitinol – Shape Memory Alloy Wire (SMA) wire**:

   Test sample: Wire of 100 mil diameter with a gauge length of 6.65 in Phase transition temperature: 82°C (355 K) – 38°C (311 K)

   E_{hot} / $E_{\text{cold}} = 4$

   Density of Nitinol = 6.47 g/cc

   Max. Stress = 550 MPa

   Reference: Cross, W.B., Kariotis, A.H. and Stimler, F.J., 1969. Nitinol characterization study (No. GER-14188). NASA.

2. **Shape Memory Polymer: Polyurethane Series**

   Test sample: Rectangular sheet with $l = 25$ mm, $w = 5$ mm, and $t = 50$ μm

   Glass transition temperature: 55°C (328 K).

   E_{cold} / $E_{\text{hot}} = 100$

   Density = 1.25 g/cc

   Max. Stress = 28 MPa

   Reference: Tobushi, H., Hara, H., Yamada, E. and Hayashi, S., 1996. Thermomechanical properties in a thin film of shape memory polymer of polyurethane series. Smart Materials and Structures, 5(4), p.483.

3. **Elastomeric Composite (EMC)**:

   Test sample: Dog bone specimen with a cross-section of 0.25×0.125 $inch$

   Material: CTD-DP-5.1 resin

E_{cold} / $E_{\text{hot}} = 100$

Density $\leq 1.2\ g/cc.$

Max. Stress = 20 MPa

Reference: Abrahamson, E.R., Lake, M.S., Munshi, N.A. and Gall, K., 2003. Shape memory mechanics of an elastic memory composite resin. Journal of intelligent material systems and structures, 14(10), pp.623-632.

4. **Tachi-Miura Origami Polyhedron**:

   Test sample: Paper folded structure

   $K_{\text{fold}}/K_{\text{nofold}} = 25 \approx 27$

   Typical paper density = 375 g/m^2

   Paper thickness = 0.2 mm (assumed based on common print paper)

   Density = $\frac{375\times10^{-4}}{0.02}$ = 1.875 g/cc

   Max. Stress = 0.0067 MPa

   Reference: Miyazawa, Y., Yasuda, H., Kim, H., Lynch, J.H., Tsujikawa, K., Kunimine, T., Raney, J.R. and Yang, J., 2021. Heterogeneous origami-architected materials with variable stiffness. Communications Materials, 2(1), p.110.

5. **SMA-Based Continuum Manipulator**:

   We considered the SMA sheath that is tested for its bending stiffness, made with SMA wires of 0.5mm diameter.

   $K_{\text{volt}}/K_{\text{novolt}} = 1.4 \approx 2.2$

   Effective Density = $\frac{TotalMass}{TotalVolume} = \frac{8\rho_{SMA}\ .\ wirevol.}{L\ .\ Cross\ area} = 0.139\ g/cc$

   Assume the sheath is a hollow cylinder with an inner diameter d =16 mm and outer diameter $D = 14$ mm, the maximum Bending Stress = $\frac{y\ .\ M}{I}$ = 0.7211 MPa

Reference: Jiang, S., Chen, B., Qi, F., Cao, Y., Ju, F., Bai, D. and Wang, Y., 2020. A variable-stiffness continuum manipulators by an SMA-based sheath in minimally invasive surgery. The International Journal of Medical Robotics and Computer Assisted Surgery, 16(2), p.e2081.

6. **Electrostatic Layer Jamming Material**:

   Samples made by paper (80 gsm), carbon grease (1.05 g/cc), PI-film (1.42 g/cc), and Aluminum tips (2.7 g/cc), with a dimension $40 \times 120 \times 0.08\ mm$

   $K_{\text{jammed}}/K_{\text{unjammed}} = 6 \approx 7$

   Effective density $= \frac{TotalMass}{TotalVolume} = \frac{wt.of\ (paper+carbongrease+PI-films)}{Vol.\ of\ plate} = 1.226$ g/cc

   Max. Nominal Stress $= 0.93\ MPa$

   Reference - Wang, T., Zhang, J., Li, Y., Hong, J. and Wang, M.Y., 2019. Electrostatic layer jamming variable stiffness for soft robotics. IEEE/ASME Transactions on Mechatronics, 24(2), pp.424-433.

7. **Shape memory Polymer Composite (SMPC)**:

   $E_{\text{cold}}/E_{\text{hot}} = 79$

   Fiber volume fraction $\nu_{\text{fiber}} = 0.3$, where $\rho_{\text{resin}} = 0.9$ g/cc and $\rho_{\text{fiber}} = 1.76\ g/cc$

   Effective density $= \rho_{\text{resin}}\ \nu_{\text{resin}} + \rho_{\text{fiber}}\ \nu_{\text{fiber}} = 1.16\ g/cc$

   Max. nominal stress $= 35\ MPa$

   Reference: Chen, Y., Sun, J., Liu, Y. and Leng, J., 2012. Variable stiffness property study on shape memory polymer composite tube. Smart Materials and Structures, 21(9), p.094021.

8. **Fluidic flexible Matrix Composite ($\mathbf{F^2MC}$)**:

Sample made with carbon fibers ($_{\text{CF}} = 1.54\ g/cc$) and silicone matrix ($_{\text{Sil}} = 1.24\ g/cc$)with a fiber volume fraction $\nu_{\text{f}} = 0.5$

$E_{\text{closed}}/E_{\text{open}} = 25.1$

Effective density $\rho_{\text{Sil}}\ \nu_{\text{Sil}} + \rho_{\text{CF}}\ \nu_{\text{f}} = 1.39\ g/cc$

Max. Nominal stress = 1.8 MPa

Reference: Philen, M., Shan, Y., Wang, K.W., Bakis, C. and Rahn, C., 2007. Fluidic flexible matrix composites for the tailoring of variable stiffness adaptive structures. In 48th AIAA/ASME/ASCE/AHS/ASC Structures, Structural Dynamics, and Materials Conference (p. 1703).

9. **Multi-stable Carbon Fiber Reinforced Composite Panel**:

Sample made with CFRP prepregs with $= 1.57\ g/cc$

$K_{\text{straight}}/K_{\text{curved}} = 95$

Max. nominal stress = $\frac{Force}{C/S\ Area}$= 2.72 MPa

Reference: Arrieta, A.F., Kuder, I.K., Waeber, T. and Ermanni, P., 2014. Variable stiffness characteristics of embeddable multi-stable composites. Composites Science and Technology, 97, pp.12-18.

Chapter 4

Folding laminates

4.1 Introduction

Until now, we have seen how the bistable laminate has varied behavior under different boundary conditions, such as out-of-plane loading and in-plane loading. These observed behaviors can be functionally implemented in real-world applications such as morphing aerofoil sections[29, 71], ailerons[1], and sandwich cores as shown in the previous chapter. One of the important features of bistability for such laminates is their characteristic curvatures in each state. These curvatures are in opposite directions plus perpendicular to each other and are interchangeable. So, the question arises:

Can these bistable laminates with characteristic curvatures be used for added functionality?

Before answering this question, let's look at what advantages bistable laminates could give us if implemented as a morphing structure that shows *reconfiguration*. Reconfiguration is a rearrangement process of a structure through some external activation to adapt or modify its properties for different functions such as stiffness[8, 67], friction[32], shape[36], and optical properties[92, 93]. A qualitative analysis of different types of reconfiguration structures and their activation methods is presented in the figure 4.1. Through a general understanding, the energy expense of reconfiguration activation methods such as mechanical, thermal, magnetic, and electrical is estimated. Electrical activation, the most refined and highest form of energy,

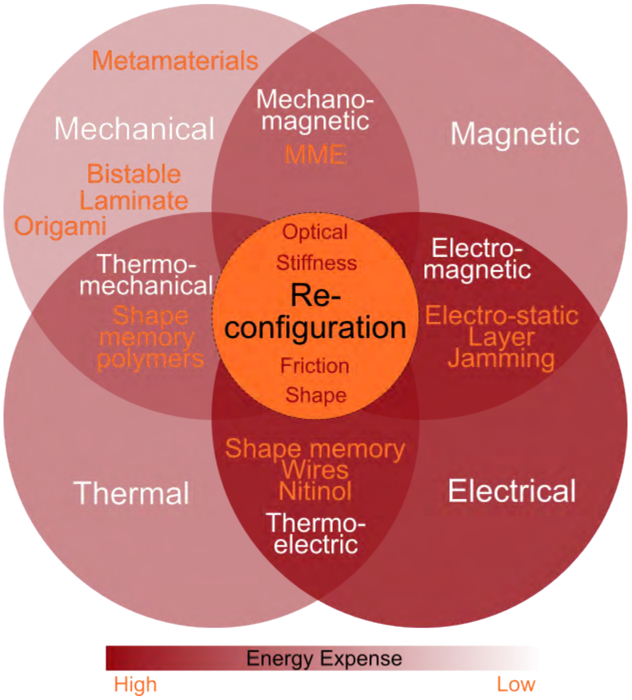

Figure 4.1: Qualitative Analysis for reconfiguration methods.

has the highest expense to operate. On the other side of the scale, mechanical activation is the least expensive form of energy available to use, such as simply applying force or pressure. The thermal and magnetic activation methods are deemed moderately energy expensive, more than the mechanical activation, but less expensive compared to electrical. Now, taking the example of Shape memory alloys (SMAs) such as Nitinol[58] that can be twisted to different shapes. To switch back to its original shape, it usually utilizes a combination of two modes, electrical energy by passing current as it is conductive, and once enough thermal energy is generated, it switches to its original shape. The energy expense and the equipment needs are quite intensive for such SMA wires. Another example of electrostatic layer jamming to adapt the stiffness of the overall structure[8] , which also utilizes two methods in combination. They use magnetic activation to attract adjacent layers and lock to create a thicker laminae structure, thereby increasing its bending stiffness. To create this magnetic activation, electrostatic forces are induced through energy-intensive electromagnetic devices. Hence, these reconfigurable structures serve different purposes, but one might question their efficiency in achieving this reconfiguration. We believe the answer to this could lie in combining two technologies that require only mechanical activation to achieve reconfiguration. One is, of course, our bistable laminates, and the other can be *Origami structures*.

Origami is briefly introduced in the introduction section. Here, we would reintroduce the concept of this ancient Japanese art form, which has shown tremendous potential and revolutionized modern engineering. Origami and Kirigami define the rules of folding paper in a specified pattern and order to create almost any shape. This technique has many advantages, though the most extraordinary feature is *scalability*. The mechanics of the folding patterns can be adopted easily from micron-to-kilometer scale structures.[94] This art form could have umpteen benefits in engineering, especially in fields such as metamaterials[31, 32, 33, 34, 85], morphing topologies (transforming from 2D shape to 3D shape)[35], and auxetic materials (negative Poisson's ratio or negative thermal expansion coefficients)[31, 36]. Most often, the folding principles at the basal level emerge from the nature of things around us. For example, the famous 'miura-ori' pattern is inspired by the geometry of leaves from beech or hornbeam trees, where its surface has a corrugated shape that is initially completely packed inside a bud. This bud opens up during the spring season by actuating the distributed flow vessels (veins) through the leaf body and opening the leaf geometry in the process. The Miura-ori has the auxetic property, i.e., the folded geometry opens and expands in both perpendicular directions even if stretched in one direction. One engineering field where this origami technique is being aggressively adopted is Space technology, where the storage and transportation of equipment inside a rocket is crucial. As the energy needs to operate the satellites are ever-increasing, there is a need to have larger solar arrays. The researchers have identified origami/kirigami-inspired structures as a possible solution to this big packaging problem, where large surface solar arrays could be *folded* into a much smaller volume and transported into outer space. Once there, it could be deployed to its original size. [95] Also, large booms are used in small satellites, CubeSats, for deploying these solar arrays [38, 39, 41] that need to be packed with them. Recently, in-space robotic equipment used in manufacturing/construction on extra-terrestrial planets is being redesigned using such techniques [96, 97]. To summarize, using a basis of origami, having the fold lines (creases) on a structure provides multiple advantages as follows:

1. Mechanical reconfiguration: as learnt above, the structure can change its shape/configuration from one to the other.
2. Packaging: the structure could be designed to fold into a smaller volume. It is useful in storage or during transportation.
3. Preventing failure: creases provide the purposeful less-stiffened areas to a structure, and through them, it might allow large deformation. This deformation might prevent the critical structural elements from crumbling under a load and developing fractures that eventually fail. To provide an example, consider figure 3.10 where the bistable laminate is shown to fail due to the compression forces. This failure could be avoided by having a fold along the failure plane.

From above, it is clear that Origami techniques could be successfully utilized to achieve reconfiguration. But this reconfiguration brings another drawback: it still needs to be actively held/secured in this reconfigured state. For example, if a fully-formed miura-ori sheet is compressed in the in-plane direction, it folds into a smaller volume. What if you want to lock the miura-ori in its initial configuration, such that it becomes load-bearing in that direction? Also, if you release this miura-ori sheet after compression, it does not stay in this completely-packed state. It bounces back like a spring to the original configuration due to the elastic forces induced at the creases. Hence, it needs to be constrained in this completely-packed state for packaging needs and is less efficient. This type of folding is often called rigid folding, where the panels (the plane between adjacent creases) do not deform and remain rigid during the process. However, if these panels are allowed to deform, there could be a way to lock these origami designs in different configurations and make some of them load-bearing.

Now, coming back to our question asked before, can these bistable laminates with their characteristic curvature help in this regard? Let's find out!

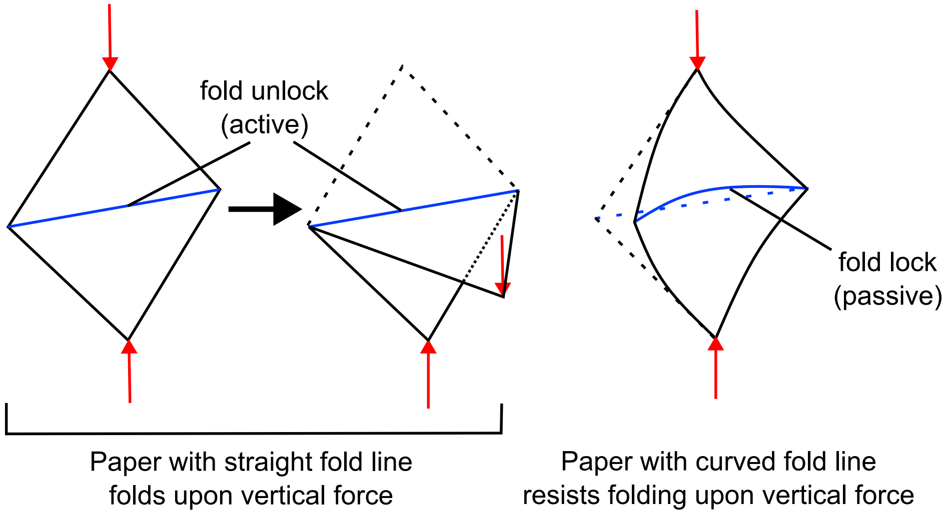

Figure 4.2: Paper with a Fold line. Under a compression force, perpendicular to the fold line, paper would bend along this horizontal crease. Whereas the compression characteristics improve significantly with a small curvature along the fold line.

To explain the idea, consider a simple demonstration, refer to the figure 4.2. Here, a piece of paper with a fold line along its diagonal is shown. Now, if one applies a vertical compression force at two opposite corners of the paper, perpendicular to the fold line, it folds with no resistance. Whereas, if you push the other two corner points inwards, a curvature develops in the paper and at the crease. This curvature significantly improves the resistance of the paper toward folding under the same vertical compression force. Hence, an increased compression load-bearing ability in the paper is observed. Therefore, introducing such a simple curvature to the crease can '*lock*' the ability of the structure to fold. And making the crease free from curvature can '*unlock*' the ability to fold. Here, bistable laminates could be employed effectively as their two stable states could be carefully designed to provide this locking and unlocking feature to the fold line (refer to the figure 4.3). The idea of introducing curvature to the panels (area between the creases) breaks the traditional assumption of having rigid fold-ability and gives rise to *compliant fold-ability*. This would allow the panel to smartly reconfigure by selecting "to be folded or not to be folded". Here, we continue learning from the previous study as the TPU and CFRPs show good bonding characteristics. TPU is used as a flexible material that behaves like fold lines on the laminate. The simplified fabrication of bistable CFRPs with the addition of TPU creases in its geometry could bring a paradigm shift in the morphing technology where structural reconfigurations could be locked and unlocked in an energy-efficient way.

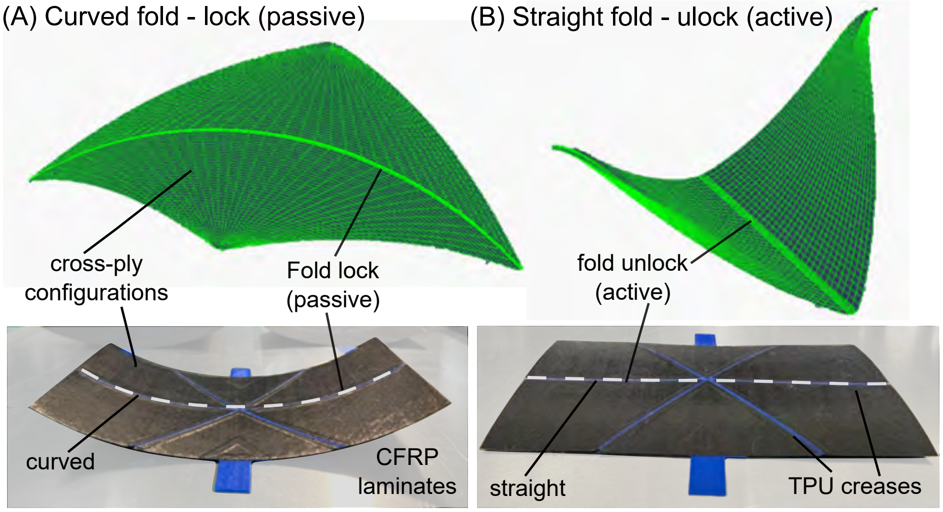

Figure 4.3: Embedding fold line into a bistable laminate. In the first stable state, the fold line is curved and locks the laminate from folding along it. Whereas the fold line is straight in the other stable state. This allows laminate to fold along it as shown in the simulated figure on the top.

To understand its impact, the following study will first select a panel structure inspired by one of the bases used in origami, with creases that can be folded into different configurations. Second, we explain the fabrication challenges and procedures for integrating CFRPs and TPU materials in detail. Third, the compression responses of this panel structure are studied for three different configurations that commonly occur in origami designs. At last, we look at some applications of using this panel structure.

4.2 Methodology

Here, we first understand the process of selecting an origami geometry of interest to be used with our laminates. Later, we discuss a new fabrication technique devised to manufacture such laminates.

4.2.1 Panel geometry: Waterbomb laminates

Origami engineering has seen a lot of potential applications in the last two decades to create meta-materials, sensors, and actuators for use in soft robotics, space technology, and bio-inspired structures. Hence, it is critical for us to explore any opportunities to utilize our novel bistable laminate technology in origami engineering, especially when we observe that they could be used to control structure reconfigurations. Various fold patterns that are regularly seen in origami engineering designs (refer to figure 4.4) are Yoshimura, Waterbomb, Ron-Resch, and Miura-Ori.

Upon carefully observing these patterns, a bow-tie-like crease pattern emerges that is often repeated (as shown in the red color in the figure) and is of great significance in our study. This intersecting crease pattern is one of the important *bases* in origami called as ‘Waterbomb base’, which helps build more intricate origami designs. We believe that by studying this

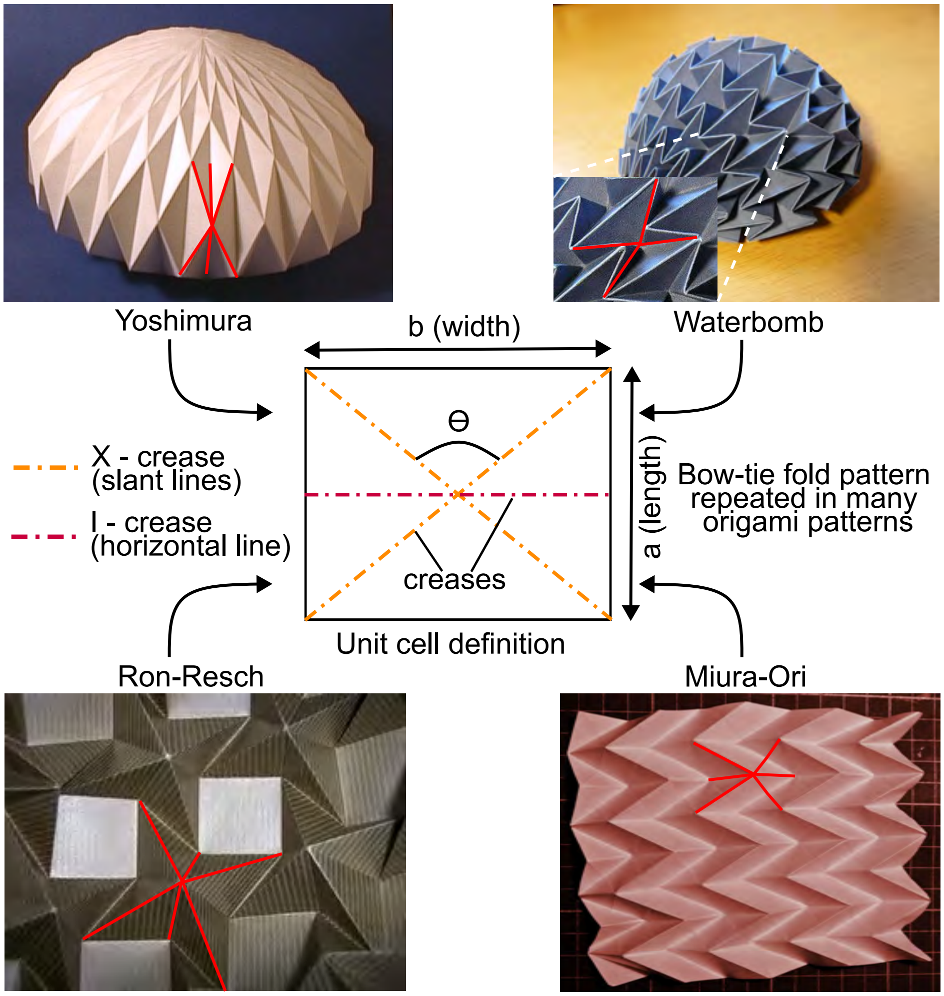

Figure 4.4: The geometry selection of the panel structure that has a bow-tie crease pattern, which is one of the important origami bases called a '*Waterbomb base*'. This geometry is observed repeatedly in many origami patterns such as Yoshimura, Waterbomb, Ron-resch, and Miura-Ori. This waterbomb crease pattern has a horizontal crease called an '*I-crease*' and a cross pattern called an '*X-crease*'.

pattern, one could get critical information in creating a wide variety of origami designs where reconfigurability is desired. This waterbomb base pattern has two types of creases - an '*I-crease*' that runs horizontally through the geometry marked by red color, and an '*X-crease*' that has two diagonal creases marked by orange color. We isolate this folding base pattern from the designs and study its geometry as applied to our bistable laminates. The peripheral geometry of the structure is kept as a rectangle with two sides marked as 'a' and 'b' in the figure, which is consistent with our previous studies. The idea is to understand how well the bistability of composites can be used to (a) lock the crease lines and not allow the structure to fold; (b) easily unlock the crease lines and fold with little stiffness to pack the structure with either just along the I-crease line or use all the creases including the X-creases.

The following study first outlines the in-house fabrication techniques and method for such unique bistable laminates that have crease lines inside the geometry. Second, to understand the various folding behaviors quantitatively, we present in-plane compression tests of laminates in different possible configurations observed. Also, a parametric experimental analysis is presented to observe the effects of increasing the size of the laminates (aspect ratio) and changing the X-crease angle of the laminate on the in-plane compression response for three different configurations. Later, we conclude by presenting our findings and possible future work to effectively use them for space technology where optimized packaging of large structures is ever necessary.

4.2.2 Fabrication Technique

The waterbomb laminate is developed through a newly designed fabrication technique. This technique is inspired by our previous study, in which we observed that TPU can be successfully combined with CFRP and has good bonding. The idea is to use the TPU material as the softer crease material and unsymmetric CFRP panels to impart bistability to waterbomb laminates. This fabrication process is more involved as many smaller geometries need to be aligned precisely. Refer to the figure 4.5 (a).

Firstly, the CFRP uni-directional prepregs are cut to the appropriate dimension of the waterbomb laminate in both [0°]-ply and [90°]-ply. Next, the crease pattern is marked on them and cut into smaller triangular pieces, as shown in the figure. Note, during manual fabrication, it is important to follow the above step as cutting the prepreg sheets directly in the triangular pieces incurred many fabrication inaccuracies. Simultaneously, the appropriate crease pattern is 3D-printed using the Ultimaker S5 printer with TPU material. The TPU crease pattern is specifically custom designed to have extended thin flaps (5 mm wide) on both sides of the crease line (crease width = 1 mm). Next, lay the triangular pieces of [0°] ply on the bottom layer and carefully place the TPU crease on top so that the prepregs overlap only on the thin flaps and not on the crease lines. Now, place the TPU flexible connection inserts in the center of the two opposite larger sides, as shown. Later, the triangular pieces of [90°]-ply are placed on top and pressed firmly to ensure the two layers of prepregs stick to each other. Lastly, the vacuum bagging technique is employed again to cure these laminates at standard 145°C for three hours. After curing the laminates and then releasing them upon cooling to room temperature, it is observed that they settle in either configuration 1 or configuration 2. All the different waterbomb laminates are tested in these two configurations, as well as configuration 3, which resembles the actual folding of the waterbomb structure.

4.3 Results

The waterbomb base patterned bistable CFRP laminate shown above in the figure 4.5 (b) has three different configurations that are interchangeable upon applying appropriate boundary

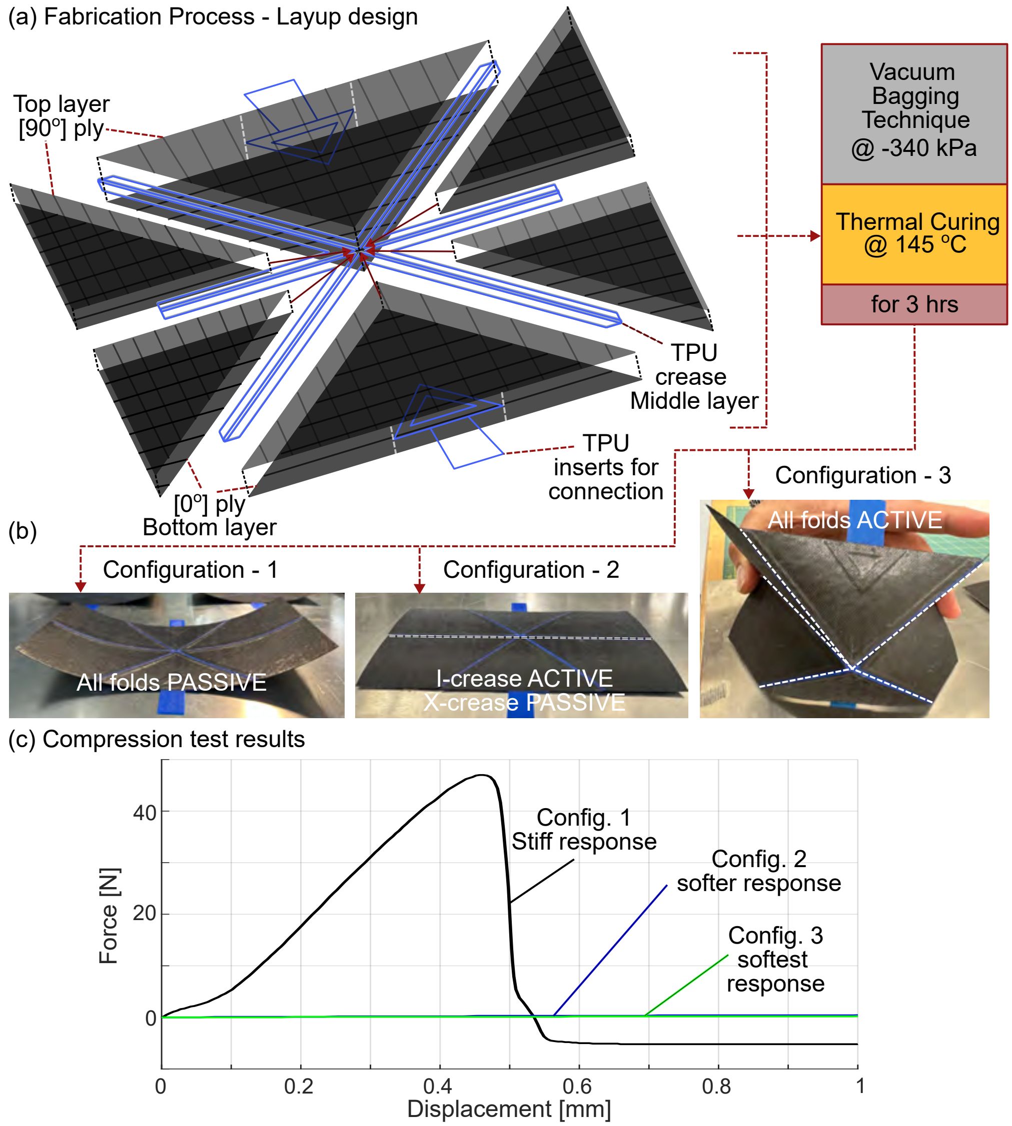

Figure 4.5: Fabrication process for folding laminates. (a) Appropriate triangular-shaped prepreg pieces are cut of — [0°]-ply that are placed on the bottom layer; and [90°]-ply that are placed on the top layer. A 3D-printed TPU crease is carefully sandwiched between these two layers such that it overlaps with prepregs only at the outer thin flaps. Once all the prepreg cut-pieces are assembled, the entire laminate geometry undergoes familiar vacuum bagging technique and is cured in the composite oven. (b) After the curing process, the waterbomb laminate is observed to reconfigure in three different modes — configuration 1: all folds are *passive* and locked; configuration 2: only the I-crease is active and folds; or configuration 3: all the folds are actively folding. (c) Upon compression testing of all the configurations for a square laminate, i.e. AR = 1, it is revealed that configuration 1 produces the stiffest response, whereas configuration 3 produces the softest response.

conditions. In the current study, we deem understanding the load-bearing performance of laminate in these different configurations is a critical aspect more than the reconfiguration process itself. Introducing these fold lines, the laminate is expected to weaken in compression performance.

We primarily test the crease locking ability of the bistable laminate by performing load-bearing in-plane compression testing. The square laminate (aspect ratio = 1, 100×100 mm^2) is tested in all the three configurations whose results are summarized in the figure 4.5 (c). It is observed that in configuration 1, where all the fold lines are locked due to the curvature, produces a high-stiff response. Whereas, in configurations 2 and 3, the fold lines are active and produce extra-soft responses compared to the compliant response seen in Chapter 2. The creases in this waterbomb laminate, when active, can be potentially used to fold the laminate in different configurations with ease and could be employed in origami/kirigami-inspired structures effectively. Also to get a better understanding, a parametric analysis is presented where the change in load-bearing abilities of the laminate is observed with (a) changing the aspect ratio of the laminate to observe how the curvature at the I-crease influences the response, and (b) changing the subtended angle (θ) between the X-crease lines to observe the interplay of the central triangular regions with the load-bearing capacity of laminate. Hence, the test setup for the in-plane compression consists of — a fixture that is mounted on the force sensor and connects at the top-center of the waterbomb laminate to apply concentrated loading in the central region; another fixture that holds the bottom part of the laminate and restricts all the degrees of freedom; and an appropriate load cell (Instron 1kN load cell) with a displacement rate of 0.5 mm/sec. This setup is consistent in all the different tests presented below.

4.3.1 Aspect Ratio Study

In the first parametric analysis, we study the effect of changing the aspect ratio of the laminate, i.e., by increasing the size of the laminate from a square shape to a rectangular shape for wider laminates. With this increase in the laminates span (horizontal direction), the curvature, as seen in the previous chapter, also increases. However, due to the presence of crease lines in the geometry, it is also observed that the curvature of the laminate decreases when compared to not having any crease lines. This curvature change effects are currently beyond the scope of the work as we need to outline the advantages of having an ability to fold for such laminates.

For experiments, five different aspect ratios are selected for waterbomb laminates ranging from AR = 1 to 2. The subtended angle θ between the X-crease is kept constant 90° for all laminates. These are tested for in-plane compression at their three different configurations as seen in the figure 4.6. In configuration 1, all the folds are locked, and two important observations are recorded — max. critical load before it buckles completely to change shape to configuration 2, and the stiffness in the initial period of compression test. A counter-intuitive results are seen where it is observed that the AR = 1 laminate shows the highest critical buckling load of 46 N (approx.), which is much lesser than a similar laminate with no fold lines (reference from the previous chapter, section 3.3.1), i.e., 90 N (approx.). The inference is that having creases inside the laminate weakens it in the compression test by almost 50% with this crease pattern. However, we acknowledge that the boundary conditions used in these tests are partial and do not use the complete top and bottom edges as with the tests done in Chapter 2. With increasing aspect ratio, we see a decreased load-bearing ability of the laminates for this set of boundary conditions. The author believes that as the compression forces are concentrated through the central region of the laminate, the two bigger triangular regions in the laminate at the connections are the main load-bearing

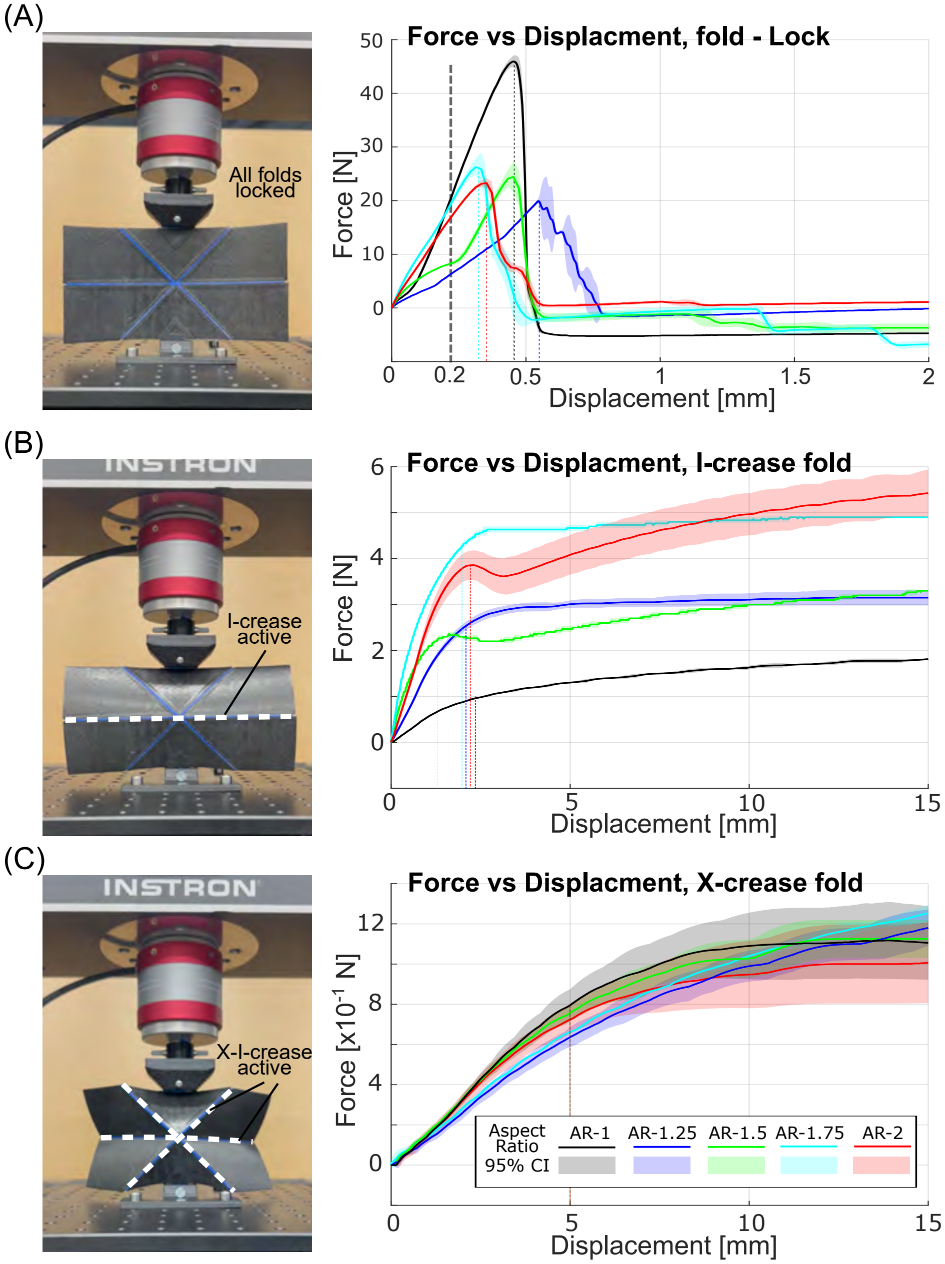

Figure 4.6: Effect of change in aspect ratio (AR) to in-plane compression response of three different configurations of the creased folding laminate. (A) The experimental image shows the laminate has all creases locked, which has a stiff compression response as seen in the following force vs displacement plot. (B) The experimental image shows the laminates in a foldable state where only the horizontal 'I-crease' is active. The following plot shows a much softer response compared to the first configurations. (C) The experimental image shows the laminate in the other possible foldable state where both the 'X-crease and I-crease' are actively deforming and producing the softest response of all the configurations.

Aspect ratio	Fold lock Max. load [N]	Fold lock stiffness** [N/mm]	I-crease fold stiffness** [N/mm]	X-crease fold stiffness** [N/mm]
AR = 1.00	45.89 ± 1.09	109.85	0.54	0.16
AR = 1.25	21.93 ± 2.53	77.95	1.29	0.15
AR = 1.50	24.89 ± 2.41	87.74	1.75	0.14
AR = 1.75	26.83 ± 2.16	82.77	2.69	0.13
AR= 2.00	23.35 ± 0.85	56.14	3.04	0.13

Table 4.1: The aspect ratio changes the compression characteristics of waterbomb laminates.
** Avg. stiffness is measured over five tests for each sample.

parts. And they are identical ($\theta = 90°$) for all different designs as the aspect ratio increases. For higher aspect ratios, the other regions of the laminate (except for these two central triangular regions) get isolated due to the creases. Learning from the previous chapter 3, the deformation at the top and bottom edges of the laminate during the buckling process is crucial and more the curvature at these edges, the more buckling force is observed. Now, having the X-crease meet on these edges results in a partitioning of the curvature. This curvature for the middle triangular regions remains fairly similar for all the aspect ratios. Hence, all the waterbomb laminates, except for the AR = 1, show very similar buckling forces. For the AR = 1 laminate, the middle triangular region has a continuous curvature at the top and bottom edges, and the X-crease meets only at the corner. This helps transfer the load to the other regions of the laminate and is able to sustain higher buckling loads before it snaps to configuration 2.

In configuration 2, the laminate has the X-creases still in the passive state, i.e., they are locked, whereas the I-crease becomes active. Hence, upon compression, the waterbomb laminates fold in half along its horizontal crease. This behavior is consistent for all the laminates with increasing aspect ratio. The force-displacement results are presented in the figure 4.6(B), showing how the initial linear stiffness (slope of the initial curve until the behavior is linear) of the laminates is observed to increase with increased aspect ratio. These results are summarized in the table 4.1.

Configuration 3 is commonly observed in the origami structures and is called the waterbomb-base (refer to the section 4.2.1 for more details) fold, and hence, we decided to understand the response characteristics in this state as well. In this configuration, the structure can be completely flat folded by utilizing all the creases, i.e. X-creases and I-crease, similar to observed in different origami designs. Interestingly, the laminates do not stabilize in this state and have to be forced. Hence, we observe that all the waterbomb laminates of different aspect ratios need to be given a 20 mm preload to stabilize in that configuration. The results for the compression of laminates in this configuration are shown in the figure 4.6 (C). We observe a peculiar trend where the stiffness of folding remains fairly constant and does not change for wider laminates. The other important observation is that the stiffness showcased in this configuration is at least 5 times less than in configuration 2. This can be accounted for with the observation that the laminate has a greater degree of freedom to deform where all the triangular regions rotate with respect to their adjacent regions. Takeaways from this aspect ratio study are that, similar to chapter 3 , the laminates are affected by the aspect ratio, but here, the performance is observed to decrease in terms of load-bearing abilities.

4.3.2 Characteristic Angle: X-crease subtended angle θ

In the next parametric analysis, we change the subtended angle θ between the X-creases and observe its effect on the compression folding characteristics of the waterbomb laminates. For the study, we choose AR = 1.25 laminate and keep the boundary conditions the same as the previous analysis. Here, we only focus on two configurations—1 and 3—as their compression characteristics were susceptible to angle change.

The compression response for configuration 1 of waterbomb laminates with angle variations

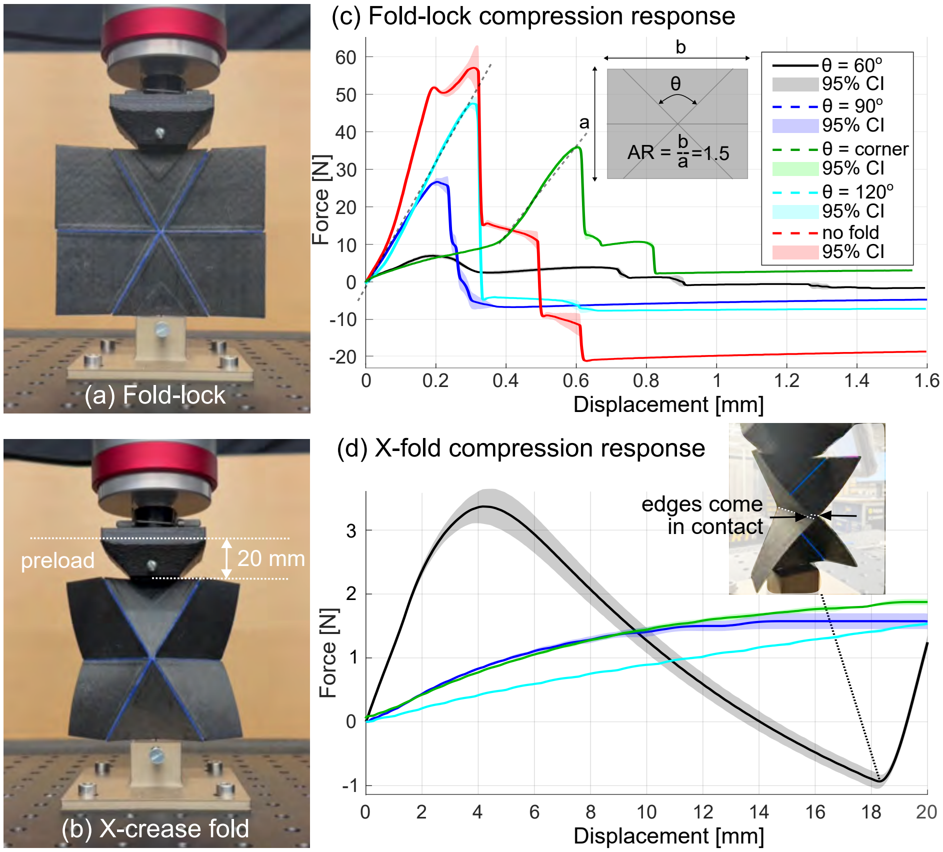

Figure 4.7: Various folding responses for AR = 1.25 laminates with varying X-crease subtended angle (θ). (a) All creases are in the locked state produces a stiff response. (b) All creases are active and fold the laminate until the two horizontal creases come in contact. It is observed that for the angle, $\theta = 60^\circ$ the horizontal creases come in contact on the back side of the laminate's face seen in the image. Therefore, a stiff response is observed once this occurs.

Subtended Angle (θ)	Fold lock Max. load [N]	Fold lock stiffness** [N/mm]	X-I-crease stiffness** [N/mm]
$\theta = 60°$	6.97 ± 1.42	35.92	1.17
$\theta = 90°$	26.92 ± 1.25	77.95	0.21
$\theta = corner$	36.77 ± 0.47	90.87	0.19
$\theta = 120°$	56.79 ± 1.63	163.39	0.11
$no\ fold$	74.19 ± 4.43	300.31	-

Table 4.2: Subtended Angle (θ) changes the compression characteristic of waterbomb laminate with aspect ratio = 1.25.
** Avg. stiffness is measured over five tests for each sample.

reveals an increasing trend for load-bearing capacities for the laminates. For example, laminates with angle $\theta = 60°$ have only 6.97 N (avg.) of critical buckling loads, whereas $\theta = 120°$ it shows the highest load-bearing with 56.79 N (avg.). The compression response of a laminate with no creases in its geometry is tested for comparison. Remarkably, we observe that for $\theta = 120°$ laminate, almost 76% of all the load-bearing capacity is maintained even after introducing fold lines.

For the compression in configuration 3, the stiffness remains fairly constant for all the laminates except for $\theta = 60°$this waterbomb laminate, where the middle triangular regions are quite small in comparison to other regions. Hence, the curvature in those other regions dominates the performance of the laminate, and we observe a much stiffer response from this laminate. Another important observation is with the flat-folding of laminates in this parametric analysis. The laminate with angle $\theta = 60°$ does NOT go through flat-folding. In fact, its two horizontal ends meet with each other mid-way of folding and provide much stiffer response. This could be observed in the force-displacement plot, refer to the figure 4.7 (d), where once the two ends meet, the response is seen to be stiff, indicating the fold-locking of the laminate. Hence, to ensure flat-folding of waterbomb laminates, it is crucial to keep the subtended angle $\theta \geq 90°$.

Following, we provide a case study that further explores this idea of incorporating bistable laminates in origami structures.

4.4 Case study: Plant-inspired Growing Robotic Structure

Publication Details

1. **Title:** "Switchable structures using asymmetric fiber composite laminates: two case studies"
   Conference: Active and Passive Smart Structures and Integrated Systems XVI (2022).
   Other Authors: Oliver Myers, Suyi Li.
2. **Title:**'Golden Ratio Yoshimura'for meta-stable and massively reconfigurable deployment
   Journal: The Royal Society - Philosophical Transactions A (2024).
   Other Authors: Ziyang Zhou, Yogesh Phalak, Ian Walker, Suyi Li.

4.4.1 Inspiration and Introduction

Maneuvering through congested and dynamically evolving environments is a long-standing challenge for the robotic community due to the rigid structure of the robots. The operation of such robots that interact with their environments often comes with safety guidelines due to the harm they can cause to humans through their life cycle. For example, the automated rigid arms used in industrial factories are very useful in carrying heavy loads and performing quite precise tasks, but their paths are fixed. Sometimes, humans may hinder these paths, risking their lives. Hence, it is a crucial advancement for robots to have the ability to change their progression path in multiple time scales (short and long time scales) and monitor their surroundings in real time to navigate through dynamic environments. Interestingly, nature has already found answers to such questions where plants (a) manipulate their growth directed towards sunlight for harnessing the energy through photosynthesis, (b) create a balanced path that can carry weight and make slow reinforcements (long time scale) at the branches according to the stress induced in them, and (c) sometimes achieve ballistic speeds (short time scale) in reacting to the surroundings such as Venus flytraps, touch-me-not plants.

The novel idea is to get inspiration from the plant world and design robotic structures that can achieve tasks in multiple time scales. A very exciting *Plant-inspired* project is ongoing in our lab (Dr. Suyi Li's lab) in collaboration with Clemson University. My research study is the first major step in this project with the aim to achieve slow and permanent growth of its 'trunk' (similar to a cylindrical structure) that can be maneuvered in changing directions to navigate through unfamiliar environments and maintain its stability and balance with load-bearing capabilities. To create such a conforming structure, we draw inspiration from the Origami (briefly explained in the section **??**) art form that has shown morphing capabilities. Specifically, we look at the compression buckling in cylinders that results in peculiar surface textures through elastic instabilities of the geometry. These surface textures arise due to controlled-localized buckling of the shell structure and are a function of the boundary conditions applied to it. Therefore, we discuss two such surface textures in the next section, which are famous origami designs, and show how we could achieve a 'trunk' structure using these two designs by coupling them with bistable CFRP laminates. The overall aim is to create a permanently deployable robotic structure that has locking properties to become load-bearing, the ability to unlock at localized locations to achieve growth in certain directions, and maintain stability and balance by optimizing the growth path.

4.4.2 Methodology

This research project is currently progressing through three main phases: (a) Design Selection, (b) Fabrication techniques and requirements, and (c) Experimental Testing (Ongoing).

Design Selection

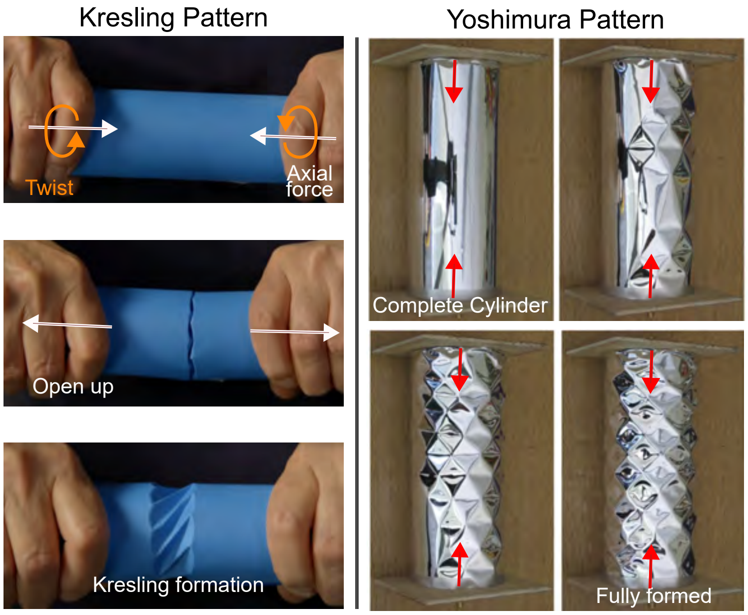

Figure 4.8: Surface texturing through cylinder buckling. (A) Kresling pattern emerges if you apply an axial compression force with a twisting moment. The figures show a sequential process of obtaining the pattern using chart paper wrapped around two cylinders and then carefully applying axial compression and twisting forces and moments [98]. (B) Yoshimura Pattern observed on a cylinder made from a mylar sheet. [99]

The key factors that would form an ideal robotic plant growth structure are (a) a simple folding and unfolding structure with minimum requirements to unfold; (b) after unfolding the structure it should lock itself in the configuration and become high-load bearing; (c) able to manipulate the growth direction; (d) a hollow structure from inside that can host a vine-like continuum robot (this part is studied by the collaborators in Clemson University, Dr. Ian Walker's Lab).

We studied two designs for our structure: (a) **Kresling Pattern** , observed in the buckling failure of cylinders under twist-axial compression loads, and (b) **Yoshimura Pattern** , observed in the buckling failure of cylinders under axial-compression loads. The figure 4.8 shows these two patterns developing on the surface of a cylindrical shell that undergoes elastic instability due to compression buckling forces. Therefore, a completely uniform shell, initially a high load-bearing structure, deforms under appropriate conditions to a folded configuration. Due to high concentrations of stresses developed at the crease lines, they usually exceed the material fracture limit and eventually develop cracks. We aim to *reverse* the phenomenon and achieve a completely locked shell structure from an initially folded configuration. Hence, the material selection becomes critical as there is a need to have (a) a compliant material at the creases of the structure providing a flexible coupling that can undergo large deformations and with minimum energy requirements and, (b) a stiff material at the intermediate panels that could resist deformation and impart load-bearing properties. This leads to the next section, which explains the fabrication of such structures that have special requirements.

Fabrication technique

The fabrication of folding structures is one of the big challenges that involve creases that undergo large deformation. If the crease line is well defined and has a *sharp* edge then the stress concentrations are quite high and often the material exceeds its yield limit, hence a plastic deformation is observed. For example, a folded model with paper or some plastic sheets forms sharp fold lines and is irreversible to a flat configuration with no trace of the fold line. General practice to maintain the operation of the folded state is to *temper* (soaking in an oven) the model (usually for models prepared from plastics) at elevated temperatures to release residual stresses that are developed at these fold lines. The other possible crease line would be to have a more continuous *blunt* fold line that has a curvature. For a blunt fold line, it is possible to have a stretchy material like rubber or soft polymers that can be recovered almost completely to the flat configuration. Learning from the previous chapter, in the section 3.2, we used the 3D-printed TPU material for a flexible connection, and it shows good bonding abilities with the CFRP laminates. Hence, we continue using this 3D-printing material to model our creases in the structure. TPU is a flexible polymer that has good chemical, corrosion, and high wear-tear resistances, which make it a good choice for our foldable structures that are going to be exposed to the outside world. The later challenge would be to make it water-resistant as it tends to absorb moisture over time.

Kresling Pattern

The Kresling structure consists of three main components: (1) a Kresling skin made of 3D-printed soft TPU material, (2) end plates made from stiff Nylon material (also 3D printed), and (3) triangular-shaped asymmetric laminates made from the above-mentioned CFRP prepreg. The Kresling skin (Figure 4.9(C)) serves as the skeleton of this structure. Its flexibility allows it to fold and unfold easily, generating the creases in the traditional Kresling origami design. These skins have triangular cavities in their facets to accommodate the asymmetric laminates, as well as five holes on the top and bottom to connect to the end plates. In this case study, we select L = R = 60 mm as the side length of the regular hexagonal base, the angle $\theta = 60°$, and angle fraction $\lambda = 0.8$ (Figure 4.9 (A)). Each end plate is an assembly of two components: the outer plate and inner plate (Figure 4.9(D)); the inner plate has teeth on its periphery that slide into the holes on the outer plate, locking the relative motion between the two. Finally, asymmetric two-ply laminates are added to the triangular-shaped cavities in the Kresling skin.

These laminates all have one fiber ply layer aligned in the crease direction and the other

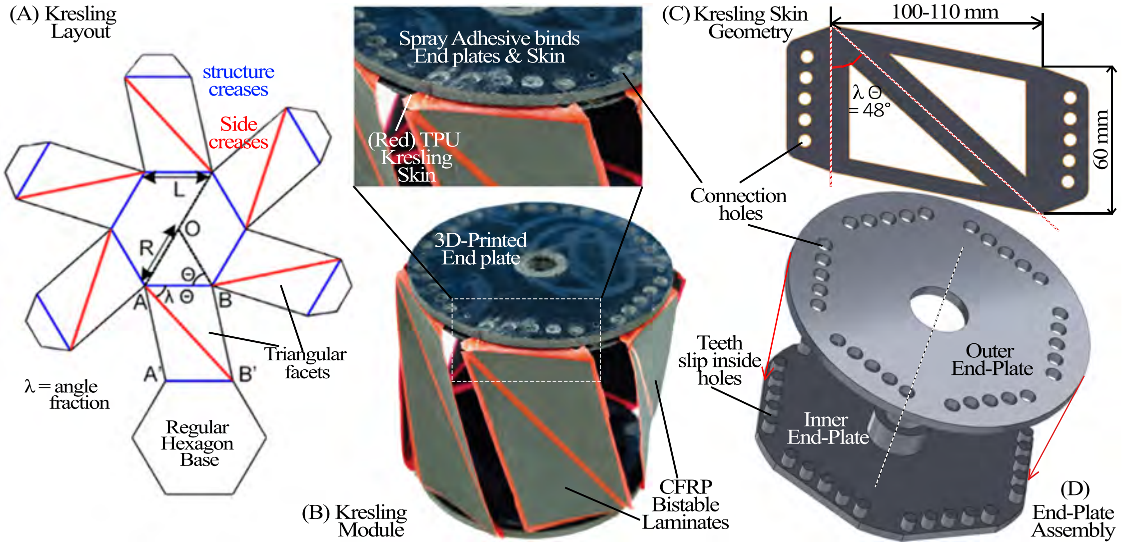

Figure 4.9: Switchable composite Kresling structure: Design parameters and fabrication process.

in the corresponding perpendicular direction. To fabricate the Kresling origami, we first assemble its facets by attaching uncured laminate prepregs to the 3D printed kresling skin, then oven-cure the facet assembly using the same vacuum bagging techniques. The cured Kresling facets are installed via the holes on the skin, in between the two components of the endplates (refer Figure 4.9(B), where the enlarged image shows the end plate assembly and the TPU skin installed in between the plates). We ensure that the Kresling facets are buckled outward in this assembly process. Finally, the two parts of the endplates are glued together with spray adhesive.

Yoshimura Pattern

Currently, the research model is in the trial phase of experiments. Hence, we fabricate the model in two ways: (a) a fully 3D-printed model with TPU material at the folding creases and Nylon material at the stiff panels, and (b) a model with integrated bistable CFRP laminates at the stiff panels and 3D-printed TPU creases. The idea for making two models is simply

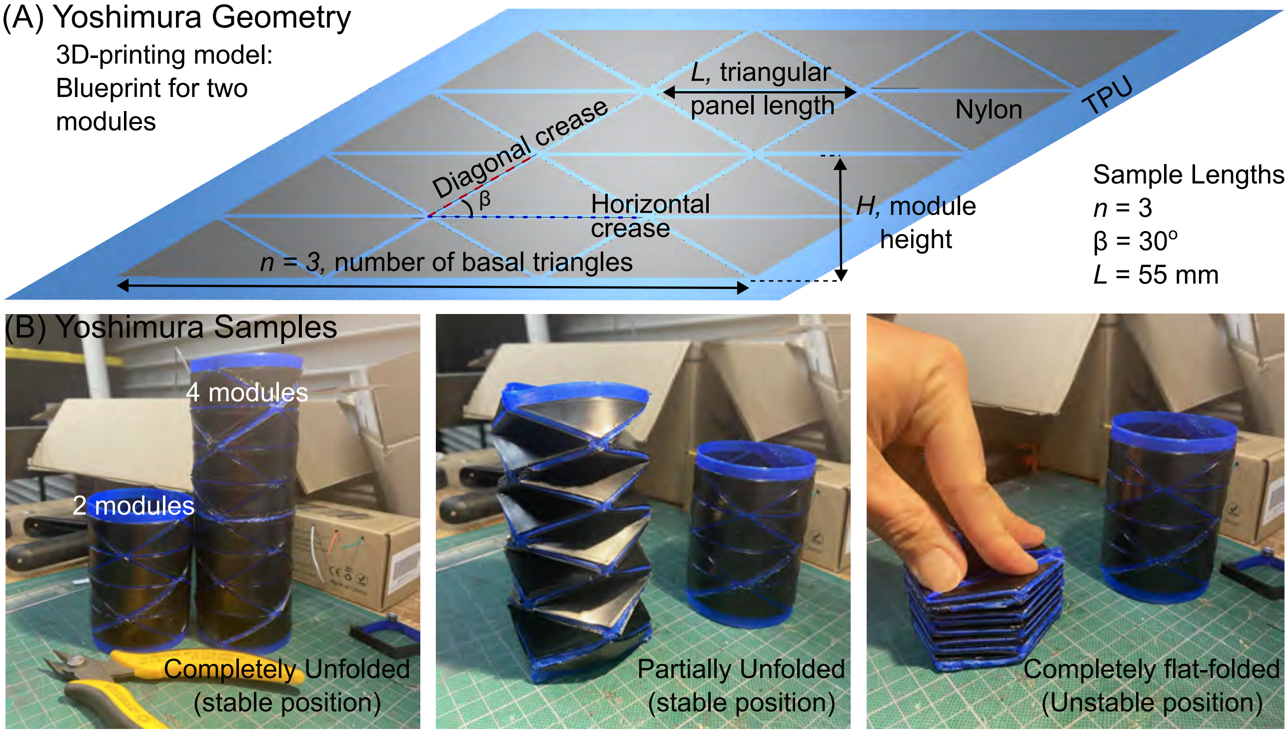

Figure 4.10: Yoshimura Pattern: (a) Yoshimura geometry has different parameters that are marked. Only two independent parameters are sufficient to define the geometry of the pattern, namely, $n = 3$ and $L = 55$ mm, which are used for the 3D-printed model. Note: The Blueprint shown here represents a model with two Yoshimura modules printed in a single run. (B) Yoshimura samples are 3D-printed with two materials - TPU (blue material) and Nylon (black material). Two samples are shown - one with two modules and the other with four modules. The subsequent figures show partial unfolded and completely folded states.

because of the material cost and efforts associated with the later model. Hence, during the experimental iterations of the model, the first method to have a complete 3D-printed model is preferred as it takes less time to fabricate and update the model.

The fabrication related to a complete 3D-printed model has various parameters that are currently being explored (refer to the figure 4.10). The parameters include (a) thickness of the TPU material (flexible coupling), (b) thickness of the Nylon panels (triangular facets), (c) L, length of the bigger side of the triangular facet, and (d) n, number of basal triangles. The geometry of a yoshimura pattern for no elastic deformation at the closed configuration, different parameters are linked together by the following expressions,

$$\beta = 90^\circ - \frac{(n-1)180^\circ}{2n} ==> 2n\beta = \pi \tag{4.1}$$

where the β refers to the angle subtended by the crease lines with the horizontal plane. The number of basal triangles n and the length of the side of a basal triangle L also relate to the diameter of the cylinder formed through a yoshimura pattern, which is given as follows,

$$nL = 2\pi R \tag{4.2}$$

We can also estimate the height of one module H using a simple equation as,

$$H = Ltan\beta \tag{4.3}$$

From the above relations, it is clear that only two independent quantities are required to define the geometry of the Yoshimura pattern. The sample size is kept small with $L = 55$ mm, $n = 3$. The idea of choosing $n = 3$ is the three basal triangles create a triangular ring through their bigger sides on every horizontal plane of the yoshimura pattern. This ring with three sides is the most stable structure; if there were two sides, then they would be against each other and generate too much constraint for the structure to deform; if there were four, then they would represent a four-bar chain and be susceptible to lateral deformation.

4.4.3 Significant Results

Kresling Structure

Once assembled, the Kresling structure is evaluated for its switchable behavior between foldable and locked configurations. More specifically, the assembled Kresling can stabilize itself in either a foldable State-1 or locked State-2 as shown in Figure 4.11(B). At the foldable State-1, the Kresling's side facets curve inwards, and its creases carry most of the external load. As a result, we can apply only a small axial force to fold the Kresling into a collapsed configuration, where all creases are folded to their maximum. We refer to this collapsed configuration as State-0 in Figure 4.11(B). Such folding (and twisting) from State-1 to 0 is consistent with the kinematics of traditional Kresling origami design. Once the external force is released, the Kresling quickly unfolds itself and returns to State-1.

To measure the compression force-displacement relationship of the Kresling at foldable configuration, we use the Universal Testing machine. A custom-made, free-rotating platform is installed on the tester machine to accommodate the Kresling's twisting during folding. The green-colored loading cycle shown in Figure 4.11(A) shows the response in foldable configuration between State-1 and 0. The State-1 is at the leftmost point of this cycle (∼ -50mm displacement), and the State-0 is at the rightmost (50mm displacement). Therefore, the total stroke of the foldable Kresling is near 100mm. More importantly, besides a slight increase in reaction force near the State-0 (the slight increase in stiffness could be attributed to the folded Kresling sides coming in contact at the end profile of the test and providing a small compression resistance), the foldable Kresling shows minimal resistance to external load.

In contrast to foldable State-1, the Kresling structure shows fundamentally different kinematic behaviors in the locked State-2. In this locked configuration, the side facets curve outwards, so the Kresling will not fold and collapse under a compression load. Instead, the facets bend outwards so that the stiff composite laminates, rather than the soft crease materials, carry most of the external load (Figure 4.11(B)). We can switch the Kresling from foldable State-1 to locked State-2 by simply twisting its end plates in the opposite direction to the folding-induced twisting direction. However, the reverse twist would not switch the locked Kresling back to its foldable State-1. This unique locked configuration and the corresponding switching behavior originate from the internal stress embedded in the asymmetric composite laminate facets.

Moreover, the locked Kresling offers significantly higher loading bearing capacity upon compression. The blue loading cycle in Figure 4.11(A) shows the response at the locked configuration. The Kresling supports almost 60 times its own weight ($\approx$ 200 grams) during the compression test, with only 40mm displacement.

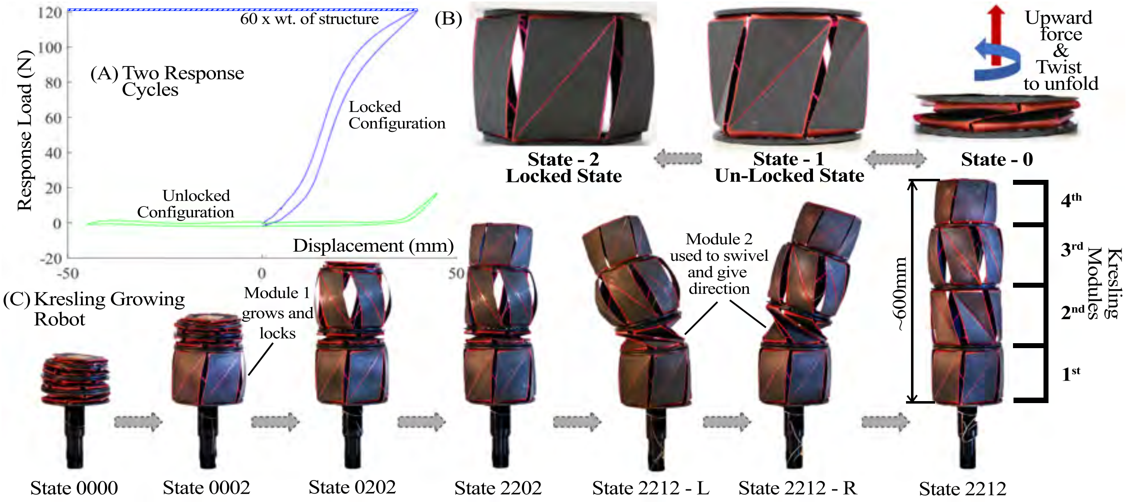

Figure 4.11: Switching behavior and potential applications of the composite Kresling origami. (A) Experimentally measured force-displacement curves of the Kresling in foldable (green) and locked (blue) configurations. (B) The Kresling origami at three different states – State-0 fully collapsed state, State-1 expanded but yet foldable where the kresling sides are still buckled inwards, and State-2 showing fully locked module that resists to fold. (C) A conceptual demonstration of the Kresling-based growing robotic trunk.

A promising application of the switchable Kresling structure is a “Kresling-based growing robot.” The idea is to assemble various Kresling modules into a robotic trunk and mimic plant-like growth behavior by exploiting their (un)folding and locking behaviors. Figure 4.11(C) demonstrates a preliminary example of such a growing robot, where four Kresling modules are axially connected. We label the configurations of this robot using a simple naming scheme: If a Kresling module is at the fully-folded (or collapsed) State-0, the associated number is “0.” If the module is at its unfolded (extended) State-1 without locking, the corresponding label is “1.” Finally, if the module is at the fully extended and locked State-2, we label it “2.” For example, the second image in Figure 4.11(C) is labeled as 0002 because the first module at the base is fully extended and locked. Therefore, one can mimic the irreversible plant growth by activating the Kresling module from the fully compressed State-0 (before growth) to extended State-1 (during growth) and finally to locked State-2 (growth complete). In the fifth and sixth image in Figure 4.11(C), we set the second module from the base at State-1, which has some bending flexibility for robotic maneuver. It could be swiveled 360° to search the appropriate direction for the robot to grow. Here, we show two directions with respect to the viewpoint – left, denoted as ‘L’, and right, denoted as ‘R’.

Yoshimura Structure

The Yoshimura model shown in the fig 4.10 has been recreated with bistable CFRPs at the triangular facets. This sample with bistable laminates is through initial tests for identifying the range of actuation force required to lock the structure from a partially unfolded state. This gives an elementary idea for the selection of an actuator that would help in unfolding the structure. The size of the structure is defined by its characteristic length, $L = 210$ mm. Therefore, the diameter of the sample is estimated to be ≈ 201 mm and measured is 205 mm, whereas the height of the module is estimated to be 121 mm and the measured is 125

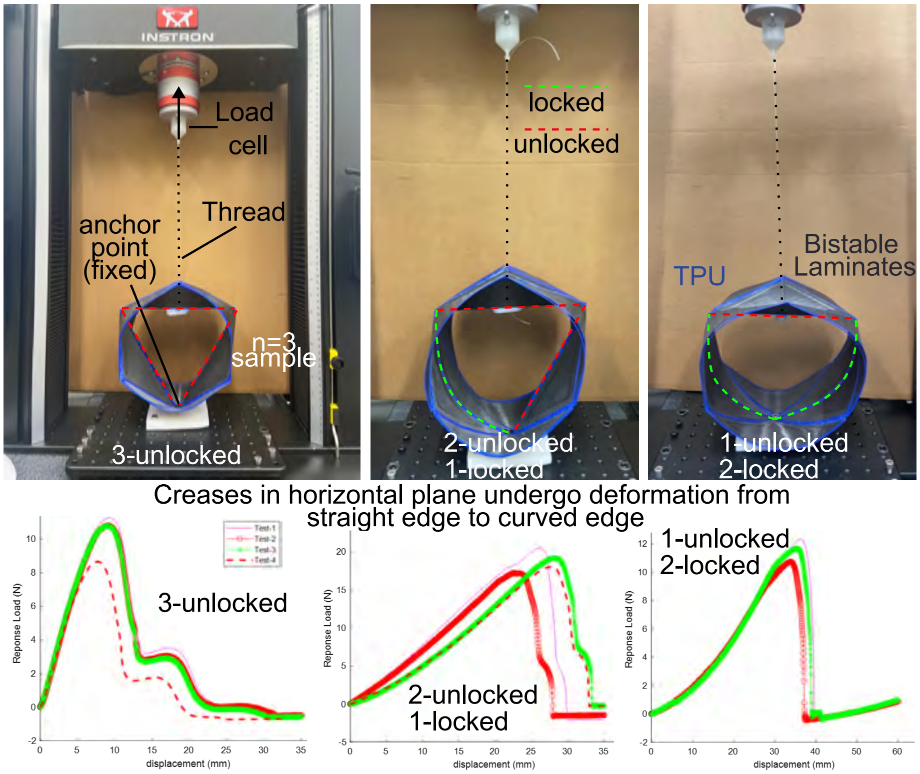

Figure 4.12: Yoshimura result: The first image shows the experimental setup to measure the actuation force required to snap the horizontal crease from unlocked state to a locked state. Note: the Yoshimura model used in the experiments is fabricated through bistable CFRP laminates at triangular facets and TPU material at the creases.

mm (estimation are based on the equations 4.1 - 4.3).

The first image in the figure 4.12 explains the setup for measuring the activation force for each unlocked horizontal crease in the module. The boundary condition enforced on the module suggests a need for an anchor point to hold the module and then apply force at the opposite horizontal crease. The activation force is applied to the crease through a fish line (marked as thread in the figure) that is attached to the load cell. This load cell has a prescribed displacement upwards until the crease snaps to the locked configuration. We observe that the unfolding mechanics of a crease differs with the number of unlocked and locked creases. The maximum force required to snap the crease from the unlocked state to the locked state varies in the range of $12 - 20$ N with a snap-through displacement required in the range of $25 - 35$ mm. More experiments will be needed for any more conclusive results. Similar experiments will be followed to analyze the completely 3D-printed model in the future.

4.5 Conclusion

We observe that many origami structures have a prominent folding pattern, commonly known as a waterbomb base, which is selected for integrating with bistable laminates. A preliminary look into such waterbomb laminates reveals multiple configurations that each have their own merits. The geometry has two prominent folding patterns that are compared below for their properties in the table 4.3.

Therefore, these new origami-inspired waterbomb laminates provide the readers with some ground-breaking takeaways –

1. Locking behavior: incorporating bistable laminates into the origami structure such as the waterbomb geometry used here could provide locking behavior. This would be beneficial in achieving load-bearing capacity and increasing compression stiffness.
2. Switchable behavior: essentially adding the locking behavior, one can switch from a foldable state of the structure to a rigid, non-foldable state.
3. Tunable performance: with understanding the design parameters of origami structures and bistable laminates, it is possible to embed provisions to tune the performance on-demand.

Therefore, this study makes a crucial advancement in the field of morphing structures, using bistable laminates to achieve multi-functionality.

Properties	X-crease pattern	I-crease pattern
Foldability: kinematics of geometric folding of patterns	1. Very compact structure: flat-folds into a much smaller surface area. 2. Fabrication: relatively difficult, has a lot of flexible connections, more number of parts. 3. Limitations: angle $\theta \geq 90°$ otherwise not flat-foldable.	1. Compact: Only shows flat-foldabiity, acquires larger surface area after folding. 2. Fabrication: Easier to fabricate, just one crease in the geometry. 3. Limitation: No limitations on geometry, always flat-foldable
Curvature Influence: effectiveness of laminate curvature on locking creases to fold	1. Trend: shows decreasing influence as the angle θ decreases 2. Locking ability: compromised, curvature along the laminate changes with direction	1. Trend: Maximum influence as the curvature is highest in the horizontal direction 2. Locking ability: Best when the crease is oriented in the direction of curvature
Locked Stiffness (High): when no folding is allowed	Depends on the X-crease angle θ - increases with increasing angle	Does not affect the stiffness (for waterbomb laminates with constant X-crease)
Load-bearing ability: at locked configuration	Increases with the increase in the X-crease angle θ	Not affected with increasing Aspect ratio (for waterbomb laminates with constant X-crease)
Folding stiffness (soft): when flat-folding along respective creases	1. Lowest stiffness, flexibility at all creases 2. Effect of parameter: not much affected with changing either X-crease angle or Aspect ratio	1. Low stiffness but higher in comparison to X-fold pattern 2. Effect of Parameter: Higher aspect ratio (AR) increases the stiffness as more crease material undergoes bending
Uses	Common occurrence in origami structures such as waterbomb, miura-ori, yoshimura robots	Single-fold structures such as Kresling

Table 4.3: Comparison table between properties of the laminate with having either the X-fold and I-fold in the geometry.

Chapter 5

Future Work

Bistable laminates future studies

1. Comprehensive in-plane testing: We were able to present the quasi-static in-plane compression testing of bistable laminates. For a more comprehensive understanding of the material behavior, the following tests are suggested -
   (a) Fatigue testing: upon understanding the quasi-static in-plane testing, it is crucial to understand the fatigue response of such bistable laminates. Switchable sandwich cores, when implemented, would be in continuous operation, thereby experiencing a cyclic loading. Interestingly, if you pull the laminate from the soft state in the tensile direction, it automatically shifts to the previous stiff state. Hence, this cyclic loading would test the energy losses and give an idea about durability over multiple cycles. This study would provide insights to make the laminate tougher and resilient.
   (b) Creep test: These bistable laminates are affected by environment factors such as moisture, temperature. Hence, over a sustained exposure to changes in environment, the laminates in in-plane compression might buckle before they reach their maximum potential. A controlled-environment creep test could help understand the effects of each parameter and might give insights to protect the laminates.
   (c) Impact loading: The laminates are more susceptible to impact loading damages

due to their complex localized buckling during compression. When the stiff-state laminate is applied to compression loading, it produces a three-step process for buckling, as seen in the chapter 3. If impact loading is applied, the laminate does not have time to go through these different buckling modes and could induce complex modes, which result in premature damage of laminates.

2. Inverse design of bistable laminates for tuned performance: This study establishes a few parameters that affect their compression characteristics, such as the aspect ratio, curvature, or stacking sequence. A semi-analytical model is also observed to predict its behavior in a reasonable agreement. Hence, it would be crucial to understand the inverse process of designing these bistable laminates for certain applications that require specific performance characteristics such as load-bearing capacity, stiffness, or even the folding patterns by embedding creases in the geometry. Our study stands as a base to help guide further research into designing morphing structures according to the need.

3. Improving life-expectancy of bistable laminates: currently, it is well understood that environmental factors degrade their performance over time. Being an unconventional material, it undergoes large deformations during its oscillations from one state to the other. This performance degrades over time due to settling of humidity, temperature cycles, chemical corrosion, etc. Hence, there is an increasing need to find a solution to coat these laminates with weather-proofing solutions. However, it needs to be studied carefully so that this coating does not affect the performance of such laminates.

4. Multi-modal morphing structures: waterbomb laminates presented in the above chapter 4 have features that are common to various known origami structures. Hence, one could deploy these conceptual laminates to various robotic structures that require reconfiguration for multiple purposes. For example, the waterbomb laminates could

be folded in a similar pattern as the Kresling module. However, a Kresling module has a specific direction in which it twists and expands, such as clockwise (CW) or counter-clockwise(CCW) motion. Many researchers have used this to create a crawling worm-like robot [100]. Here, the waterbomb laminates significantly upgrade the design as it could be twisted in either direction, i.e., CW or CCW. With a carefully designed robotic system, one could create a multi-modal crawling robot that has umpteen applications ranging from long search-expedition robots, excavating robots to tiny medical robots for drug deliveries.

5. In-space manufacturing robotic arms: Bistable laminates have been increasingly studied for space exploration, building colonies, and in-space manufacturing equipment owing to their deploying characteristics and efficient packaging. We believe the origami structures incorporated with bistable laminates could provide a strong base to create switchable robotic arms that could be deployed in space. And later, on-demand could be activated to lock-in to different configurations for carrying-out simple, yet dangerous in-space welding, assembling, and servicing tasks.

Chapter 6

Supporting Study: High-fidelity analytical model for shape prediction of bistable CFRP laminate

Publication Details

Other Authors: Shoab Chowdhury, Oliver Myers, Suyi Li.

Title: “High-fidelity analytical modeling of asymmetric CFRP composites using Reissner–Mindlin theory and hygroscopic degradation”

Journal: Composites Science and Technology, vol. 236, p. 109983, 7 (2023).

Abstract

Multi-stable carbon fiber-reinforced composites with asymmetric ply layouts have shown promising potential for creating multi-functional structural systems. To design and analyze these complex composites, high-fidelity and computationally efficient analytical models are crucial. To this end, Hyer and Dano formulated the first model four decades ago based on classical lamination theory (CLT). Surprisingly, despite many follow-up studies to refine this analytical approach, current models still follow the same fundamental ingredients

used in Hyer and Dano's original work. As a result, they all inherited the same limitations. For example, they ignore the interlaminar stresses and lack a rigorously calibrated hygroscopic term. To overcome these limitations, we propose a new analytical modeling approach by adopting the Reissner-Mindlin theory and hygroscopic degradation. This new model introduces in-plane rotations as two additional degrees of freedom and a combined expansion coefficient for the epoxy matrix materials. Compared to finite element simulations and experiment data, the new model can estimate the interlaminar stress reasonably well (especially regarding its concentration near the edges) and predict the laminates' external shape more accurately than an equivalent Hyer's model. The new model can also accurately predict the reduction in the laminate's curvature and snap-through force in different design configurations, as well as their linear correlation to the moisture content levels. Overall, the results of this study present a fundamental advancement in the analytical modeling of asymmetric multi-stable composite laminates, offering a broad and versatile foundation for designing and analyzing the next generation of multi-functional composite structures.

6.1 Introduction

Over the past decade, we have witnessed a rapidly increasing demand for adaptive multifunctional structures systems that can perform multiple tasks besides load-bearing. These adaptive structures have offered many exciting capabilities such as mechanical property control [101, 102, 103], energy harvesting [16, 23], mechano-digital hybridization [104, 105, 106], and even physical intelligence [33, 34, 107]. To this end, multi-stable carbon fiber reinforced composite with asymmetric fiber layouts is an excellent platform for such structural adaptation and functionalization. This is because combining fiber composite and multi-stability brings out the most promising advantages of these two concepts: Carbon fiber composites feature superior mechanical properties such as a high strength-to-weight ratio and stiffness-to-weight ratio, making them the preferred option for lightweight systems [108, 109]. On the other hand, multi-stability – created by the thermally-induced residual stresses from asymmetric ply layout – can enable a wide variety of adaptive functions. As a result, multi-stable carbon fiber laminates have become popular in aerospace structures [15, 110, 111], wind turbine blades [112, 113], automobiles [2], and energy harvesting systems [24].

At the most elementary level, a composite laminate patch with an asymmetric fiber layout can exhibit two distant stable equilibria (or stable states) (Figure 6.1a,b). Such *bistable* laminate's external shapes are close to cylindrical at these stable states, and the corresponding cylindrical axis' orientation and curvatures are directly related to the underlying design parameters, such as fiber orientation (ϕ), play arrangement, and laminate size. Moreover, one can "snap" the laminate from one stable state to the other by applying a transverse external force (Figure 6.1b), and the corresponding critical force to achieve such snap is called snap-through force.

Therefore, to fully uncover the potential of these asymmetric and adaptive carbon fiber composites, it is essential to formulate high-fidelity analytical models to predict their multi-stability and snap-through behaviors. To this end, Hyer and Dano developed the first model in their seminal paper in 1981 [10, 11]. This model adopted the Classical Lamination theory (CLT), where they assumed the laminate's external shape at stable states using constant curvatures. They also approximated the laminate's strain and out-of-plane deformation field using simple polynomial functions. Many subsequent studies improved upon this theoretical model to incorporate higher-order polynomial functions [14, 27], arbitrary fiber lay-ups [13], multiple-patched designs [43, 46, 48, 114], and nonlinear dynamics [115]. The predictions from these models regarding laminate shapes and snap-through load can agree reasonably well with finite element simulations and experiment data.

However, to the author's surprise, all analytical models reported in the literature so far have followed the same fundamental ingredients used in Hyer and Dano's original model: classical lamination theory. As a result, they all inherited the same fundamental limitations from the Kirchhoff's plate theory. Therefore, in this study, we propose a new analytical approach — using the more advanced Reissner-Mindlin plate theory and hygroscopic terms — to achieve new capabilities imperative for multi-stable composites' functionalities and practical operations.

Firstly, the new model can also predict the interlaminar stresses in multi-stable fiber composites besides the in-plane stresses. Understanding these stresses is crucial to prevent delamination at the composite laminate's edge [116, 117, 118], ensuring long-duration operations. Moreover, many multi-stable composites are integrated with layers of responsive materials on their surface to achieve actuation or energy harvesting [119, 120, 121, 122]. These responsive materials typically interact with the host composite via shear stress; therefore, the new analytical model can facilitate the rapid design of such a system.

Secondly, our new model incorporates an accurately calibrated component to predict the influence of moisture absorption. Composite laminate's external shapes and mechanical properties can deviate significantly from their original values due to changes in the working environment, necessitating the incorporation of environmental factors like moisture into analytical modeling. Indeed, exposure to moisture for an extended time has substantial effects on composite's performance in general [123], resulting in lower strength and stiffness [124, 125, 126, 127], interfacial debonding between fiber and the matrix [128], increased glass transition temperature [129], shape distortion [130], and deteriorated existing damage due to highly concentrated swelling strains [131]. For asymmetric composites, moisture absorption and the subsequent relaxation of residual stress would eventually cause the critical loss of multi-stability [132]. Therefore, an analytical model validated by extensive experiment data

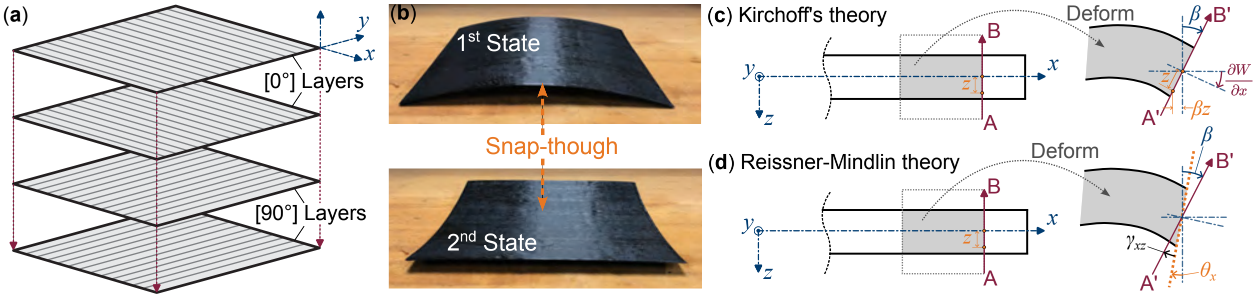

Figure 6.1: Overview of the bistable composite laminate and its different modeling approach. (a) A composite laminate with an asymmetric fiber ply layout (such as [0°/0°/90°/90°] in this case) can show two distant stable states. (b) One can snap the laminate between these two states by an external force, commonly known as "snap-through". (c) The deformation kinematics underpinning the Kirchoff plate theory. The red arrow depicts the normal of the mid-plane, and it is the same as the cross-section rotations. This means $\beta = \theta_x$, where β is the mid-plane rotation and θ_x is cross-section area rotation ($\tan(\theta_x) \approx \sin(\theta_x) \approx \theta_x$). (d) The deformation kinematics underpinning the Reissner-Mindlin plate theory. The normal direction of the mid-plane is different from cross-section rotation.

can ensure robust design against "real-world" conditions.

This paper details the formulation and validation of the new analytical model for multi-stable asymmetric composites. In what follows, we first discuss the limitations of the current modeling approach pioneered by Hyer and Dano. Then, we detail the formulation of the new model by combining the classical lamination theory with the Reissner-Mindlin plate theory. The accuracy of this new analytical model is assessed with the finite element simulations based on experimentally calibrated constitutive properties. Besides the unique capability of predicting interlaminar stress, the new model can also predict the laminate's external shapes more accurately than the current approaches. Then, we shift our focus to the moisture effects, detailing the formulation of experimentally calibrated hygroscopic terms. The theoretical predictions of moisture effects also show good agreement with finite element simulations. Overall, the new modeling framework provides a versatile foundation for engineering the next generation of adaptive and multi-functional composite structures.

6.2 Limitation of Current Modelling Approach

6.2.1 Re-examining Classical Lamination Theory and Interlaminar Stress

Usually, CLT is the default choice for engineering researchers when analyzing composite laminates, particularly bistable composites, due to its ease of application to different structural configurations. However, CLT inherits some fundamental assumptions from Kirchhoff's theory. These assumptions, if not carefully considered, could result in unexpected inaccuracies and over-confidence in the model's capabilities. Kirchhoff's plate theory imposes several fundamental assumptions regarding the deformation kinematics of the composite structure, of which the more consequential/critical assumption states that the slope of the deformed laminate's mid-plane equals the rotation angle of the corresponding cross-section area as observed in Figure 6.1(c). While appropriate for thin symmetric laminates, this assumption would underestimate the unsymmetric laminate's deformation, making it appear stiffer than the actual values.

Moreover, this assumption completely neglects interlaminar stresses. Interlaminar stress originates from the difference between the deformed mid-surface slope and the cross-section rotation, so it turns out to be exactly zero based on the current models. Such simplification creates an inconsistency in the stress field definition, especially at the laminate's free edges (also referred to as the *free-edge effect* [133]). This free-edge effect is well-studied for symmetric laminates [134, 135], but for asymmetric laminates with bistability, it received very little attention.

To understand these interlaminar stresses, we conduct a finite element simulation on a square-shaped thin laminate plate in ABAQUS CAE 2020. This laminate consists of two layers of fiber ply of different ply angles ([0°/90°]); hence it is asymmetric. Its size is 100mm × 100mm × 0.24mm, and its constitutive material properties, summarized in Table 6.1, are calibrated from experiment data (Appendix Section A). We mesh the laminate using 3D quadratic brick elements with reduced integration (C3D20R). The element size is 2mm × 2mm × 0.06mm, giving four layers of elements through the laminate's thickness. Details regarding finite element simulations are available in Appendix Section B.1.

Figure 6.2(b) summarizes the finite element results. The distribution of interlaminar stresses τ_{xz}, τ_{yz} (or S13, S23) are plotted against the $x-$ and $y-$coordinates of axes in the laminate's mid-plane. These stresses are minimal for most parts but become significantly higher near the edges. Interestingly, these interlaminar stresses remain almost the same between the two stable states, regardless of the inversion of the laminates' overall curvature. Researchers have shown these stresses could reach singularity with approximated elasticity solutions [136]. One can understand these interlaminar stresses' origin by closely examining the two elements at the boundary (Figure 6.2c). Here, the first element is from the middle of the left edge near the mid-plane (Point 1 in Figure 6.2a). τ_{xy} (or S12) is acting in the laminate layer, and the element experience this stress on three faces: d-e-h-a, e-f-g-h, and f-c-b-g. But the face a-b-c-d is traction free, so it must be stress-free. To balance these stresses, another stress τ_{xz} (S13) must act on this element's upper and bottom surfaces. Similarly, the second element, located in the middle of the adjacent edge, must have a stress τ_{yz} (or S23) on its top and bottom surfaces. Overall, the high interlaminar stresses near the edge are similar to those

Table 6.1: Material properties of the CFRP based on experimental data. E_i and G_{ij} are in the units of GPa, α_{ii} is in $^\circ\mathrm{C}^{-1}$. Ply thickness $h = 0.12$ mm. Details regarding the material property calibration experiment are available in Appendix Section A.

Property	Value	Property	Value	Property	Value	Property	Value
E_1	140	G_{12}	5	ν_{12}	0.3	α_{11}	-2×10^{-8}
E_2	9.4	G_{13}	7.17	ν_{13}	0.3	α_{22}	2.4×10^{-5}
E_3	9.4	G_{23}	3.97	ν_{23}	0.4	α_{33}	2.4×10^{-5}

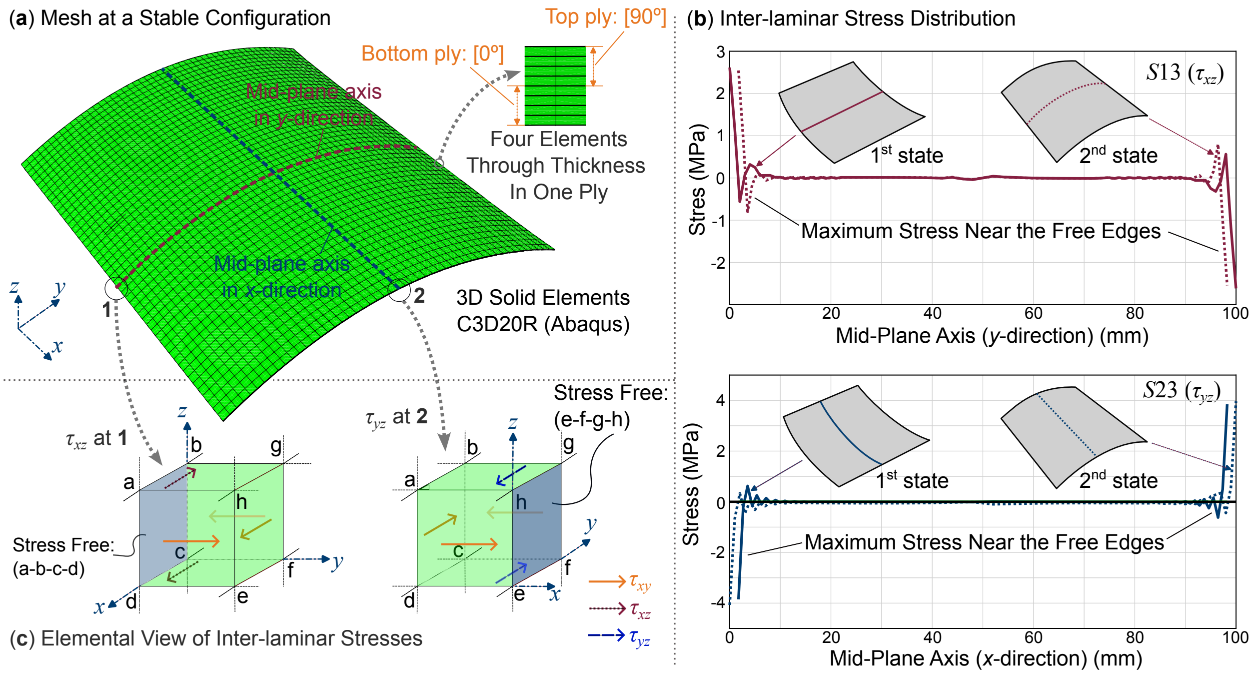

Figure 6.2: Interlaminar stresses analysis based on the finite element simulation using 3D solid elements. (a) The meshed laminate settled in one of its stable states. (b) Interlaminar stress distributions in the laminate through the mid-plane axes at the two stable states. Note the mid-plane y-axis' length, when projected on the reference frame, is shorter in the 2^{nd} stable state than the 1^{st} state due to the laminate's cylindrical shape. Similarly, the mid-plane x-axis' length is shorter at the 1^{st} state.
(c) Elemental view at the free edge explaining the origin of interlaminar stresses.

observed in the symmetric fiber laminates.

The neglection of such interlaminar stresses in the classical lamination theory means the free edges are technically not stress-free. Such artificial shear stress on the free edges makes the laminate appear stiffer than the actual value, resulting in under-estimated deformation after curing and over-estimated natural frequencies [137]. In reality, the interlaminate stress can become very high near the edges to ensure moment equilibrium about the out-of-plane axis. And such high stress can cause local delamination, a failure that the current models can not explain. These issues motivate us to formulate a more elaborated theory in Section 3.

6.2.2 The Importance of Considering Moisture Effects

Prior experimental, analytical, and finite element studies confirmed that multi-stable composites could experience significant changes in geometric shapes and mechanical properties due to moisture absorption. For example, the principal and twisting curvatures of the cylindrical-shaped multi-stable laminates decrease linearly as the absorbed moisture content increases [138, 139, 140, 141]. Such correlations are typically related to the fiber ply layout designs. Besides curvatures, moisture absorption can significantly reduce the force needed to snap the laminate from one stable equilibrium to another (aka. snap-through force) [132, 142]. These moisture absorption effects are reversible. One can reduce or even eliminate the absorbed moisture by placing the multi-stable composite under a controlled environment with an elevated temperature and low humidity, recovering the composite's original geometric shape. However, the composite laminate can absorb moisture again. Such absorption-desorption-resorption cycles can repeat several times with predictable results [138].

More careful analysis revealed that these moisture effects originate from the hygro-thermo-elastic stresses [143], especially in the epoxy matrix materials. Epoxy is a polymer material with a cross-linked network that forms a voided structure. When exposed to moisture, these voids allow the water molecules to diffuse through the polymer network [144]. In this process, the inter-chain Van der Waals bonds break down, and new hydrogen bonds are formed [145]. As a result, the polymer chain mobility increases, and residual thermal stresses and strains from the thermal curing process start to relax. This process is called “plasticization” of the cross-linked polymer network [129, 144, 145]. One can accurately characterize these behaviors based on the hygroscopic strain as a function of absorbed moisture content.

However, besides the significance of understanding moisture absorption effects, the relevant studies are scarce, sometimes with contradictory conclusions [140, 141]. More importantly, there is still a critical lack of an *accurately calibrated* analytical model. The studies mentioned above have proposed different models to incorporate moisture effects, but the validations were not comprehensive. For example, the reduction of snap-through force was only measured at one moisture content level or assessed only as a function of exposure time. Moreover, only a few laminate ply layouts are tested.

Therefore, in this study, we will incorporate moisture absorption formulation in our proposed new analytical model and thoroughly calibrate it based on experiments and finite element simulations. Specifically, we will validate the model predictions at different moisture content levels and asymmetric fiber ply configurations (aka. 2-ply, 4-ply, and 6-ply laminates), ensuring our results' accuracy and broad applicability.

6.3 Adopting Reissner-Mindlin Theory to CLT

To address the fundamental limitations inherited from using Kirchoff's plate theory, we propose to adopt the Reissner-Mindlin theory (or RM theory) that allows the in-plane stress τ_{xy} near the free edges to be balanced by the interlaminar stresses [146, 147]. This way, the free edge surfaces become strictly stress-free. The Reissner-Mindlin theory introduces two additional independent parameters — rotation about the $y-$axis θ_x and rotation about the $x-$axis θ_y — in addition to the transverse displacement field W_0. One can understand this setup from Figure 6.1(d): The cross-section $A - B$ is initially straight and normal to the laminate's mid-plane, after deformation, $A' - B'$ is still straight, but *no longer normal to the mid-plane*. Therefore, these rotations about the mid-plane are additional degrees of freedom to better approximate the laminate deformation.

6.3.1 Underpinning Formulation

The total potential energy of the laminate is a function of the total stiffness of all fiber plies, the mid-plane strains and curvatures, and thermal loads and moments. Mathematically, the energy is expressed as follows,

$$\Pi = \int_{-\frac{L_x}{2}}^{\frac{L_x}{2}} \int_{-\frac{L_y}{2}}^{\frac{L_y}{2}} \left\{ \frac{1}{2} \begin{bmatrix} \boldsymbol{\epsilon}_0 & \boldsymbol{\kappa} \end{bmatrix} \begin{bmatrix} \mathbf{A} & \mathbf{B} \\ \mathbf{B} & \mathbf{D} \end{bmatrix} \begin{bmatrix} \boldsymbol{\epsilon}_0 \\ \boldsymbol{\kappa} \end{bmatrix} - \begin{bmatrix} \boldsymbol{\epsilon}_0 & \boldsymbol{\kappa} \end{bmatrix} \begin{bmatrix} \mathbf{N}_t \\ \mathbf{M}_t \end{bmatrix} \right\} \mathrm{d}y \, \mathrm{d}x. \tag{6.1}$$

Here, L_x and L_y are laminate sizes. The $\boldsymbol{\epsilon}_0$ refers to the reduced mid-plane strain vector and $\boldsymbol{\kappa}$ refers to the curvature vector. These are explained later in this section.

The other terms in Eq. (6.1): $\mathbf{A}$ refers to the extension-shear coupling, $\mathbf{B}$ refers to the bending-extension coupling, and the $\mathbf{D}$ refers to the bending-twist coupling. They are functions of the overall stiffness matrix, which could be calculated using summations as follows [137],

$$\begin{aligned} \mathbf{A}_{ij} &= \sum_{k=1}^{k=n} \overline{\mathbf{Q}}_{ij}^{(k)} \left(z_k - z_{k-1} \right), \\ \mathbf{B}_{ij} &= \frac{1}{2} \sum_{k=1}^{k=n} \overline{\mathbf{Q}}_{ij}^{(k)} \left(z_k^2 - z_{k-1}^2 \right), \\ \mathbf{D}_{ij} &= \frac{1}{3} \sum_{k=1}^{k=n} \overline{\mathbf{Q}}_{ij}^{(k)} \left(z_k^3 - z_{k-1}^3 \right), \text{where, } i, j = 1, 2, 4, 5, 6 \end{aligned} \tag{6.2}$$

where the superscript $^{(k)}$ refers to different layers of fiber laminate ply, n is the total number of plies, z refers to the position along laminate thickness. i and j refer to the rows and columns of the reduced compliance matrix defined below in Eq. (6.4). The *global* stiffness matrix $\overline{\mathbf{Q}}$ (defined in the global coordinate system) is calculated based on the *material* stiffness matrix $\mathbf{Q}$ in that $\overline{\mathbf{Q}} = \mathbf{T}\mathbf{Q}\mathbf{T}^{\intercal}$, where $\mathbf{T}$ is the transformation matrix between the material coordinate along the fiber direction and the global $x-y$ coordinate. Denote ϕ as the angle between the fiber and $x-$ axis, $\mathbf{T}$ is calculated as

$$\mathbf{T}=\begin{bmatrix}\cos^2\phi & \sin^2\phi & 0 & 0 & -\sin 2\phi\\ \sin^2\phi & \cos^2\phi & 0 & 0 & \sin 2\phi\\ 0 & 0 & \cos\phi & -\sin\phi & 0\\ 0 & 0 & \sin\phi & \cos\phi & 0\\ \sin\phi\cos\phi & -\sin\phi\cos\phi & 0 & 0 & \cos 2\phi\end{bmatrix}. \tag{6.3}$$

and $\mathbf{Q}$ is the inverse of constitutive compliance matrix $\mathbf{S}$ based on the orthotropic properties of the fiber ply material in that $\mathbf{Q}=\mathbf{S}^{-1}$, and

$$\mathbf{S}=\begin{array}{c|ccccc|} & 1 & 2 & 4 & 5 & 6\\ \hline 1 & \frac{1}{E_1} & \frac{-\nu_{12}}{E_1} & 0 & 0 & 0\\ 2 & \frac{-\nu_{12}}{E_1} & \frac{1}{E_2} & 0 & 0 & 0\\ 4 & 0 & 0 & \frac{1}{G_{23}} & 0 & 0\\ 5 & 0 & 0 & 0 & \frac{1}{G_{13}} & 0\\ 6 & 0 & 0 & 0 & 0 & \frac{1}{G_{12}}\\ \hline \end{array} \tag{6.4}$$

$\mathbf{N}_t$ in Eq. (6.1) is a vector of thermal forces induced by the temperature drop in the curing process, and $\mathbf{M}_t$ is a similar thermal moments vector:

$$\begin{aligned}\mathbf{N}_t &= \sum_{k=1}^{k=n}\overline{\mathbf{Q}}_{ij}^{(k)}\overline{\boldsymbol{\alpha}}\nabla T\left(z_k-z_{k-1}\right),\\ \mathbf{M}_t &= \frac{1}{2}\sum_{k=1}^{k=n}\overline{\mathbf{Q}}_{ij}^{(k)}\overline{\boldsymbol{\alpha}}\nabla T\left(z_k^2-z_{k-1}^2\right).\end{aligned} \tag{6.5}$$

Here, $\overline{\boldsymbol{\alpha}}$ is the vector of the transformed coefficient of thermal expansions in that $\overline{\boldsymbol{\alpha}} = [\boldsymbol{\alpha}^*_{11}\ \boldsymbol{\alpha}^*_{22}\ \boldsymbol{\alpha}^*_{23}\ \boldsymbol{\alpha}^*_{13}\ \boldsymbol{\alpha}^*_{12}]^\intercal$, where $\boldsymbol{\alpha}^* = \mathbf{T}^*\boldsymbol{\alpha}\mathbf{T}^{*\intercal}$, and

$$\begin{aligned} \boldsymbol{\alpha} &= \begin{bmatrix} \alpha_{11} & 0 & 0 \\ 0 & \alpha_{22} & 0 \\ 0 & 0 & \alpha_{33} \end{bmatrix}, \\ \mathbf{T}^* &= \begin{bmatrix} \cos\phi & -\sin\phi & 0 \\ \sin\phi & \cos\phi & 0 \\ 0 & 0 & 1 \end{bmatrix}. \end{aligned} \tag{6.6}$$

Material properties are listed in Table 6.1. The mid-plane strain vector $\boldsymbol{\epsilon}_0$ and curvature vector $\boldsymbol{\kappa}$ are adopted from Reissner-Mindlin theory and modified for our model as,

$$\boldsymbol{\epsilon}_0 = \begin{bmatrix} \epsilon_{x0} \\ \epsilon_{y0} \\ \gamma_{yz0} \\ \gamma_{xz0} \\ \gamma_{xy0} \end{bmatrix}, \quad \boldsymbol{\kappa} = \begin{bmatrix} \kappa_x \\ \kappa_y \\ \kappa_{yz} \\ \kappa_{xz} \\ \kappa_{xy} \end{bmatrix} = \begin{bmatrix} -\frac{\partial\theta_x}{\partial x} \\ -\frac{\partial\theta_y}{\partial y} \\ 0 \\ 0 \\ -\left(\frac{\partial\theta_x}{\partial y} + \frac{\partial\theta_y}{\partial x}\right) \end{bmatrix}. \tag{6.7}$$

Note that these strain and curvature formulations deviate fundamentally from the currently available models due to the additional rotational degrees of freedom. The formulation of the proposed new model involves five independent quantities - mid-plane strain field ϵ_{x0} and ϵ_{y0}, out-of-plane displacement field W_0, and the cross-sectional area rotation θ_x and θ_y. These quantities need to be approximated using appropriate polynomials, and all other quantities are derived from them. Here, we use the approximations by Hyer and Dano for the mid-plane strains ϵ_{x0} and ϵ_{y0} so that [14]

$$\begin{aligned}\epsilon_{x0} &= c_1 + c_2\frac{x^2}{L_x^2} + c_3\frac{y^2}{L_y^2} + c_4\frac{xy}{L_xL_y},\\ \epsilon_{y0} &= c_5 + c_6\frac{x^2}{L_x^2} + c_7\frac{y^2}{L_y^2} + c_8\frac{xy}{L_xL_y}.\end{aligned} \tag{6.8}$$

The most critical assumption here is the out-of-plane displacement field that defines the external shape of the bistable laminate. Hyer and Dano used a constant curvature formulation, so there are only three terms in their W_0 definition [13, 14]. However, we assume a higher-order polynomial for better accuracy. We use a third order-polynomial to define the $z-$displacement field:

$$\begin{aligned}W_0 = c_9\frac{x^2}{L_x^2} + c_{10}\frac{y^2}{L_y^2} + c_{11}\frac{xy}{L_xL_y} + c_{12}\frac{x^2y}{L_x^2L_y}\dots\\ +c_{13}\frac{xy^2}{L_xL_y^2} + c_{14}\frac{x^3}{L_x^3} + c_{15}\frac{y^3}{L_y^3},\end{aligned} \tag{6.9}$$

The cross-section rotations are also approximated based on third-order polynomials:

$$\begin{aligned}\theta_x &= c_{16}\frac{x}{L_x} + c_{17}\frac{y}{L_y} + c_{18}\frac{xy}{L_xL_y} + c_{19}\frac{x^3}{L_x^3} + c_{20}\frac{y^3}{L_y^3},\\ \theta_y &= c_{21}\frac{x}{L_x} + c_{22}\frac{y}{L_y} + c_{23}\frac{xy}{L_xL_y} + c_{24}\frac{x^3}{L_x^3} + c_{25}\frac{y^3}{L_y^3}.\end{aligned} \tag{6.10}$$

The laminate curvatures, which are the first-order differentials of rotations, are second-order polynomials. The in-plane displacements are calculated using the strain definitions as follows,

$$
\begin{aligned}
U_0 &= \int \left[\epsilon_{x0} - \frac{1}{2} \left(\frac{\partial W_0}{\partial x} \right)^2 \right] \mathrm{d}x + g(y), \\
V_0 &= \int \left[\epsilon_{y0} - \frac{1}{2} \left(\frac{\partial W_0}{\partial y} \right)^2 \right] \mathrm{d}y + h(x).
\end{aligned}
\tag{6.11}
$$

The in-plane displacements have constants of integration, these are used to complete the polynomials using suitable approximations including the linear and cubic terms as follows,

$$
\begin{aligned}
g(y) &= g_1 \frac{y}{L_y} + g_2 \frac{y^3}{L_y^3}, \\
h(x) &= h_1 \frac{x}{L_x} + h_2 \frac{x^3}{L_x^3}.
\end{aligned}
\tag{6.12}
$$

The rigid body rotations in the in-plane displacement field would be introduced due to the functions above. If rigid body motion does not occur, one can impose a constraint $g_1 = h_1$ to eliminate one undetermined constant. The in-plane shear is a function of the in-plane and out-of-plane displacement in that

$$
\gamma_{xy0} = \frac{\partial U_0}{\partial y} + \frac{\partial V_0}{\partial x} + \frac{\partial W_0}{\partial x} \frac{\partial W_0}{\partial y}.
\tag{6.13}
$$

Lastly, the non-trivial inter-laminar shear strains, which are an integral part of this new analytical approach, can be obtained by

$$
\begin{aligned}
\gamma_{yz0} &= \frac{\partial W_0}{\partial y} - \theta_y \ ; \\
\gamma_{xz0} &= \frac{\partial W_0}{\partial x} - \theta_x.
\end{aligned}
\tag{6.14}
$$

In the formulation above, these inter-laminar shear terms are third-order polynomials. This is consistent with the FEA results seen above. Therefore, we conclude that at least a third-order polynomial distribution is required to estimate the interlaminar shear.

Based on the formulations above, we arrive at a high-order polynomial function for the laminate's potential energy, where the unknown variables are the polynomial coefficients. There are eight undetermined coefficients from the mid-plane strain definitions, seven from the out-of-plane displacement field, ten from the rotations, and three from the integration constants. Hence, a total of 28 coefficients need to be determined. In comparison, the original Hyer's model [13, 14] had 14 undetermined constants. Therefore, our new analytical model is more computationally expensive but still much faster than finite element simulations.

We obtain the solution by minimizing the potential energy function (Eq. 6.1) using MATLAB's built-in multivariate optimizer `fmincon`. To expedite the calculations, we supply the `fmincon` solver with the gradients of the potential function with respect to each undetermined coefficient. In addition, we normalize the polynomial approximations by dividing every polynomial term by the length in that direction (either L_x or L_y) of the same order.

6.3.2 Interlaminar Stress

Our finite element simulation in Figure 6.2(b) shows that the interlaminar stress distribution has two noteworthy characteristics: First, it has a very high magnitude near the edge but is relatively negligible at the middle of the laminate. Secondly, the interlaminar stress at two opposite edges are the same in magnitude but opposite in sign, with an apparent anti-symmetry about the laminate's mid-point. These characteristics are possible only if the stresses are odd functions, implying that the interlaminar strains and the laminate's cross-section rotations are also odd functions.

To capture these characteristics, Eq. (6.10) in the new model's formulation approximates the

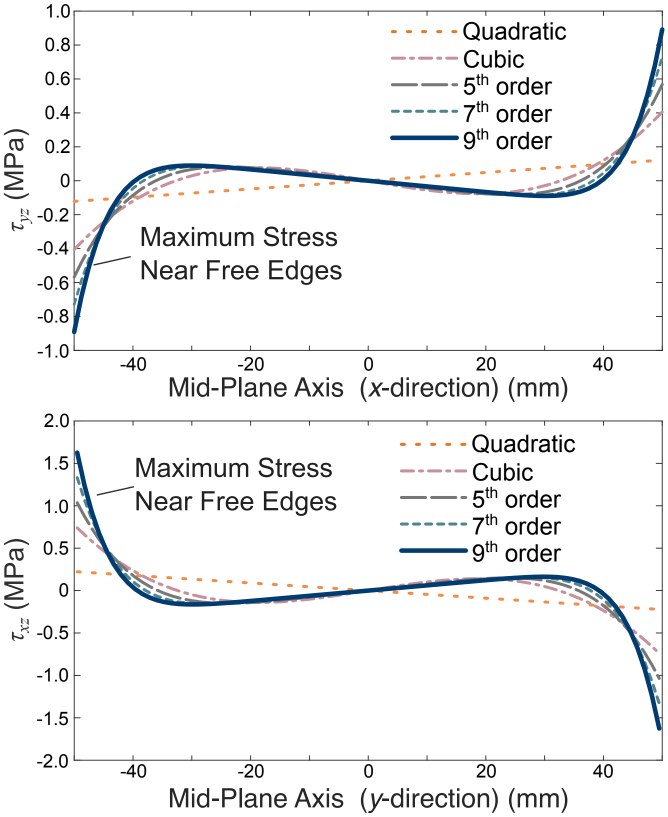

Figure 6.3: Interlaminar stress distribution for [0°/90°] laminate, obtained from the new analtyical model. The stress concentration near the free edge and corresponding magnitude is consistent with the finite element simulations shown in Figure 6.2.

cross-section rotation field by combining linear, quadratic (linear-twist), and cubic terms. This is the minimum requirement for appropriately estimating the inter-laminar stress distributions seen in finite element results. In addition, we compare the predicted interlaminar stress using higher-order polynomial functions for the rotation field (Figure 6.3). Specifically, we replace the polynomial terms in Eq. (6.10) containing c_{19}, c_{20}, c_{24}, and c_{25} by new polynomials with different orders — starting from simple quadratic terms to ninth-order. As the order of these polynomials increases, the predicted interlaminar stress becomes more concentrated near the laminate edges, showing a very similar trend and magnitude as the finite element result in Figure 6.2. Therefore, the proposed new analytical approach is an accurate yet computationally efficient tool for analyzing interlaminar stress.

6.3.3 Single-Patch Case Studies

To further gauge the new model's performance, we compare its predictions of the bistable laminates' external shapes with finite element simulations based on different laminate designs (see Table 6.2 for design details). Besides the laminate sizes and the number of plies, we also test different fiber layout orientations, including $\phi = 90°$, $60°$, $45°$, $30°$, and $0°$. These ply orientations have been widely used in previous studies; hence their results would be sufficient to elucidate the new model's performance.

Single Patch FEA Study

The bistable laminate in this finite element study is meshed using S4R *shell* elements with a mesh size of 2.5mm (that adopt the Reissner-Mindlin Theory) rather than the solid elements in the previous inter-laminate shear study. They can provide accurate predictions of laminate shape, and snap-through responses [148, 149] while significantly reducing computation time. The "Static Structural" module allows us to model the three selected configurations – two-ply, 100mm×100mm; four-ply, 100mm×100mm, and two-ply laminates, 200×200mm with the material properties listed in Table 6.1. After modeling, the laminate is cured at 135°C in the initial step and then cooled down to 20°C (room temperature) by fixing all degrees of freedom in the laminate, simulating the vacuum bagging procedure. This step allows the residual stresses to develop inside the laminate plies as there is a difference in the thermal expansion coefficients in the two in-plane directions. When we release the laminate after cooling and fix it only at its middle node, it deforms freely into one of the stable shapes. For comparison with analytical model predictions, we extract nodal displacements of thirteen selected points from the final FEA results: the four corners, the mid-point of every edge, the mid-point of all the four quadrants, and the center point (Figure 6.4), sufficiently capturing the overall shape and curvature of the laminates.

Evaluation Metrics

We evaluate the discrepancy between our new analytical model's predictions and the finite element simulation by comparing the laminate displacement at thirteen selected locations (Figure 6.4). In particular, we quantify the analytical model's performance using two measures. The first one is the root-mean-squared error (referred to as "R^2" hereafter):

$$R^2 = 1 - \frac{\sum_{j=1}^{13}(p_{\mathrm{A}} - p_{\mathrm{FE}})_j^2}{\sum_{j=1}^{13}(p_{\mathrm{A}})_j^2}, \tag{6.15}$$

where p_{A} is the selected nodal position vector based on the analytical result, p_{FE} comes from finite element simulations, and i indicates the selected node. An R^2 value closer to unity (1) means a better fit or more accurate model predictions.

Second, we define a normalized error percentage (e_n) to compare the results from different ply orientations, sizes, and ply thicknesses. This normalized error is the ratio between the maximum deviation between FEA and analytical predictions over the maximum laminate deflection along the out-of-plane $z-$direction.

Figure 6.4 summarizes the analytical and finite element predictions of two-ply square laminates of 100mm×100mm size and different fiber ply orientations. Four laminate designs are tested: each has a layer of 0°ply at the base, and the other ply's angle varies from 90°, 60°, 45°, to 30°. In addition, we compare the R^2 values of our proposed model and Hyer's model in Table 2. Notice that Hyer's model in this case study uses the same polynomial functions as the new model for approximating the out-of-plane displacement and mid-surface strains. Interested readers can refer to the authors' previous publication for the details of Hyer's model formulation [149]. It is also worth highlighting that the results are obtained only at

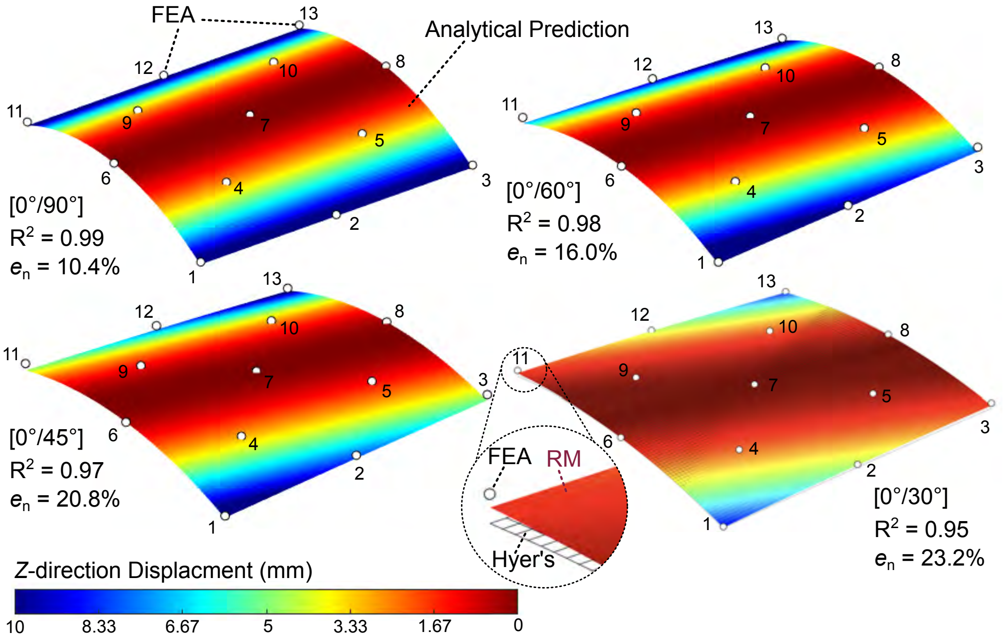

Figure 6.4: The external shape of two-ply laminates predicted by the new analytical approach. All these laminates have a base layer of 0°ply and a top layer of different fiber orientations. The predicted stable shapes from the analytical model are plotted as colored surfaces. White circles represent the positions of extracted nodal points from the finite element simulations. The *colorbar* shows the range of out-of-plane displacements, measured in mm. Note that for the [0°/30°] laminate, we also include the results from Hyer's model, shown by square mesh, to compare the accuracy between different analytical modeling approaches.

one stable state because the result at the other stable state would be the same.

Overall, the proposed new model can accurately predict the external shapes of different 2-ply laminates with consistently higher accuracy than Hyer's model. The best match occurs for the [0°/90°] laminate because it has a more regular, cylindrical shape in its stable state. On the other hand, the maximum discrepancy in nodal displacement is found in the [0°/30°] laminate's result due to the significant twisting curvature. At the two opposite corners (points 3 and 11) of the [0°/30°] laminate, the difference between model prediction and FEA is 1.9mm, corresponding to a normalized error of 23.2%. Note that this seemingly large error percentage is due to the small out-of-plane deformation, so even a tiny deviation in the model prediction would result in a significant normalized error. Regardless, the R^2

Table 6.2: Absolute discrepancy (measured in mm) between the FEA results and the new analytical model's prediction at selected nodes. Due to the symmetric nature of the laminates' shapes and underpinning polynomial equations, we only list the deviations at six nodes. Node 7 has zero discrepancies between FEA and model prediction because the laminate is fully fixed at this location.

Laminates & Selected Nodes							Performance Metrics		
Nodes	1	2	3	6	11	13	e_{n} (%)	R^2 (RM)	R^2 (Hyer)
2-ply laminate, 100mm×100mm									
[0°/90°]	1.1	0.1	1.1	0.5	1.1	1.1	10.4	0.99	0.96
[0°/60°]	0.7	0.8	1.9	0.5	1.9	0.7	16.0	0.98	0.93
[0°/45°]	0.8	1.2	2.2	0.5	2.2	0.8	20.8	0.96	0.89
[0°/30°]	0.6	1.0	1.9	0.5	1.9	0.6	23.2	0.95	0.83
4-ply laminate, 100mm×100mm									
$[0^\circ_2/90^\circ_2]$	0.6	0.0	0.6	0.0	0.6	0.6	10.5	0.99	0.97
$[0^\circ_2/60^\circ_2]$	0.2	0.1	1.2	0.0	1.2	0.2	18.5	0.96	0.89
$[0^\circ_2/45^\circ_2]$	0.5	0.0	1.3	0.0	1.3	0.5	22.1	0.96	0.76
$[0^\circ_2/30^\circ_2]$	0.6	0.1	1.2	0.1	1.2	0.7	27.3	0.91	0.72
2-ply laminate, 200mm×200mm									
[0°/90°]	2.5	0.1	2.6	0.5	2.6	2.5	5.8	0.99	0.97
[0°/60°]	1.6	1.0	1.6	0.7	1.6	1.6	3.3	0.99	0.96
[0°/45°]	1.1	0.5	1.1	0.7	1.1	1.1	2.5	0.99	0.92
[0°/30°]	2.1	0.8	0.8	0.2	0.8	2.1	5.6	0.99	0.88

value is still high above 0.95, suggesting that the new analytical model can offer an excellent estimation of laminate shapes. Moreover, the new model's accuracy is superior to Hyer's model, especially for the [0°/30°] laminate.

Next, we compare the new model's predictions to finite element simulations for thicker and relatively stiffer laminates. Figure 6.5 summarizes the results for 4-ply laminates consisting of two plies of 0°and another two with varying fiber orientations. The maximum discrepancy of 1.3mm is found in the [0/0/30/30] laminate, corresponding to a 27.2% normalized error. However, the R^2 values (rows 6-9 in Table 6.2) are still above 0.91, indicating that the model performs decently well for these thick laminates. In contrast, Hyer's model performs poorly with R^2 values dropping rapidly as the top two ply's fiber angle decreases — from $R^2 = 0.97$ for 90°to 0.72 for 30°.

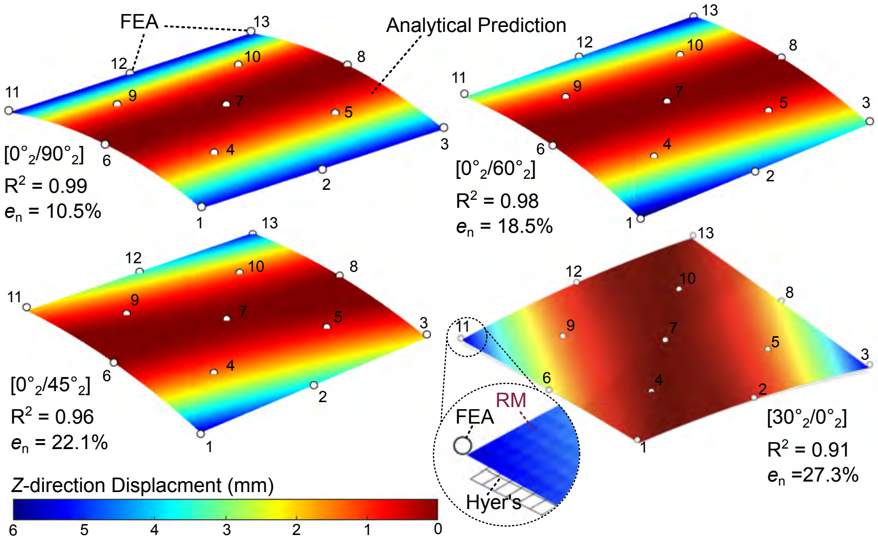

Figure 6.5: The predicted external shape for 4-ply laminates. They all have two layers of 0 ply angle, and the other two with different fiber orientations. The color bar shows $z-$ displacement values measured in mm. Again, the Hyer model's solution is added for the [30/30/0/0] laminate for comparison.

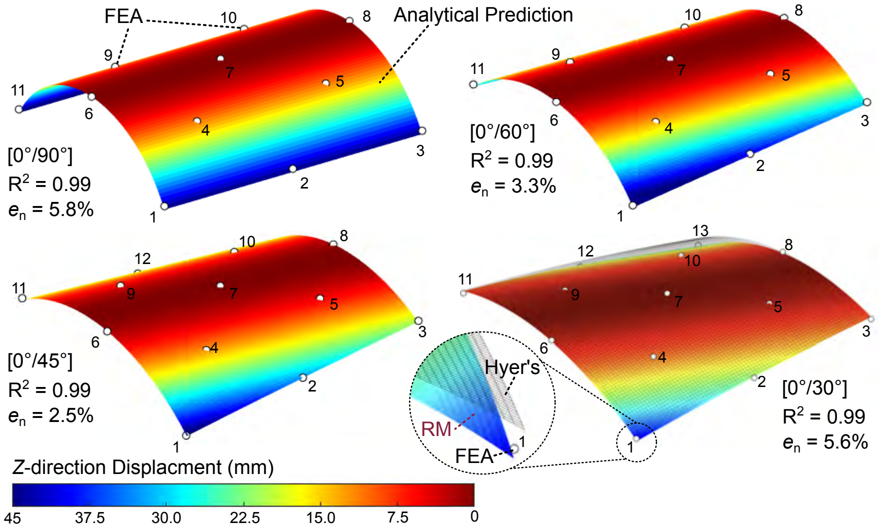

Figure 6.6: The predicted external shape of 2-ply laminates with a larger size — 200mm × 200mm. The color bar shows z-displacement values measured in mm. The closed-up analytical model comparison for the [0°/30°] laminate is viewed from a different angle.

Finally, Figure 6.6 summarizes the results for two-ply laminates with a larger dimension of 200mm×200mm. Surprisingly, despite the much more significant out-of-plane deformation in these larger laminates, the discrepancies in nodal displacement predictions have similar magnitudes as the case studies above. For example, in the [0°/30°] laminate results, the discrepancy is 2.1mm at nods 3 and 11, which is only slightly larger than the error shown in the smaller laminate results (1.9 mm). As a result, the normalized error is much more minor at 5.6%. Moreover, the corresponding R^2 values are very close to 1, indicating the performance of our model is exceptional as the square laminate size increases. On the other hand, Hyer's model's performance still lags.

The differences between the two analytical models elucidate the importance of considering inter-laminar strains and ensuring stress balance near the free edges. It is worth emphasizing that both analytical models predict smaller out-of-plane displacements than the finite element results, but Hyer's model's prediction deviates more. This is because the neglection of inter-laminar strain and stress would make the composite laminates appear stiffer than the actual value. Moreover, since the inter-laminate stress concentrates near the free edge (Figure 6.2, 6.3), the stress imbalance in Hyer's model introduces additional error.

6.3.4 Multiple-Patch Case Studies

Here, we extend our new analytical model to multi-patched laminates with complex designs and external shapes. To this end, we use the kirigami composite unit examined previously by the authors as the case study example [148]. This kirigami composite unit consists of five integrated patches, each defined based on its fiber ply orientations and four characteristic lengths (L_{tab}, L_{width}, L_{uncut}, and L_{height}) (Figure 6.7A). Due to the reversed ply-layups in regions 1 and 5, we can obtain rich geometrical shapes after curing.

To adapt the new model to the multi-patched structure. One can define a unique set of polynomial approximations for every patch and enforce appropriate compatibility conditions between them. The total potential energy of this kirigami composite unit is

$$\Pi_{total} = \Pi^1(c_i^1) + \Pi^2(c_i^2) + \Pi^3(c_i^3) + \Pi^4(c_i^4) + \Pi^5(c_i^5), \tag{6.16}$$

where the Π^i are the five different potential energy functions for the five patches in our study, c^i are the corresponding polynomial coefficients, and the superscript i ($i = 1 \dots 5$) refers to the five patches. These five patches have different polynomial approximations for their two in-plane strain fields (ϵ_x, ϵ_y), two rotation fields (θ_x, θ_y), and the out-of-plane displacement field (W_0). The in-plane strain functions remain the same as the single patch formulation, but the rotation and out-of-plane displacement fields have additional constant terms so that

$$\begin{aligned}
\theta_x^i &= c_{16}^i \frac{x}{L_x} + c_{17}^i \frac{y}{L_y} + c_{18}^i \frac{xy}{L_x L_y} + c_{19}^i \frac{x^3}{L_x^3} + c_{20}^i \frac{y^3}{L_y^3} + c_{26}^i, \\
\theta_y^i &= c_{21}^i \frac{x}{L_x} + c_{22}^i \frac{y}{L_y} + c_{23}^i \frac{xy}{L_x L_y} + c_{24}^i \frac{x^3}{L_x^3} + c_{25}^i \frac{y^3}{L_y^3} + c_{27}^i. \\
W_0^i &= c_9^i \frac{x^2}{L_x^2} + c_{10}^i \frac{y^2}{L_y^2} + c_{11}^i \frac{xy}{L_x L_y} + c_{12}^i \frac{x^2 y}{L_x^2 L_y} \\
&\quad + c_{13}^i \frac{xy^2}{L_x L_y^2} + c_{14}^i \frac{x^3}{L_x^3} + c_{15}^i \frac{y^3}{L_y^3} + c_{28}^i.
\end{aligned} \tag{6.17}$$

The constant terms at the end of each equation above introduce rigid-body rotations and displacement, which are necessary for ensuring displacement continuity between patches. Compatibility conditions are also required at the boundary between adjacent patches. In the new model, C^0 continuity constraints are sufficient — the adjacent patches should have the same displacement at their edges. In contrast, Hyer's model requires C^1 continuity that demands the same displacement and slopes [48]. For the x-direction edges shared between

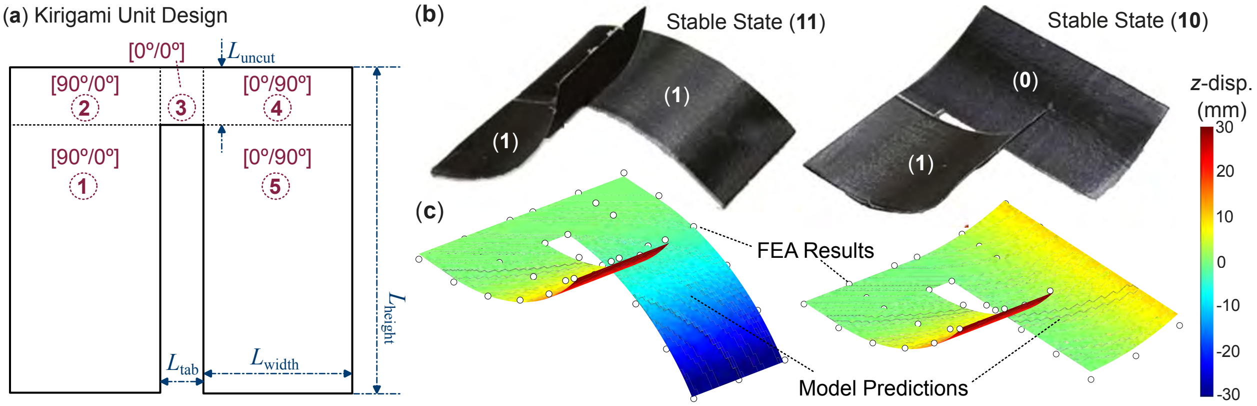

Figure 6.7: Summary of the multi-patched composite study: (a) The design of a kirigami unit consisting of 5 composite patches with different sizes and fiber ply layout. (b) Its external shapes at two stable states. (c) The corresponding theoretical predictions based on the new analytical approach and finite element. Here, the circles are nodal positions extracted from FEA results, and the colored surfaces are analytical model predictions. Color map represents out-of-plane displacements.

patches 1-2 and 4-5, the C^0 continuity requires

$$\begin{aligned} U_0^i(y=\pm L_y^i/2) &= U_0^{i+1}(y=\mp L_y^{i+1}/2), \\ V_0^i(y=\pm L_y^i/2) &= V_0^{i+1}(y=\mp L_y^{i+1}/2), \\ W_0^i(y=\pm L_y^i/2) &= W_0^{i+1}(y=\mp L_y^{i+1}/2). \end{aligned} \tag{6.18}$$

Similarly, for the y-direction edges shared between patches 2-3 and 3-4:

$$\begin{aligned} U_0^i(x=\pm L_x^i/2) &= U_0^{i+1}(x=\mp L_x^{i+1}/2), \\ V_0^i(x=\pm L_x^i/2) &= V_0^{i+1}(x=\mp L_x^{i+1}/2), \\ W_0^i(x=\pm L_x^i/2) &= W_0^{i+1}(x=\mp L_x^{i+1}/2). \end{aligned} \tag{6.19}$$

Here, L_x and L_y are the patches' lengths in local coordinate systems. We can translate them to the global coordinate system, whose origin is set at the mid-point of patch 3's bottom-edge. Also, we eliminate the overall rigid-body motion of the kirigami composite unit by setting the displacements at this origin to zero in that:

$$\begin{aligned} U_0^3(x=0, y=-L_y/2) &= 0, \\ V_0^3(x=0, y=-L_y/2) &= 0, \\ W_0^3(x=0, y=-L_y/2) &= 0. \end{aligned} \tag{6.20}$$

Figure 6.7 (B) shows two stable configurations of the Kirigami composite unit, and the corresponding geometric designs are $L_{tab} = 10$mm, $L_{width} = 40$mm, $L_{uncut} = 20$mm, and $L_{height} = 100$mm. Note that this structure can have four stable configurations [148]), but only two are used here for modal validation. The new analytical model based on the Reissner-Mindlin theory agrees excellently with the finite element simulation results, validating the model's capability for more complex, multi-patched composite laminates.

6.4 Conclusion

In this paper, we propose and validate a high-fidelity analytical approach — combining Reissner-Mindlin plate theory and hygroscopic degradation — for multi-stable asymmetric fiber composites. This study is motivated by the fact that 1) the currently available modeling approach for asymmetric composites has not seen any fundamental advancement since Hyer's pioneering research four decades ago, and 2) the moisture absorption has not received sufficient attention despite its significant influences on composite performance. Accordingly, the model developed in this paper introduces two primary contributions.

The contribution is integrating the Reissner-Mindlin plate and classical lamination theories for asymmetric composites. The RM theory introduces the rotations of the laminate's cross-section areas as independent variables. As a result, the new analytical approach can estimate the interlaminar shear and achieve stress balance at the free edges. These capabilities present a fundamental advancement because the current approaches neglect the interlaminate shear and create stress imbalance at the free edges. By comparing the new model's prediction to experimentally calibrated FEA, we show that the new model can estimate the interlaminar stress reasonably well (especially regarding its concentration near the edges) and predict the laminates' external shape more accurately than an equivalent Hyer's model. Such advantages are observed for single-patch laminates with different design configurations, as well as multi-patched structures exhibiting more complex geometries and multiple stable states.

In conclusion, this paper's new analytical modeling approach offers a broad and versatile foundation for designing and analyzing the next generation of multi-functional adaptive structures based on asymmetric composite laminates.

6.5 Appendix

Constitutive Material Property Calibration

The composite prepreg material used for the first part of our study (Table 6.1) consists of GRAFIL TR50S fiber and Newport 301 epoxy resin. Although the supplier (Rock West Composites, Inc.) provides some constitutive material properties, they were obtained based on autoclave curing. On the other hand, we use the vacuum bagging technique to prepare our multi-stable composite samples. Therefore, we expect the corresponding material properties can differ. Moreover, thermal expansion coefficients and shear modulus are not readily available. To obtain accurate estimations of these constitutive material properties, we combine experimental measurements and finite element simulations. The basic idea is to compare the shapes of the laminate from the experiments and FEA simulations, and then optimize the properties setup in FEA to reduce the discrepancy between them.

The first step is to measure the composite laminate's external shape experimentally. We use four 2-ply asymmetric laminate samples with a size of 100 mm × 100mm and ply configurations of $[0°/\alpha°]$, where the α varies between 90, 60, 45, and 30. We used a profilometer (NANOVEA™ ST500 optical profilometer) to create 3D scanned images of these laminates (an example in Figure 6.8). We filter these images to remove erroneous data points, and then apply translational and rotational transformations to eliminate rigid body motions about the laminate's mid-point.

The second step is to process these images through MATLAB's curve fitting tool to approximate the scanned surface using a complete, second-order polynomial fitting function. The accuracy of the fits for all laminate samples is more than 99.5% ($R^2 > 0.995$). We record the values of the fitted polynomial coefficients. In parallel, we use the same method to gather another set of fitted polynomial coefficients from the FEA simulations. These two sets of polynomial coefficients can be used to reconstruct the laminate surfaces observed in the experiment and FEA so that we can create an "error surface" by subtracting these two. Finally, the root-mean-square error (e_{rms}) is calculated based on this error surface as the objective function.

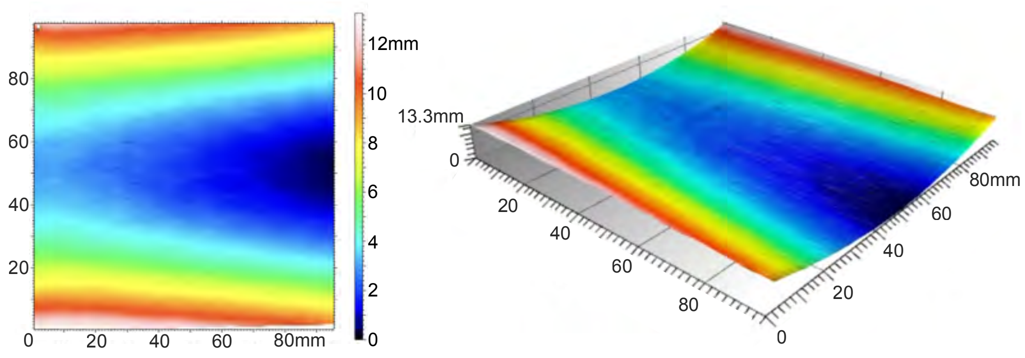

Figure 6.8: An example of profilometer scanning from the [0°/90°] laminate at its stable state. The color map shows the out-of-plane displacement.

Table 6.3: The final root-mean-square error (e_{rms}) after constitutive material property optimization. These errors are calculated based on the "error surfaces" that describe the differences between the experimentally measured laminate shapes and those predicted by FEA. These errors are the least for the cross-ply [0°/90°] laminate but increase as the angle between the fiber-ply layers decreases to 30 degrees.

Laminate	[0°/90°]	[0°/60°]	[0°/45°]	[0°/30°]
e_{rms} (mm)	0.74	0.74	1.24	1.42

In the final third step, we use optimization to identify the constitutive material property setup in FEA so that the e_{rms} is minimized across the results from all four laminate samples. Table 6.3 lists the final e_{rms} values.

FE Simulation Setup: Inter-laminar Shear Study

To understand the inter-laminar stresses, we conduct a finite element simulation on a square-shaped thin laminate plate in ABAQUS CAE 2020. This laminate consists of two layers of fiber ply of different ply angles ([0°/90°]); hence it is asymmetric. Its size is 100mm × 100mm × 0.24mm, and its constitutive material properties, summarized in Table 6.1, are calibrated from experiment data (Appendix Section A). We mesh the laminate using 3D quadratic brick elements with reduced integration (C3D20R). The element size is 2mm × 2mm × 0.06mm, giving four layers of elements through the laminate's thickness.

The simulation consists of three consecutive steps. In the first "curing step," the laminate is cooled down from the curing temperature of 135 °C to the room temperature of 20 °C, generating residual stress in the matrix. Due to its perfect square geometry, the laminate would take a saddle shape (unstable equilibrium) at the end of this step. In the second "snap-through" step, we fix the laminate at the center and force it towards one of the stable shapes via a prescribed displacement at its corners. In the third, "free damping" step, we release all constraints to the laminate except for the fixed center. This setup allows the laminate to settle into one stable shape with free-free boundary conditions and no external force.

Bibliography

[1] C. Perkins, "How the mclaren speedtail's flexible carbon-fiber ailerons work," *Road Track*, 2019.

[2] S. Daynes and P. M. Weaver, "Review of shape-morphing automobile structures: Concepts and outlook," *Proceedings of the Institution of Mechanical Engineers, Part D: Journal of Automobile Engineering*, vol. 227, no. 11, pp. 1603–1622, 2013.

[3] D. Rokaya, H. E. Skallevold, V. Srimaneepong, A. Marya, P. K. Shah, Z. Khurshid, M. S. Zafar, and J. Sapkota, "Shape memory polymeric materials for biomedical applications: An update," *Journal of Composites Science*, vol. 7, no. 1, 2023.

[4] M. Enyan, Z. Bing, J. N. O. Amu-Darko, E. Issaka, S. L. Otoo, and M. F. Agyemang, "Advances in smart materials soft actuators on mechanisms, fabrication, materials, and multifaceted applications: A review," *Journal of Thermoplastic Composite Materials*, vol. 38, no. 1, pp. 302–370, 2025.

[5] M. Behl and A. Lendlein, "Shape-memory polymers," *Materials Today*, vol. 10, no. 4, pp. 20–28, 2007.

[6] A. G. Olabi and A. Grunwald, "Design and application of magnetostrictive materials," *Materials & Design*, vol. 29, pp. 469–483, 2008.

[7] C. L. Lewis and E. M. Dell, "A review of shape memory polymers bearing reversible binding groups," *Journal of Polymer Science Part B: Polymer Physics*, vol. 54, no. 14, pp. 1340–1364, 2016.

[8] T. Wang, J. Zhang, Y. Li, J. Hong, and M. Y. Wang, “Electrostatic Layer Jamming Variable Stiffness for Soft Robotics,” *IEEE/ASME Transactions on Mechatronics*, vol. 24, pp. 424–433, 4 2019.

[9] Ying Shan, M. Philen, A. Lotfi, Suyi Li, C. E. Bakis, C. D. Rahn, and K. Wang, “Variable Stiffness Structures Utilizing Fluidic Flexible Matrix Composites,” *Journal of Intelligent Material Systems and Structures*, vol. 20, pp. 443–456, 3 2009.

[10] M. W. Hyer, “Some observations on the cured shape of thin unsymmetric laminates,” *Journal of Composite Materials*, vol. 15, pp. 175–194, mar 1981.

[11] M. W. Hyer, “The room-temperature shapes of four-layer unsymmetric cross-ply laminates,” *Journal of Composite Materials*, vol. 16, no. 4, pp. 318–340, 1982.

[12] M. W. Hyer and S. R. S. R. White, *Stress analysis of fiber-reinforced composite materials*. DEStech Publications, Inc, 2009.

[13] M.-l. Dano and M. W. Hyer, “Thermally-induced deformation behavior of unsymmetric laminates,” *International Journal of Solids and Structures*, vol. 35, no. 17, pp. 2101–2120, 1998.

[14] M. L. Dano and M. W. Hyer, “Snap-through of unsymmetric fiber-reinforced composite laminates,” *International Journal of Solids and Structures*, vol. 40, no. 22, pp. 5949–5972, 2000.

[15] S. Daynes and P. M. Weaver, “A morphing trailing edge device for a wind turbine,” *Journal of Intelligent Material Systems and Structures*, vol. 23, no. 6, pp. 691–701, 2012.

[16] S. P. Pellegrini, N. Tolou, M. Schenk, and J. L. Herder, “Bistable vibration energy

harvesters: A review," *Journal of Intelligent Material Systems and Structures*, vol. 24, no. 11, pp. 1303–1312, 2013.

[17] A. F. Arrieta, I. K. Kuder, T. Waeber, and P. Ermanni, "Variable stiffness characteristics of embeddable multi-stable composites," *Composites Science and Technology*, vol. 97, pp. 12–18, 6 2014.

[18] P. M. Reis, F. L. Jiménez, and J. Marthelot, "Transforming architectures inspired by origami," *Proceedings of the National Academy of Sciences*, vol. 112, no. 40, pp. 12234–12235, 2015.

[19] E. Vazquez, J. Diarte, and J. Duarte, "Kinetic shades: Designing a shape-morphing device with bistable laminates and shape memory actuators," *Journal of Architectural Engineering*, vol. 29, no. 4, p. 06023001, 2023.

[20] A. D. Shaw, S. A. Neild, D. J. Wagg, P. M. Weaver, and A. Carrella, "A nonlinear spring mechanism incorporating a bistable composite plate for vibration isolation," *Journal of Sound and Vibration*, vol. 332, pp. 6265–6275, nov 2013.

[21] A. F. Arrieta, P. Hagedorn, A. Erturk, and D. J. Inman, "A piezoelectric bistable plate for nonlinear broadband energy harvesting," *Applied Physics Letters*, vol. 97, no. 10, p. 104102, 2010.

[22] D. N. Betts, H. A. Kim, C. R. Bowen, and D. J. Inman, "Optimal configurations of bistable piezo-composites for energy harvesting," *Applied Physics Letters*, vol. 100, no. 11, p. 114104, 2012.

[23] R. L. Harne and K. W. Wang, "A review of the recent research on vibration energy harvesting via bistable systems," *Smart Materials and Structures*, vol. 22, p. 023001, jan 2013.

[24] S. A. Emam and D. J. Inman, “A Review on Bistable Composite Laminates for Morphing and Energy Harvesting,” *Applied Mechanics Reviews*, 2015.

[25] M. A. Cantera, J. M. Romera, I. Adarraga, and F. Mujika, “Modelling and testing of the snap-through process of bi-stable cross-ply composites,” *Composite Structures*, vol. 120, pp. 41–52, 2015.

[26] K. Potter, P. Weaver, A. A. Seman, and S. Shah, “Phenomena in the bifurcation of unsymmetric composite plates,” *Composites Part A: Applied Science and Manufacturing*, vol. 38, no. 1, pp. 100–106, 2007.

[27] A. Pirrera, D. Avitabile, and P. M. Weaver, “Bistable plates for morphing structures: A refined analytical approach with high-order polynomials,” *International Journal of Solids and Structures*, vol. 47, no. 25-26, pp. 3412–3425, 2010.

[28] I. K. Kuder, U. Fasel, P. Ermanni, and A. F. Arrieta, “Concurrent design of a morphing aerofoil with variable stiffness bi-stable laminates,” *Smart Materials and Structures*, vol. 25, p. 115001, 11 2016.

[29] I. K. Kuder, A. F. Arrieta, W. E. Raither, and P. Ermanni, “Variable stiffness material and structural concepts for morphing applications,” 11 2013.

[30] J. Sun, E. Lerner, B. Tighe, C. Middlemist, and J. Zhao, “Embedded shape morphing for morphologically adaptive robots,” *Nature communications*, vol. 14, no. 1, p. 6023, 2023.

[31] A. Rafsanjani and D. Pasini, “Bistable auxetic mechanical metamaterials inspired by ancient geometric motifs,” *Extreme Mechanics Letters*, vol. 9, pp. 291–296, 2016.

[32] A. McCrary, M. S. Hashemi, and A. Sheidaei, “Programmable Bidirectional Mechanical

Metamaterial with Tunable Stiffness and Frictional Energy Dissipation," *Advanced Theory and Simulations*, vol. 5, 7 2022.

[33] F. Zangeneh-Nejad, D. L. Sounas, A. Alù, and R. Fleury, "Analogue computing with metamaterials," *Nature Reviews Materials*, vol. 6, no. 3, pp. 207–225, 2021.

[34] K. S. Riley, S. Koner, J. C. Osorio, Y. Yu, H. Morgan, J. P. Udani, S. A. Sarles, and A. F. Arrieta, "Neuromorphic metamaterials for mechanosensing and perceptual associative learning," *Advanced Intelligent Systems*, vol. n/a, no. n/a, p. 2200158, 2022.

[35] S. J. Callens and A. A. Zadpoor, "From flat sheets to curved geometries: Origami and kirigami approaches," *Materials Today*, vol. 21, no. 3, pp. 241–264, 2018.

[36] S. Kamrava, D. Mousanezhad, H. Ebrahimi, R. Ghosh, and A. Vaziri, "Origami-based cellular metamaterial with auxetic, bistable, and self-locking properties," *Scientific Reports*, vol. 7, no. 1, p. 46046, 2017.

[37] M. Gardiner, *ORI* On the Aesthetics of Folding and Technology.* PhD thesis, 02 2019.

[38] W. K. Belvin, M. Straubel, W. K. Wilkie, M. Zander, J. M. Fernandez, and M. Hillebrandt, "Advanced deployable structural systems for small satellites," *NASA Technical Reports Server*, 2016.

[39] J. M. Fernandez, "Advanced deployable shell-based composite booms for small satellite structural applications including solar sails," in *International Symposium on Solar Sailing 2017*, no. NF1676L-25486, 2017.

[40] V. Rustagi and C. Sultan, "Closed-form solutions to continuous-time algebraic riccati equation for second-order systems," *Journal of Applied Mechanics*, vol. 91, no. 6, 2024.

[41] D. Mhadgut, A. Phoenix, and J. Black, “Data-driven rational approximation for composite boom deployment on a cubesat via vector-fitting,” in *AIAA SCITECH 2024 Forum*, p. 0410, 2024.

[42] S. PARTHASARATHY and R. K. KAPANIA, “Piece-wise ritz analysis of beams subjected to discontinuity in slope,” *STRUCTURAL HEALTH MONITORING 2023*, 2023.

[43] A. Algmuni, F. Xi, and H. Alighanbari, “Design and analysis of a grid patch multistable composite,” *Composite Structures*, vol. 246, no. January, p. 112378, 2020.

[44] V. Deshpande, O. Myers, G. Fadel, and S. Li, “Transient deformation and curvature evolution during the snap-through of a bistable laminate under asymmetric point load,” *Composites Science and Technology*, vol. 211, p. 108871, 7 2021.

[45] M.-L. Dano and M. W. Hyer, “Thermally-induced deformation behavior of unsymmetric laminates,” *International Journal of Solids and Structures*, vol. 35, pp. 2101–2120, 6 1998.

[46] J. P. Udani and A. F. Arrieta, “Analytical Modeling of Multi-sectioned Bi-stable Composites: Stiffness Variability and Embeddability,” *Composite Structures*, vol. 216, no. November 2018, pp. 228–239, 2019.

[47] F. Mattioni, P. Weaver, K. Potter, and M. Friswell, “Analysis of thermally induced multistable composites,” *International Journal of Solids and Structures*, vol. 45, 1 2008.

[48] F. Mattioni, P. M. Weaver, and M. I. Friswell, “Multistable composite plates with piecewise variation of lay-up in the planform,” *International Journal of Solids and Structures*, vol. 46, no. 1, pp. 151–164, 2009.

[49] M.-L. Dano, M. Jean-St-Laurent, and A. Fecteau, “Morphing of Bistable Composite Laminates Using Distributed Piezoelectric Actuators,” *Smart Materials Research*, vol. 2012, pp. 1–8, 2012.

[50] A. Pourfarzaneh, M. Taghavi, T. Helps, and J. Rossiter, “Towards Adaptive Prosthetic Sockets using 3D-printed Variable-stiffness Shape-memory Structures,” in *2019 2nd IEEE International Conference on Soft Robotics (RoboSoft)*, pp. 410–415, IEEE, 4 2019.

[51] S. Jiang, B. Chen, F. Qi, Y. Cao, F. Ju, D. Bai, and Y. Wang, “A variable-stiffness continuum manipulators by an SMA-based sheath in minimally invasive surgery,” *International Journal of Medical Robotics and Computer Assisted Surgery*, vol. 16, 4 2020.

[52] P. Butaud, D. Renault, B. Verdin, M. Ouisse, and G. Chevallier, “In-core heat distribution control for adaptive damping and stiffness tuning of composite structures,” *Smart Materials and Structures*, vol. 29, p. 065002, 6 2020.

[53] E. W. Hawkes, L. H. Blumenschein, J. D. Greer, and A. M. Okamura, “A soft robot that navigates its environment through growth,” *Science Robotics*, vol. 2, 7 2017.

[54] S. Cinquemani, G. Bianchi, N. Antonacci, and F. Resta, “Design of a soft pneumatic robot inspired to plant roots’ growth,” in *Bioinspiration, Biomimetics, and Bioreplication X* (A. Lakhtakia, R. J. Martín-Palma, and M. Knez, eds.), p. 36, SPIE, 4 2020.

[55] C. Majidi, “Soft Robotics: A Perspective—Current Trends and Prospects for the Future,” *Soft Robotics*, vol. 1, pp. 5–11, 3 2014.

[56] L. Deng, S. Sun, M. Christie, D. Ning, S. Jin, H. Du, S. Zhang, and W. Li, “Investigation of a seat suspension installed with compact variable stiffness and damping rotary

magnetorheological dampers," *Mechanical Systems and Signal Processing*, vol. 171, p. 108802, 5 2022.

[57] T. Mori, I. Nilkhamhang, and A. Sano, "ADAPTIVE SEMI-ACTIVE CONTROL OF SUSPENSION SYSTEM WITH MR DAMPER," *IFAC Proceedings Volumes*, vol. 40, no. 13, pp. 191–196, 2007.

[58] W. Cross, A. Kariotis, and F. Stimler, "Nitinol characterization study," tech. rep., NTRS - NASA Technical Reports Server, 9 1969.

[59] F. T. Calkins and J. H. Mabe, "Shape Memory Alloy Based Morphing Aerostructures," *Journal of Mechanical Design*, vol. 132, 11 2010.

[60] Z. Zhou and S. Li, "Self-Sustained And Coordinated Rhythmic Deformations With SMA For Controller-Free Locomotion," 10 2023.

[61] H. Tobushi, H. Hara, E. Yamada, and S. Hayashi, "Thermomechanical properties in a thin film of shape memory polymer of polyurethane series," *Smart Materials and Structures*, vol. 5, pp. 483–491, 8 1996.

[62] G. Mcknight, R. Doty, A. Keefe, G. Herrera, and C. Henry, "Segmented Reinforcement Variable Stiffness Materials for Reconfigurable Surfaces," *Journal of Intelligent Material Systems and Structures*, vol. 21, pp. 1783–1793, 11 2010.

[63] A. Lendlein, H. Jiang, O. Jünger, and R. Langer, "Light-induced shape-memory polymers," *Nature*, vol. 434, pp. 879–882, 4 2005.

[64] S. I. Rich, V. Nambeesan, R. Khan, and C. Majidi, "Tuning the composition of conductive thermoplastics for stiffness switching and electrically activated healing," *Journal of Intelligent Material Systems and Structures*, vol. 30, pp. 2908–2918, 11 2019.

[65] S. Puthanveetil, W. C. Liu, K. S. Riley, A. F. Arrieta, and H. Le Ferrand, "Programmable multistability for 3D printed reinforced multifunctional composites with reversible shape change," *Composites Science and Technology*, vol. 217, p. 109097, 1 2022.

[66] Y. Miyazawa, H. Yasuda, H. Kim, J. H. Lynch, K. Tsujikawa, T. Kunimine, J. R. Raney, and J. Yang, "Heterogeneous origami-architected materials with variable stiffness," *Communications Materials*, vol. 2, 12 2021.

[67] Q. Liu, H. Ye, J. Cheng, H. Li, X. He, B. Jian, and Q. Ge, "Stiffness-Tunable Origami Structures via Multimaterial Three-Dimensional Printing," *Acta Mechanica Solida Sinica*, vol. 36, pp. 582–593, 8 2023.

[68] E. R. Abrahamson, M. S. Lake, N. A. Munshi, and K. Gall, "Shape Memory Mechanics of an Elastic Memory Composite Resin," *Journal of Intelligent Material Systems and Structures*, vol. 14, pp. 623–632, 10 2003.

[69] Y. Chen, J. Sun, Y. Liu, and J. Leng, "Variable stiffness property study on shape memory polymer composite tube," *Smart Materials and Structures*, vol. 21, 9 2012.

[70] H. Michael, Y. Shan, K. W. Wang, C. E. Bakis, and C. D. Rahn, "Fluidic flexible matrix composites for the tailoring of variable stiffness adaptive structures," in *Collection of Technical Papers - AIAA/ASME/ASCE/AHS/ASC Structures, Structural Dynamics and Materials Conference*, vol. 1, pp. 24–34, 2007.

[71] S. Daynes and P. M. Weaver, "A morphing trailing edge device for a wind turbine," *Journal of Intelligent Material Systems and Structures*, vol. 23, pp. 691–701, 4 2012.

[72] A. Algmuni, F. Xi, and H. Alighanbari, "Flexible joints for a grid-based multi-stable composite morphing skin," *Composite Structures*, vol. 259, p. 113512, 3 2021.

[73] A. F. Arrieta, P. Hagedorn, A. Erturk, and D. J. Inman, “A piezoelectric bistable plate for nonlinear broadband energy harvesting,” *Applied Physics Letters*, vol. 97, 9 2010.

[74] Z. Zhang, H. Wu, X. He, H. Wu, Y. Bao, and G. Chai, “The bistable behaviors of carbon-fiber/epoxy anti-symmetric composite shells,” *Composites Part B: Engineering*, vol. 47, pp. 190–199, 4 2013.

[75] A. Mukherjee, M. I. Friswell, S. F. Ali, and A. Arockiarajan, “Modeling and design of a class of hybrid bistable symmetric laminates with cantilever boundary configuration,” *Composite Structures*, vol. 239, p. 112019, 5 2020.

[76] A. Lele, V. Deshpande, O. Myers, and S. Li, “Snap-through and stiffness adaptation of a multi-stable Kirigami composite module,” *Composites Science and Technology*, vol. 182, p. 107750, 9 2019.

[77] J. Biju, G. Fadel, S. Li, and O. Myers, “Design of Four-Patch Multi-Stable Composite Laminates for Shape Morphing Applications,” in *Volume 3B: 47th Design Automation Conference (DAC)*, American Society of Mechanical Engineers, 8 2021.

[78] J. P. Udani and A. F. Arrieta, “Analytical Modeling of Multi-sectioned Bi-stable Composites: Stiffness Variability and Embeddability,” *Composite Structures*, vol. 216, pp. 228–239, 5 2019.

[79] A. Pirrera, D. Avitabile, and P. Weaver, “Bistable plates for morphing structures: A refined analytical approach with high-order polynomials,” *International Journal of Solids and Structures*, vol. 47, pp. 3412–3425, 12 2010.

[80] D. V. Murray and O. J. Myers, “Modeling Bistable Composite Laminates for Piezoelectric Morphing Structures,” *ISRN Materials Science*, vol. 2013, pp. 1–12, 4 2013.

[81] V. Deshpande, S. A. Chowdhury, O. Myers, and S. Li, "High-fidelity analytical modeling of asymmetric CFRP composites using Reissner–Mindlin theory and hygroscopic degradation," *Composites Science and Technology*, vol. 236, p. 109983, 5 2023.

[82] S. A. Emam and D. J. Inman, "A Review on Bistable Composite Laminates for Morphing and Energy Harvesting," *Applied Mechanics Reviews*, vol. 67, 11 2015.

[83] A. Mukherjee, D. Kumar, S. F. Ali, and A. Arockiarajan, "Design and conception of a trailing edge morphing wing concept with bistable composite skin," in *Active and Passive Smart Structures and Integrated Systems IX* (J.-H. Han, S. Shahab, and G. Wang, eds.), p. 100, SPIE, 5 2020.

[84] G. Risso, M. Sakovsky, and P. Ermanni, "A Highly Multi-Stable Meta-Structure via Anisotropy for Large and Reversible Shape Transformation," *Advanced Science*, vol. 9, 9 2022.

[85] G. Risso and P. Ermanni, "Multi-stability of fiber-reinforced polymer frames with different geometries," *Composite Structures*, vol. 313, 6 2023.

[86] P. M. Weaver and M. P. Nemeth, "Bounds on Flexural Properties and Buckling Response for Symmetrically Laminated Composite Plates," *Journal of Engineering Mechanics*, vol. 133, pp. 1178–1191, 11 2007.

[87] K. Wang, L. Zhao, H. Hong, Y. Gong, J. Zhang, and N. Hu, "An analytical model for evaluating the buckling, delamination propagation, and failure behaviors of delaminated composites under uniaxial compression," *Composite Structures*, vol. 223, p. 110937, 9 2019.

[88] V. Sanmugadas, M. Agarwal, P. Borwankar, and R. K. Kapania, "Parametric model

order reduction for structural optimization of fiber composite structures," *AIAA Journal*, pp. 1–16, 2025.

[89] M. Agarwal, R. K. Kapania, C. A. Minaya, S. Venkataraman, and D. C. Hammerand, "Design framework for optimization of curvilinearly stiffened variable stiffness composite laminates with direct fiber angle parameterization," in *AIAA SCITECH 2024 Forum*, p. 1071, 2024.

[90] P. Borwankar, W. Zhao, R. K. Kapania, and M. Bansal, "Optimization of Hybrid Composite Laminates with Distinct Ply Thicknesses Using Integer Programming," *AIAA Journal*, pp. 1–11, 10 2023.

[91] G. Gerard and H. Becker, "Handbook of structural stability part III : buckling of curved plates and shells," tech. rep., NTRS - NASA Technical Reports Server, 8 1957.

[92] D. Tripathi and R. S. Hegde, "Phase change material metasurface loading enables an ultrafast all-optically switchable, compact, narrowband freespace optical filter," *Optics Communications*, vol. 569, p. 130788, 2024.

[93] Q.-w. Lin, H. Wong, L. Huitema, and A. Crunteanu, "Coding metasurfaces with reconfiguration capabilities based on optical activation of phase-change materials for terahertz beam manipulations," *Advanced Optical Materials*, vol. 10, no. 1, p. 2101699, 2022.

[94] J. Tao, H. Khosravi, V. Deshpande, and S. Li, "Engineering by cuts: how kirigami principle enables unique mechanical properties and functionalities," *Advanced Science*, vol. 10, no. 1, p. 2204733, 2023.

[95] F. Fiorito, M. Sauchelli, D. Arroyo, M. Pesenti, M. Imperadori, G. Masera, and

G. Ranzi, "Shape morphing solar shadings: A review," *Renewable and Sustainable Energy Reviews*, vol. 55, pp. 863–884, 2016.

[96] A. Flores-Abad, O. Ma, K. Pham, and S. Ulrich, "A review of space robotics technologies for on-orbit servicing," *Progress in aerospace sciences*, vol. 68, pp. 1–26, 2014.

[97] D. Li, L. Zhong, W. Zhu, Z. Xu, Q. Tang, and W. Zhan, "A survey of space robotic technologies for on-orbit assembly," *Space: Science & Technology*, 2022.

[98] B. Kresling, "The fifth fold: complex symmetries in kresling-origami patterns," *Symmetry: Culture and Science*, vol. 31, no. 4, pp. 403–416, 2020.

[99] K. Seffen and S. Stott, "Surface texturing through cylinder buckling," *Journal of Applied Mechanics*, vol. 81, no. 6, p. 061001, 2014.

[100] P. Bhovad, J. Kaufmann, and S. Li, "Peristaltic locomotion without digital controllers: Exploiting multi-stability in origami to coordinate robotic motion," *Extreme Mechanics Letters*, vol. 32, p. 100552, 2019.

[101] I. K. Kuder, A. F. Arrieta, W. E. Raither, and P. Ermanni, "Variable stiffness material and structural concepts for morphing applications," *Progress in Aerospace Sciences*, vol. 63, pp. 33–55, 2013.

[102] K. Bertoldi, V. Vitelli, J. Christensen, and M. V. Hecke, "Flexible mechanical metamaterials," *Nature Reviews Materials*, vol. 2, 2017.

[103] H. Khosravi and S. Li, "Tunable wave-propagation band gap via stretching kirigami sheets," *Physical Review Applied*, vol. 17, no. 6, p. 064054, 2022.

[104] W. Zhang, X. Wang, Y. Wang, G. Yang, C. Gu, W. Zheng, Y.-M. Zhang, M. Li, and S. X.-A. Zhang, "Bio-inspired ultra-high energy efficiency bistable electronic billboard and reader," *Nature Communications*, vol. 10, no. 1, p. 1559, 2019.

[105] J. Barth, B. Krevet, and M. Kohl, “A bistable shape memory microswitch with high energy density,” *Smart Materials and Structures*, vol. 19, p. 094004, aug 2010.

[106] G. Wang, T. Cheng, Y. Do, H. Yang, Y. Tao, J. Gu, B. An, and L. Yao, “Printed paper actuator: A low-cost reversible actuation and sensing method for shape changing interfaces,” *Conference on Human Factors in Computing Systems - Proceedings*, vol. 2018-April, no. April, 2018.

[107] P. Bhovad and S. Li, “Physical reservoir computing with origami and its application to robotic crawling,” *Scientific Reports*, vol. 11, no. 1, pp. 1–18, 2021.

[108] D. S. Cairns and D. F. Adams, “Moisture and thermal expansion of composite materials,” 11 1981.

[109] F. Naya, J. M. Molina-Aldareguía, C. S. Lopes, C. González, and J. Llorca, “Interface characterization in fiber-reinforced polymer–matrix composites,” *JOM*, vol. 69, pp. 13–21, 1 2017.

[110] C. Thill, J. Etches, I. Bond, K. Potter, and P. Weaver, “Morphing skins,” *The Aeronautical Journal*, vol. 112, 3 2008.

[111] M. R. Schultz, “A concept for airfoil-like active bistable twisting structures,” *Journal of Intelligent Material Systems and Structures*, vol. 19, pp. 157–169, 2 2008.

[112] X. Lachenal, S. Daynes, and P. M. Weaver, “Review of morphing concepts and materials for wind turbine blade applications,” *Wind Energy*, vol. 16, 3 2013.

[113] Q. Ai, P. M. Weaver, T. K. Barlas, A. S. Olsen, H. A. Madsen, and T. L. Andersen, “Field testing of morphing flaps on a wind turbine blade using an outdoor rotating rig,” *Renewable Energy*, vol. 133, pp. 53–65, 2019.

[114] F. Dai, H. Li, and S. Du, “A multi-stable lattice structure and its snap-through behavior among multiple states,” *Composite Structures*, vol. 97, pp. 56 – 63, 2013.

[115] S. A. Emam, “Snapthrough and free vibration of bistable composite laminates using a simplified Rayleigh-Ritz model,” *Composite Structures*, vol. 206, no. August, pp. 403–414, 2018.

[116] J. Galos, “Thin-ply composite laminates: a review,” *Composite Structures*, vol. 236, 3 2020.

[117] A. Delbariani-Nejad, A. Farrokhabadi, and M. Fotouhi, “Finite element reliability analysis of edge delamination onset due to interlaminar stresses in composite laminates,” *Composite Structures*, vol. 288, 5 2022.

[118] Y. Yuan, X. Yao, B. Liu, H. Yang, and H. Imtiaz, “Failure modes and strength prediction of thin ply cfrp angle-ply laminates,” *Composite Structures*, vol. 176, pp. 729–735, 9 2017.

[119] M. R. Schultz and M. W. Hyer, “Snap-through of unsymmetric cross-ply laminates using piezoceramic actuators,” *Journal of Intelligent Material Systems and Structures*, vol. 14, 12 2003.

[120] M. R. Schultz, M. W. Hyer, R. B. Williams, W. K. Wilkie, and D. J. Inman, “Snap-through of unsymmetric laminates using piezocomposite actuators,” *Composites Science and Technology*, vol. 66, 11 2006.

[121] W. Hufenbach, M. Gude, and A. Czulak, “Actor-initiated snap-through of unsymmetric composites with multiple deformation states,” *Journal of Materials Processing Technology*, vol. 175, 6 2006.

[122] Y. Gandhi, A. Pirondi, and L. Collini, “Analysis of bistable composite laminate with embedded sma actuators,” *Procedia Structural Integrity*, vol. 12, 2018.

[123] C. H. Shen and G. S. Springer, “Moisture absorption and desorption of composite materials,” *Journal of Composite Materials*, vol. 10, pp. 2–20, 1976.

[124] R. Jana and H. Bhunia, “Hygrothermal degradation of the composite laminates from woven carbon/sc-15 epoxy resin and woven glass/sc-15 epoxy resin,” *Polymer Composites*, vol. 29, 6 2008.

[125] B. Abdel-Magid, S. Ziaee, K. Gass, and M. Schneider, “The combined effects of load, moisture and temperature on the properties of e-glass/epoxy composites,” *Composite Structures*, vol. 71, no. 3, pp. 320–326, 2005. Fifth International Conference on Composite Science and Technology.

[126] N. Sateesh, P. S. Rao, D. V. Ravishanker, and K. Satyanarayana, “Effect of moisture on gfrp composite materials,” vol. 2, pp. 2902–2908, Elsevier Ltd, 2015.

[127] S. Genna, F. Trovalusci, and V. Tagliaferri, “Indentation test to study the moisture absorption effect on cfrp composite,” *Composites Part B: Engineering*, vol. 124, pp. 1–8, 9 2017.

[128] F. Ahmad, F. Abbassi, J.-W. Hong, S.-H. Chang, and M. K. Park, “Hygroscopic effects on the penetration-resistance behavior of a specially-orthotropic cfrp composite plates,” *Composite Structures*, vol. 176, pp. 1073–1080, 2017.

[129] H. Choi, K. Ahn, J.-D. Nam, and H. Chun, “Hygroscopic aspects of epoxy/carbon fiber composite laminates in aircraft environments,” *Composites Part A: Applied Science and Manufacturing*, vol. 32, 5 2001.

[130] E. Hörberg, M. Åkermo, and S. Hallström, “Moisture effect on shape distortions of curved quasi-isotropic prepreg composite laminates,” *Composites Part A: Applied Science and Manufacturing*, vol. 145, p. 106361, 2021.

[131] B. Harper and Y. Weitsman, “On the effects of environmental conditioning on residual stresses in composite laminates,” *International Journal of Solids and Structures*, vol. 21, pp. 907–926, 1985.

[132] J. Etches, K. Potter, P. Weaver, and I. Bond, “Environmental effects on thermally induced multistability in unsymmetric composite laminates,” *Composites Part A: Applied Science and Manufacturing*, vol. 40, pp. 1240–1247, 8 2009.

[133] C. Mittelstedt and W. Becker, “Free-Edge Effects in Composite Laminates,” *Applied Mechanics Reviews*, vol. 60, pp. 217–245, 09 2007.

[134] C. A. Rose and C. T. Herakovich, “An approximate solution for interlaminar stresses in composite laminates,” *Composites Engineering*, vol. 3, no. 3, pp. 271–285, 1993.

[135] C. Kassapoglou and P. A. Lagace, “An Efficient Method for the Calculation of Interlaminar Stresses in Composite Materials,” *Journal of Applied Mechanics*, vol. 53, pp. 744–750, 12 1986.

[136] R. B. Pipes and N. J. Pagano, “Interlaminar stresses in composite laminates—an approximate elasticity solution,” *Journal of Applied Mechanics*, vol. 41, pp. 668–672, 09 1974.

[137] R. Jones, *Mechanics Of Composite Materials.* CRC Press, 1999. `https://doi.org/10.1201/9781498711067`.

[138] Y.-J. Wu, T. Takatoya, K. Chung, J. C. Seferis, and K. Ahn, “Development of the transient simulated laminate (tsl) methodology for moisture ingression studies using

unsymmetric laminates," *Journal of Composite Materials*, vol. 34, pp. 1998–2015, 12 2000.

[139] G. Gendron, M. L. Dano, and A. Cloutier, "A numerical study of the hygro-mechanical deformation of two cardboard layups," *Composites Science and Technology*, vol. 64, pp. 619–627, 2004.

[140] H. Chai, Y. Li, Z. Zhang, M. Sun, H. Wu, and S. Jiang, "Systematic analysis of bistable anti-symmetric composite cylindrical shells and variable stiffness composite structures in hygrothermal environment," *International Journal of Advanced Manufacturing Technology*, vol. 108, pp. 1091–1107, 5 2020.

[141] Z. Zhang, H. Pan, H. Wu, S. Jiang, and G. Chai, "Hygroscopic influence on bistable characteristics of antisymmetric composite cylindrical shells: An experimental study," *Journal of Composite Materials*, vol. 52, pp. 3565–3577, 11 2018.

[142] P. Portela, P. Camanho, P. Weaver, and I. Bond, "Analysis of morphing, multi stable structures actuated by piezoelectric patches," *Computers & Structures*, vol. 86, pp. 347–356, feb 2008.

[143] M. Gigliotti, F. Jacquemin, J. Molimard, and A. Vautrin, "Transient and cyclical hygrothermoelastic stress in laminated composite plates: Modelling and experimental assessment," *Mechanics of Materials*, vol. 39, pp. 729–745, 8 2007.

[144] D. A. Powers, "Interaction of water with epoxy.," tech. rep., Sandia National Laboratories (SNL), 7 2009.

[145] M. Cavasin, M. Sangermano, B. Thomson, and S. Giannis, "Exposure of glass fiber reinforced polymer composites in seawater and the effect on their physical performance," *Materials*, vol. 12, p. 807, 3 2019.

[146] R. D. Mindlin, "Influence of Rotatory Inertia and Shear on Flexural Motions of Isotropic, Elastic Plates," *Journal of Applied Mechanics*, vol. 18, pp. 31–38, 04 2021.

[147] E. Reissner, "The effect of transverse shear deformation on the bending of elastic plates," 1945.

[148] A. Lele, V. Deshpande, O. Myers, and S. Li, "Snap-through and stiffness adaptation of a multi-stable Kirigami composite module," *Composites Science and Technology*, vol. 182, no. May, p. 107750, 2019.

[149] V. Deshpande, O. Myers, G. Fadel, and S. Li, "Transient deformation and curvature evolution during the snap-through of a bistable laminate under asymmetric point load," *Composites Science and Technology*, vol. 211, 7 2021.